

Understanding radio pulsar emission through single pulse studies

Ph.D. Thesis

by

Parul Janagal



**Department of Astronomy, Astrophysics
and Space Engineering**

**Indian Institute of Technology Indore
Khandwa Road, Simrol, Indore - 453552, India**

Understanding radio pulsar emission through single pulse studies

A THESIS

Submitted in partial fulfilment of the requirements for the award of the degree

of

DOCTOR OF PHILOSOPHY

by

Parul Janagal



**Department of Astronomy, Astrophysics
and Space Engineering**

**Indian Institute of Technology Indore
Khandwa Road, Simrol, Indore - 453552, India**



INDIAN INSTITUTE OF TECHNOLOGY INDORE

I hereby certify that the work which is being presented in the thesis entitled “**Understanding radio pulsar emission through single pulse studies**” in the partial fulfilment of the requirements for the award of the degree of **DOCTOR OF PHILOSOPHY** and submitted in the **DEPARTMENT OF ASTRONOMY, ASTROPHYSICS, AND SPACE ENGINEERING (DAASE), Indian Institute of Technology Indore**, is an authentic record of my own work carried out during the time period from **July 2018 to February 2024** under the supervision of Dr Manoneeta Chakraborty, Associate Professor, IIT Indore (India) and Dr N. D. Ramesh Bhat, Senior Research Fellow, Curtin University (Western Australia).

The matter presented in this thesis has not been submitted by me for the award of any other degree of this or any other institute.

February 14, 2024
(**PARUL JANAGAL**)

This is to certify that the above statement made by the candidate is correct to the best of my knowledge.

14/02/2024

(**DR MANONEETA CHAKRABORTY**)

14/02/2024

(**DR N. D. RAMESH BHAT**)

Parul Janagal has successfully given her PhD. Oral Examination held on **February 14, 2024**.

14/02/2024

(**DR MANONEETA CHAKRABORTY**)

14/02/2024

(**DR N. D. RAMESH BHAT**)

“Never be cruel, never be cowardly.

Remember ...

Hate is always foolish,

Love is always wise,

Always try to be nice,

But never fail to be kind.”

- The Doctor

Acknowledgements

I sincerely thank Dr Manoneeta Chakraborty, who was kind and patient with me throughout the last five years. She gave me her best advice in work and in life, for which I'll always be thankful. I also thank Dr N. D. Ramesh Bhat, who, despite the time difference, always found time to discuss and counsel me on my research. Ramesh, getting your comments and suggestions was humbling, and I feel grateful to have the chance to learn from you. Without my supervisors' guidance, I'd not be as proud of myself as I am today. Many thanks to my collaborator Dr Samuel J. McSweeney, who patiently listened to all my crazy ideas, irrespective of the hours it may take, and gave his most honest opinion. Sam, I've never had a better teacher than you. I also extend my gratitude to Dr Suman Majumdar, my advisor outside of academia and a guiding light. I thank all the resources provided by IIT Indore and the CSIR for their Junior and Senior Research Fellowships.

Mumma, papa, and Ankit, thank you for believing in me when others didn't, supporting me when I felt weak, and loving me unconditionally. I hope I made you proud. Amma, Achhan, and Krishna, I am fortunate to have you in my life as my second family.

Harshita, you continue to be with me through thick and thin; without you, I'd not be me. No words will express how happy I am to have you still. My chosen family - Akriti, Sriya, and Unnati, the last five years have been nothing short of amazing. Our late-night gossip, cheese pasta, dance practice, evening tea, and whatnot, I'll keep those memories closest to my heart. I will miss you dearly. Let's meet soon and go see the world together. Akriti, you know you're special by getting the special photographic mention in Fig. 2.1 of this thesis. Others, please don't be jealous.

I was not the one to have a gang. Still, I had one with you - Sarvesh, Sayan, Arghyadeep, Anshuman, Hemapriya, and Swarna. I have too many happy memories to write them down here, but I'll remember to visit my photo album when I feel nostalgic.

Kamran, thanks for being a gracious host and a friend. I will one day learn to make biryani like yours. Many thanks to my seniors - Deepthi, Aishrila, Madhurima, Sumanjeet, Arnab, Sanmoy, Althaf, Majid, and Ramij who guided us through this journey.

I also thank the Doctor for reigniting my love for the universe I had once lost! I'm now a forever whovian.

The one person I'd like to thank the most is my husband, whose belief in me never faltered even an inch and who never left my side despite our distance. Adarsh, with all my heart, I dedicate this thesis to you.

"Allons-y"- The Doctor

Abstract

The discovery of pulsars revolutionised our understanding of physics under extreme physical environments. Over the past five decades since their discovery in 1967, these exotic objects have proven to be extremely useful for an astonishing range of physics and astrophysics. They were discovered through the detection of their highly collimated beams of radiation as it intercepts our line of sight while the pulsar rotates around its spin axis. However, even after decades of extensive research, the emission mechanism that produces the emission of electromagnetic radiation from these fascinating objects remains one of the outstanding problems in astrophysics.

While pulsar emission can be studied via a number of phenomena, studies of individual pulses have been proven fruitful. They provide direct information about the emission process inside the dynamic pulsar magnetosphere and are, therefore, essential for understanding the physical mechanisms governing pulsar radiation. Pulsars exhibit a plethora of emission phenomena, such as subpulse drifting, giant pulses, nulling, mode switching, and microstructure, to name a few. Notwithstanding the substantial progress made over the past years – both on observational and theoretical fronts – we still lack a satisfactory theoretical understanding of many of these distinctive emission phenomena.

This thesis attempts to study several important aspects of pulsar radio emission by studying the time variability in the emission properties of consecutive single pulses. Utilising data from two of the world-class radio-astronomy facilities – the upgraded Giant Metrewave Radio Telescope (uGMRT) and the Murchison Widefield Array (MWA) – both of which are amongst the recognised pathfinder/precursor facilities for the international Square Kilometre Array (SKA) telescope, we have studied the pulse-to-pulse variability in three specific pulsars: PSR J1822–2256, PSR J1820–0427, and PSR J0026–1955.

Our analysis of PSR J1822–2256 revealed that this pulsar exhibits four distinct sub-

pulse drifting modes. A detailed analysis has allowed us to calculate the possible spark configurations for each one of these modes and examine their relation to the emission heights. The large frequency coverage of our observations (~ 300 to 750 MHz) has allowed us to explore the frequency dependence of the observed subpulse drifting characteristics. Furthermore, our analysis has also revealed an inverse relation between the drift rate periodicity and the inferred emission heights, which may prove insightful in linking the emission heights to the underlying spark configuration. This work forms the subject matter of Chapter 3.

The theme of Chapter 4 is centred around the pulse-to-pulse variability of PSR J1820–0427, using high-quality data obtained from the MWA and the uGMRT, thus spanning a frequency range from ~ 170 to 750 MHz. The low-frequency data from the MWA has revealed a post-cursor feature in the average profile that was not reported in previous observations made at higher frequencies. We also developed and demonstrated the application of a new method for calibrating single-pulse flux densities using concurrent phased array and imaging observations now possible with the upgraded GMRT. Our analysis involved exploring the frequency-dependence of pulse-fluence distribution and its relation to the Stochastic Growth Theory. The calibrated intensities were also used to study the spectral indices of individual pulses and their distributions across a broad frequency range.

The focus theme of Chapter 5 is the investigation of subpulse drifting and nulling phenomena in PSR J0026–1955, a new pulsar discovered with the MWA. Our analysis of uGMRT follow-up of this pulsar (observations made at 300 - 500 MHz) has revealed the rare phenomenon of evolutionary subpulse drifting. Notably, the pulsar exhibits two distinct subpulse drifting modes (one of which can be further sub-categorised into three different modes) and a large nulling fraction of $\sim 58\%$. Its active emissions are marked by both rapid changes between the drift modes and a gradual evolution in the drift rate within two specific modes. Remarkably, our observations also provide evidence in support of

a subpulse memory across nulls and a general tendency where a particular mode often precedes the occurrence of a null. Based on our analysis and findings, we propose two plausible physical models that may explain the observed evolutionary drifting behaviour seen in this pulsar.

Even though the work described in this thesis is focused on the studies of three specific pulsars, the findings and analyses presented are also applicable to a wider population of pulsars, especially considering the prevalence of the explored emission phenomenon, such as subpulse drifting and nulling. Therefore, many of the findings that emerge from this thesis may have a broader significance, and the study can now be extended to other pulsars exhibiting similar emission phenomenology. Future astronomy facilities, in particular the SKA and its pathfinders, with their broad frequency coverage and high instantaneous sensitivity, can be well exploited for in-depth studies of single-pulse phenomena in an effort to gain a more comprehensive understanding of underlying physical processes and ultimately to uncover the intricacies of pulsar emission mechanism and unlock its secrets.

List of Publications

1. **Janagal, P.**, Chakraborty, M., Bhat, N. D. R., Bhattacharyya, B., and McSweeney, S. J., “Revisiting the subpulse drifting phenomenon in PSR J1822–2256: drift modes, sparks, and emission heights”, 2022, *Monthly Notices of the Royal Astronomical Society*, Volume 509, Issue 3, Pages 4573–4584, doi:10.1093/mnras/stab3305
2. **Janagal, P.**, Chakraborty, M., Bhat, N. D. R., McSweeney, S. J., and Sett S., “Single-pulse analysis and average emission characteristics of PSR J1820–0427 from observations made with the MWA and uGMRT”, 2023, *Monthly Notices of the Royal Astronomical Society*, Volume 523, Issue 4, August 2023, Pages 5934–5946, doi:10.1093/mnras/stad1797
3. **Janagal, P.**, McSweeney, S. J., Chakraborty, M., and Bhat, N. D. R., “PSR J0026–1955: A curious case of evolutionary subpulse drifting and nulling”, 2023, *Monthly Notices of the Royal Astronomical Society*, Volume 524, Issue 2, September 2023, Pages 2684–2697, doi:10.1093/mnras/stad2056

Table of Contents

Title	i
Acknowledgements	ix
Abstract	xii
List of Publications	xv
Table of Contents	xvii
List of Figures	xxii
List of Tables	xxix
List of abbreviations	xxx
1 Introduction	1
1.1 Pulsars	2
1.2 Observed pulsar signal	4
1.3 Integrated pulse profiles	6
1.4 Propagation effects	8
1.4.1 Dispersion	9
1.4.2 Scattering	11
1.4.3 Scintillation	13
1.5 Variability in intrinsic pulsar emission	14
1.5.1 Pulse-to-pulse amplitude modulation	15
1.5.2 Subpulse Drifting	16
1.5.2.1 Characterisation of drift bands	17

1.5.2.2	The Carousel Model	19
1.5.3	Nulling	22
1.6	A Theoretical Outlook	24
1.6.1	Neutron stars and Pulsars	24
1.6.2	The pulsar magnetosphere	25
1.6.3	Emission Mechanism	27
1.7	Motivation and scope of this thesis	29
2	Data Acquisition and Pre-processing	33
2.1	The upgraded Giant Metrewave Radio Telescope	34
2.1.1	Phased Array	35
2.1.2	Interferometer	36
2.2	The Murchison Widefield Array	36
2.2.1	The Voltage Capture System	38
2.2.2	Tied-array Beamforming	38
2.3	Data Processing	39
2.3.1	PRESTO	39
2.3.2	DSPSR	41
2.3.3	PSRCHIVE	41
2.3.4	CASA and SPAM	43
3	Subpulse drifting in PSR J1822-2256	46
3.1	Observations	50
3.2	Analysis	52
3.2.1	Mode change boundaries and characterising P_3 values	53
3.2.2	Modes of Emission	54
3.2.2.1	Mode A	55

3.2.2.2	Mode B	55
3.2.2.3	Mode C	58
3.2.2.4	Mode D	58
3.2.3	P_3 distribution	59
3.2.4	Nulling behaviour of J1822–2256	60
3.2.5	Characterising P_2	61
3.2.6	Investigation of the frequency dependence of profile components	61
3.2.7	Probing the emission geometry with polarisation observations	62
3.2.8	Determination of emission heights for the emission modes	66
3.3	Discussion	68
3.3.1	Spark calculation	69
3.3.2	Modes and implications for pulsar emission	72
3.3.3	Emission heights for modes	74
3.4	Summary	75
4	Single-pulse study of PSR J1820-0427	78
4.1	Observations	82
4.1.1	The uGMRT	82
4.1.2	The MWA	84
4.2	Data Processing	85
4.2.1	uGMRT	86
4.2.1.1	Imaging	86
4.2.1.2	Phased Array Beam	89
4.2.2	MWA	90
4.2.2.1	Imaging	90
4.2.2.2	Phased Array Beam	91
4.2.3	Flux Density Calibration	91

4.3	Analysis and Results	94
4.3.1	Profile Evolution	94
4.3.2	Pulse-to-pulse Variability	94
4.3.3	Pulse Fluence Distribution	96
4.3.4	Flux density spectrum	99
4.3.5	Scatter Broadening	101
4.3.6	Faraday Rotation	104
4.4	Discussion	105
4.4.1	Pulse Fluence Distribution	105
4.4.2	Spectral Analysis	107
4.4.2.1	Mean Flux Density Spectrum	107
4.4.2.2	Pulse-to-pulse Variability	108
4.5	Summary	110
5	Evolutionary subpulse drifting and nulling in PSR J0026–1955	114
5.1	Observations and Data Reduction	120
5.2	Analysis	122
5.2.1	Drift Mode Boundaries	122
5.2.2	Drift Mode Classification	129
5.2.3	Nulling	133
5.2.4	Drift Rate Evolution	133
5.2.4.1	A fourth-order polynomial fit of drift rates	137
5.2.5	Memory across nulls	139
5.3	Discussion	142
5.3.1	Nulling Behaviour of J0026–1955	143
5.3.2	Drift Rate - Nulling Correlation	144
5.3.3	Memory Across Nulls	145

5.3.3.1	Drift rate memory	146
5.3.3.2	Subpulse phase memory	147
5.3.4	Subpulse Drifting Model for J0026–1955	148
5.3.4.1	Variable Spark Configuration in Carousel Model	148
5.3.4.2	Carousel Model in Partially Screened Gap	150
5.3.4.3	Revisiting Mode A2 - Null Correlation	151
5.4	Summary	152
6	Summary and Future Prospects	156

List of Figures

1.1	Sequence of 20 consecutive pulses observed from PSR J1820–0427 using the upgraded Giant Metrewave Radio Telescope at 317 MHz. The x -axis shows the time elapsed in seconds since the beginning of the observation.	5
1.2	Consecutive single pulses are stacked to form a two-dimensional pulse stack showing variability in pulsar signal over time (y -axis; pulse number) and phase (x -axis). The figure shows a pulse stack of over 6000 pulses observed for PSR J1820–0427 at 317 MHz, using uGMRT.	6
1.3	Average profile of PSR J1820-0427 (left) and PSR J0026-1955 (right) at 400 MHz integrating ~ 6000 and ~ 2500 single pulses, respectively. The pulse phase on x -axis is synonymous to pulse phase from 0° to 360° . The flux on the y -axis is in arbitrary units.	7
1.4	The effect of dispersion on a single pulse from J1820–0427 observed using uGMRT. Due to the intervening ISM, the pulsar signal at a higher frequency arrives before the signal at a lower frequency. The colour scale pattern shows the uncorrected dispersed signal as a function of the observing frequency.	9
1.5	Scattering of a single pulse from PSR J1820–0427, simultaneously observed at 300-750 MHz from uGMRT. An increase in scattering time towards lower frequencies can be clearly noted.	12
1.6	Dynamic spectrum of PSR J0026–1955 in a 50 MHz subband, observed from uGMRT. The colour scale represents the intensity of the observed pulsar signal. It can be noted that the pulsar is not uniformly bright at all frequencies across the observed time range.	14

1.7	A pulse stack of PSR J1822–2256 using observations from uGMRT at 300-500 MHz. Within the on-pulse region, around phase 0°, the pulsar can be seen to exhibit subpulse drifting. It is also known to show multiple kinds of subpulse drifting modes, each with different P_2 and P_3 . A detailed study of the wideband behaviour of the subpulse drifting phenomenon in J1822–2256 is presented in chapter 3.	17
1.8	A schematic of the carousel model (Ruderman & Sutherland, 1975) showing sub-beams formed in the pulsar’s main beam, around the magnetic axis, due to a carousel of sparks near the pulsar surface. As the pulsar rotates around its magnetic axis, because of the difference between carousel rotation and pulsar rotation, a different configuration of sub-beams is observed every time, which leads to the observed drifting of subpulses.	20
1.9	Example of nulling shown by PSR J0026–1955 observed at 300-500 MHz, using uGMRT. A few pulses near the beginning and towards the middle of the sequence are missing. The x –axis represents time elapsed (in seconds) since the beginning of the observation.	22
2.1	Antenna C3 of the uGMRT telescope, alongside a model of the array configuration. The antenna is 45 meters in diameter and is part of the central square. <i>Image Credit: Parul Janagal</i>	34
2.2	One of the 256 “tiles” that make up the MWA telescope. Each tile has 16 cross-dipole antennas, which are connected to an analogue beamformer (white box). (<i>Image credit: Dr John Goldsmith/Celestial Visions, 2012</i>)	37
2.3	A PRESTO diagnostic plot for PSR J1822–2256, observed with Band 3 (300-500 MHz) of uGMRT. The bottom-left panel shows a pulse stack of the observed signal. The average pulsar profile is shown at the top left. The wide-band nature of the pulsar can be seen in the top-middle figure. The peak in the bottom-middle plot shows the DM at which the signal, when de-dispersed, has the largest S/N. The plots on the right show a search over P and \dot{P}	40
2.4	<i>Top:</i> Pulse stack before using the <code>pazi</code> subroutine for RFI mitigation. <i>Bottom:</i> Pulse stack after a few rounds of manual RFI cleaning using the <code>pazi</code> subroutine. The subpulse drifting features and pulsar nulling can be clearly observed in the lower panel.	42
2.5	A radio image of the sky near PSR J1820–0247 at 550 MHz. The pulsar is at the phase centre of the image. This data was reduced using the SPAM pipeline described in §2.3.4.	45

3.1	2D-pulsestacks displaying the subpulse drifting modes of emission observed for J1822-2256. The modes A, B, C, and D are arranged anti-clockwise. Here, the x -axis shows the pulse phase, whereas the y -axis is the pulse number. The figure clearly shows drift patterns and their distinct behaviour, representing the four different drift modes.	53
3.2	LRFS and PAPS for the mode A pulse sequence shown in Fig. 3.1. The top panel shows the Longitude Resolved Fluctuation Spectra (LRFS) of the sequence. The bottom panel shows the phase/longitude averaged value of the LRFS, i.e. PAPS. The maximum intensity mark on the top panel corresponds to the peak in the bottom panel. The inverse of this peak frequency position is P_3	55
3.3	A plot of P_3 values for Epoch 1 (top) and Epoch 2 (bottom) of J1822-2256 as calculated using the Phase Averaged Power Spectrum (PAPS). The x -axis shows the pulse number, and the y -axis shows P_3 in units of P_1 . A single block represents a continuous stretch of pulses showing one kind of subpulse drifting mode. The error bars are defined as the inverse of the number of pulses in the respective sequence.	56
3.4	Average profiles of different modes of emission of J1822-2256 at Band 3 (300-500 MHz) and Band 4 (550-750 MHz). The black dashed lines show the average profile, and the rest show the colour-coded average profile for each mode. The profiles are given arbitrary constant shifts along the y -axis for display purposes. Apart from the variation of the profiles across the different modes, the frequency-dependent behaviour of the profiles in each mode can also be observed here.	57
3.5	Plot of the distribution of the P_3 values for J1822-2256 as calculated by PAPS. The different modes are displayed with different colours. The green-dashed data are part of mode B but are due to sequences which were affected by RFI and also showed an apparent lack of emission within the drift band.	59
3.6	Profile of pseudo nulls vs full pulse profile for Band 3 (left) and Band 4 (right).	61
3.7	Plot of mean longitude position of pulse profile components. The points on the left (orange) correspond to the leading components, whereas the points on the right (blue) correspond to the trailing component of the profile.	63

3.8	<i>Top</i> : Average profile of J1822–2256 at 1400 MHz. <i>Bottom</i> : Polarisation Angle fit for 1400 MHz profile of J1822–2256 obtained from Parkes data. The green line denotes the zero crossing point of PA, and the blue line is 180° offset from that.	65
3.9	Plot of emission heights for different modes with frequency. Different colours represent the different subpulse drifting modes.	68
4.1	Wide-frequency spectral evolution of PSR J1820–0427 observed using uGMRT. The figure combines Band 3 (300-500 MHz) and Band 4 (550-750 MHz) observations, with frequency increasing from bottom to top. The colour contrast shows the intensity of the pulsar. Apart from the range between 500-550 MHz, the missing chunks correspond to the persistent RFI channels and are removed automatically.	85
4.2	<i>Left</i> : MWA Stokes I image of the $1 \times 1 \text{ deg}^2$ field (at 185 MHz) with the position of the target pulsar in the centre, with the rms sensitivity is $\sim 500 \mu\text{Jy}/\text{beam}$. <i>Middle</i> : Combined uGMRT Band 3 (300-500 MHz) image of $0.5 \times 0.5 \text{ deg}^2$ field, where the rms sensitivity is $\sim 300 \mu\text{Jy}/\text{beam}$. <i>Right</i> : Combined uGMRT in Band 4 (550-750 MHz) image of $0.15 \times 0.15 \text{ deg}^2$ field, with a much higher sensitivity of $\sim 100 \mu\text{Jy}/\text{beam}$. In all the images, the pulsar is at the phase centre, as indicated by the red circle.	87
4.3	Normalised average profiles of PSR J1820–0427 at all the observed frequencies from 185 MHz to 750 MHz. The 185 MHz observation was made using MWA, while the rest were made using uGMRT. The MWA profile has 512 time bins, whereas the uGMRT profiles are made with 1024 time bins. In the figure, x -axis is the time scale, with the average profile peaks aligned at the centre. The average profiles made using the uGMRT data show the impeccable data quality with off-pulse intensity close to zero. The scattering tail can also be seen at the lower frequencies, and an extra component rising at 185 MHz towards the trailing edge.	93
4.4	Calibrated single pulse train for PSR J1820–0427 at multiple observation frequencies for uGMRT Epoch 1. The high variability of single pulses can be seen, which decreases with higher frequency. A single high amplitude pulse also emerges at higher frequencies (around 2225s), showing a peculiar spectral index.	95

4.5	Pulse fluence histograms for uGMRT observations from Epoch 2. Each panel represents the pulse fluence distribution at a frequency mentioned at the top of each panel. In support of theories like the Stochastic Growth Theory (SGT), we found a log-normal distribution of pulse energies consistent at all frequencies. The histogram is fitted with a log-normal distribution shown as the red curve, with the parameters mentioned in the top right corner of each subplot.	98
4.6	Spectral Index fit for PSR J1820–0427 using flux density values from this work along with the flux density values from the published literature. The black dashed line is the best-fitting model to the data, and the orange shaded envelope is the 1σ uncertainty of the best-fitting model. The turn-over frequency was found to be ~ 170 MHz, and the spectral index is -2.34 ± 0.01 . In contrast with the previous studies, the power law with a low-frequency turn-over (dashed line) fits the data best for this pulsar. . .	100
4.7	Measured scattering delay vs the observing frequency for PSR J1820–0427; using a thick screen model for scattering, as described in the text. The black line in the plot is a power-law fit of the form $\tau_d \propto \nu^{-\beta}$, to the complete observed data. The red line shows a fit to only uGMRT Band 3 data. The green dashed line shows the frequency scaling for Kolmogorov turbulence, and the blue dashed line is for the empirical index favoured by a large body of measurements as shown by Bhat et al. (2004).	102
4.8	The measured pulse at 185 MHz using MWA is shown in black. The curve in blue shows the scattering function, which was chosen to be an exponential pulse broadening function with a rounded shape (thick scattering screen). The red curve is the reconstructed pulse profile and clearly shows a secondary feature emerging at the tail end, near time 0.4. .	104
4.9	Flux vs flux plot between 725 MHz (x-axis) and other frequencies (y-axis). Contours show the lines of constant spectral index. The plot shows a tighter correlation between close frequency pairs. There also appears to be an upward trend for high-intensity pulses, indicating a steeper spectral index and a possibly different emission mechanism.	111
5.1	Each pulse stack (Pulse phase vs Pulse number) represents the variety of subpulse drifting sequences shown by PSR J0026–1955 at 400 MHz (using uGMRT). Bright yellow diagonally arranged pixels around to phase 0° are the drift bands. The pulsar exhibits both short and long nulls, where no emission can be seen in the on-pulse region.	123

5.2	Pulse stack with drift bands (<i>yellow bright subpulses</i>) modelled using linear and exponential models (<i>white lines</i>). The evolution of drift rates can be seen in modes A1 and A2. The inter-modal drift band connectivity is also apparent in most cases.	124
5.3	For the MJD 59529 scan 2 observation of J0026–1955, the above plot shows the drift rates as obtained using the linear and exponential drift rate models discussed in section 5.2.1. Some of the corresponding drift band fits are shown in Fig. 5.2.	128
5.4	Average modal profiles of subpulse drifting modes exhibited by J0026–1955. Note that the average profiles of modes A0 and A1 are very similar. However, for modes A2 and B, the profiles are comparatively wider. . . .	129
5.5	Peak flux density within the on-pulse window as a function of time for the six uGMRT observations at 400 MHz. The shaded grey regions show detected subpulses. The unshaded region corresponds to nulls and RFI occurrences. The peak fluxes were measured after smoothing the time series with a Gaussian filter (1σ) to suppress the noise contribution and accentuate the contrast between nulling and burst sequences.	132
5.6	In the top panels of all sub-figures, the red dots show the location of subpulses, while the green lines correspond to fits to drift bands using a cubic smoothing spline method. In the lower panels, the black solid lines show the drift rates ($^{\circ}/P_1$) of individual drift bands, while the solid grey line shows the average drift rate. The figures represent only a few drift sequences.	134
5.7	The figure shows a distribution of drift rates ($^{\circ}/P_1$) for different modes. The topmost panel shows the combined distribution, and the lower panels show the drift rates for individual modes.	136
5.8	For the same observation of J0026–1955 shown in Fig. 5.3, the above plots show the quartic drift rate model fits. Using the cubic smoothing spline method, we calculated the drift rate ($^{\circ}/P_1$) at each pulse number, which is shown using the blue dots. The black line shows the average drift rate per pulse number. Drift rates for each of the modes are fit using a quartic polynomial, which describes a global evolution of drift rates. The colour scheme in the lower panel is similar to Fig. 5.7	138

- 5.9 The figure combines all the drift rate fits using the quartic polynomial. The black line shows the average of all drift rates, and the grey envelope shows the 1σ deviation around the mean. *Left:* Drift rate for mode A0 stays constant on average despite sudden changes, as shown by the black line. *Middle:* Mode A1 is an evolutionary mode where the drift rate evolves from faster to slower drift rates. This is also shown by the black line, which evolves from an average drift rate of $\sim -1.3^\circ/P_1$ to $\sim -0.5^\circ/P_1$ with pulse number. *Right:* The evolutionary behaviour of mode A2 is the opposite of mode A1, where it evolves from a slower to a faster drift rate towards the end. In this plot, we have plotted the drift rates such that all drift sequences end together. This exercise shows the claimed drift rate behaviour. Following the trend of the black line (average drift rate), one can note that the drift rate evolves from $\sim -0.5^\circ/P_1$ to $\sim -2.0^\circ/P_1$ 140
- 5.10 Examples showing speculative drifting during nulls for J0026–1955. *Top:* Between the two drifting sequences, there is a single burst at 1703. Extrapolating the drift rates of the first sequence (pulse 1683 to 1694) aligns well with the drifting behaviour at later pulse numbers. The drift band fits are shown to illustrate the approximate locations of the missing driftbands. *Bottom:* Between the four drifting sequences, though the drift rates may not align, the phase memory of the last burst before nulls is almost retained. 141

List of Tables

3.1	Details of observation of J1822-225 using uGMRT	51
3.2	Drift mode measurements of J1822–2256	52
3.3	Carousel parameters for J1822–2256	71
4.1	Table of observations for PSR J1820–0427	83
4.2	Multi-frequency flux density measurements of J1820–0427 obtained from imaging the pulsar field using MWA (185 MHz) and uGMRT(317-725 MHz). The flux densities and their respective errors are added in quadrature for multiple epoch observations. Data at 483 MHz was unusable and was discarded for this work. At Epoch 2, data at 383 MHz was unusable, thus only the values from Epoch 1 were used.	88
5.1	Table of observations for PSR J0026–1955.	121

List of abbreviations

PSR	Pulsar Source
uGMRT	upgraded Giant Metrewave Radio Telescope
MWA	Murchison Widefield Array
DM	Dispersion Measure
RFI	Radio Frequency Interference
ISM	Inter-Stellar Medium

Chapter 1

Introduction

“Geronimo!”

- The Doctor

Roughly ten thousand years ago, a star exploded in a distant part of the Milky Way galaxy, far from our solar system. The light from this explosion took around 8000 years to reach Earth, and in 185 AD, it appeared as a prominent spot in the northern sky. The unusual event was recorded by Chinese astronomers during the Han Dynasty and documented in the Book of Later Han. This marked the earliest historical documentation of a “guest star”. Humanity witnessed several such guest stars throughout the centuries before their true nature was understood.

Fast forward to the early 20th century, a period marked by tremendous scientific advancement. Relevant to this thesis is the discovery of the neutron, an uncharged subatomic particle, by James Chadwick, in 1932 ([Chadwick, 1932](#)). In 1934, building upon this breakthrough, astronomers Baade and Zwicky proposed the concept of a *supernova*, the explosive death of a massive star leading to the formation of a “neutron star” ([Baade](#)

& Zwicky, 1934). The supernova is an explosion which occurs at the final stages in the life cycle of a massive star, producing cosmic rays and leaving behind a star comprising predominantly of neutrons. This star was hypothesised to have a small radius, an enormous matter density, and neutrons as its main constituents.

It was subsequently realised that the “guest star” recorded in 185 AD was, indeed, a supernova event (Zhao et al., 2006). However, observational evidence for the existence of neutron stars remained elusive. This mystery was eventually unravelled three decades later, in 1967, by a Cambridge graduate student named Jocelyn Bell Hewish et al. (1968). While analysing her data, she detected a faint, regular radio signal emanating from an unknown origin, labelled CP 1919 (different from the guest star of 185 AD). The new astrophysical object was termed - “pulsar”, a shortened analogue of pulsating star. Further research revealed that pulsars belong to the category of fast-rotating, highly-magnetised neutron stars, which have energetic beamed radiation coming from their magnetic poles.

1.1 Pulsars

Pulsars were discovered through their highly periodic individual pulses, as reported by Hewish et al. (1968). Although most pulsars emit continuously along their magnetic axes, it is their rotation that causes their emission to be visible briefly as it intersects our line of sight, producing the characteristic pulsed signal (Gold, 1968). Typically, the magnetic axis is inclined with respect to the pulsar’s rotational axis. Therefore, each time a pulsar rotates, the radiation beam produced near the magnetic poles is swept at an angle across the sky, similar to a lighthouse. If the beam crosses the line of sight of an Earth-bound observer, the pulsar becomes detectable as a rise and fall in the observed intensity. With each pulsar rotation, this pattern repeats periodically. It was such single pulses that Jocelyn Bell detected in her first recording of the pulsar CP 1919 on November 28, 1967.

Neutron stars are incredibly dense stellar remnants formed when stars with masses

more than $\sim 8M_{\odot}$ reach the end of their life cycle, and their core collapses under gravity. Neutron stars have a typical mass of $1.4M_{\odot}$ (e.g., [Chandrasekhar, 1931](#); [Kiziltan, 2011](#)), condensed into a sphere of approximately 20 km in diameter. The physical conditions inside a neutron star are very different from laboratories on Earth, with densities reaching up to $10^{14} \text{ g cm}^{-3}$. A wealth of predictions about neutron stars were already made before their eventual discovery as pulsars. However, the possibility that such bizarre objects might have detectable radio emission was not considered.

Because these stellar remnants retain most of the angular momentum of their progenitor star during the collapse, they rotate rapidly, with rotation periods ranging from ~ 1.4 milliseconds for the fastest known pulsar ([Hessels et al., 2006](#)) to the slowest known pulsar with a period of 76 seconds ([Caleb et al., 2022](#)). The collapse of the parent star in a supernova event concentrates the magnetic field of the remnant immensely, reaching around the order of 10^{12} Gauss (e.g., [Cordes et al., 2004](#); [Kaspi, 2010](#)). The observed emission from radio pulsars takes place at the expense of the rotational kinetic energy of the neutron star. As a result, in addition to observing the pulsar's spin period, P_1 , we also observe the corresponding rate of spin-down, \dot{P}_1 , as the pulsar slowly loses its energy. Thus, pulsar rotational periods increase as their spin gradually slows down, as rotational energy is lost through the large amounts of magnetic dipole and electromagnetic radiation they emit throughout their lifetimes ([Lorimer, 2009](#)).

Since the discovery of the first pulsar ([Hewish et al., 1968](#)), over 3000 pulsars have been found within our Galaxy. However, despite decades of extensive observational and theoretical investigations, several open questions remain in this fascinating field. For example, the exact physical mechanism which gives rise to the coherent emission of electromagnetic radiation from these objects is still not well understood; the dynamics and structure of pulsar magnetospheres are still not well comprehended; the interior structure and composition of the extreme core density remains an intriguing question; and the pulsar distribution, formation, and revolutions an area of ongoing investigation.

In this thesis, the main focus is on understanding the pulsar emission mechanism, which remains one of the crucial open questions. Despite several proposed theoretical ideas and physical models, the exact mechanism responsible for generating and beaming the radiation still lacks a satisfactory explanation. Newer observations continue to uncover more intricate details of emission phenomenology, sometimes challenging our current understanding of pulsar emission physics. As these regimes are continuously explored, we can expect to gain deeper insights into the nature of pulsars and their underlying physics.

1.2 Observed pulsar signal

As pulsars are generally weak radio sources, their detection often needs telescopes with large collecting areas, high sensitivity, and high time resolution. A subset of pulsars is also known to emit at wavelengths other than radio (e.g., [Cocke et al., 1969](#)); however, throughout this thesis, we will focus on radio pulsars.

Radio emission from pulsars is observed using dedicated radio antennas or an array of radio telescopes that are specifically designed to amplify weak radio signals. A radio antenna or a radio telescope can be used to receive signals, which can then be viewed on an oscilloscope or even connected to a loudspeaker (after a down-conversion).

A telescope observing pulsars records the incident electromagnetic radiation over a set bandwidth with a certain time resolution. The signal observed by such a radio telescope can be described as - intensity as a function of frequency and time, referred to as a *dynamic spectrum*. Owing to the impeccably periodic behaviour of pulsars, the observed pulsar signal appears temporally pulsed at, on average, an extremely regular period, as shown in Fig. 1.1. The typical widths of individual pulses are only a fraction of the pulsar period. There is also large pulse-to-pulse variability in amplitude as well as other properties. These individual pulses are thus a marker of the dynamic pulsar

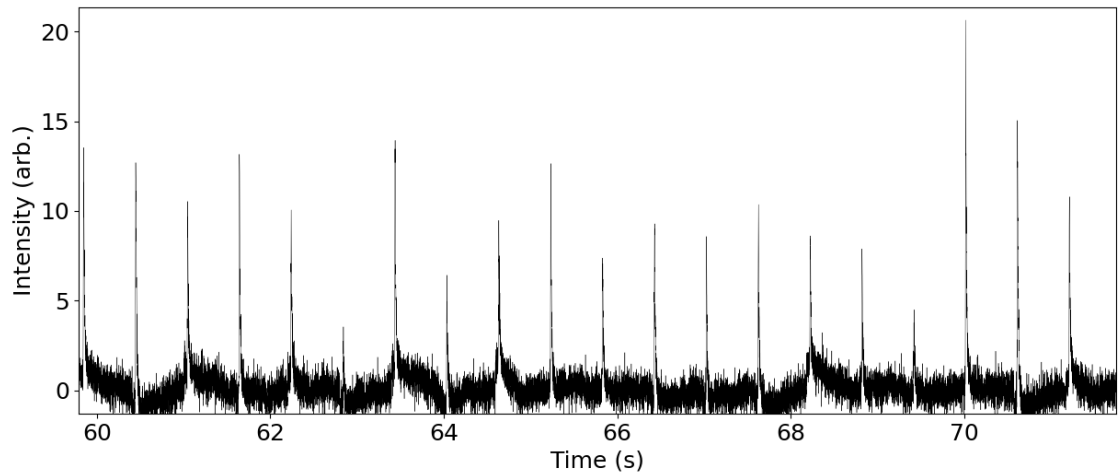


Figure 1.1: Sequence of 20 consecutive pulses observed from PSR J1820–0427 using the upgraded Giant Metrewave Radio Telescope at 317 MHz. The x -axis shows the time elapsed in seconds since the beginning of the observation.

magnetosphere and can provide essential clues for understanding pulsars (Cairns et al., 2003c). Pulsar observations generally rely on the recognition of the precise periodicity in a pulsar radio signal.

The average time difference between consecutive pulses is identified as the pulsar rotation period, P_1 . Hence, it is of interest to view the data as a function of the rotation phase rather than a time series. For this, consecutive single pulses are stacked to form a two-dimensional image. This is shown in Fig. 1.2, where the x -axis shows the rotation phase (0° to 360°) and y -axis shows the pulse number. The time series of ~ 6000 pulses is plotted in a colour scale, forming a 2D stack of single pulses. The colour scale represents the intensity and can be noted to be higher towards 0° , i.e. when the pulsar is pointing towards the observer. The variability in single pulse amplitudes can also be easily seen here.

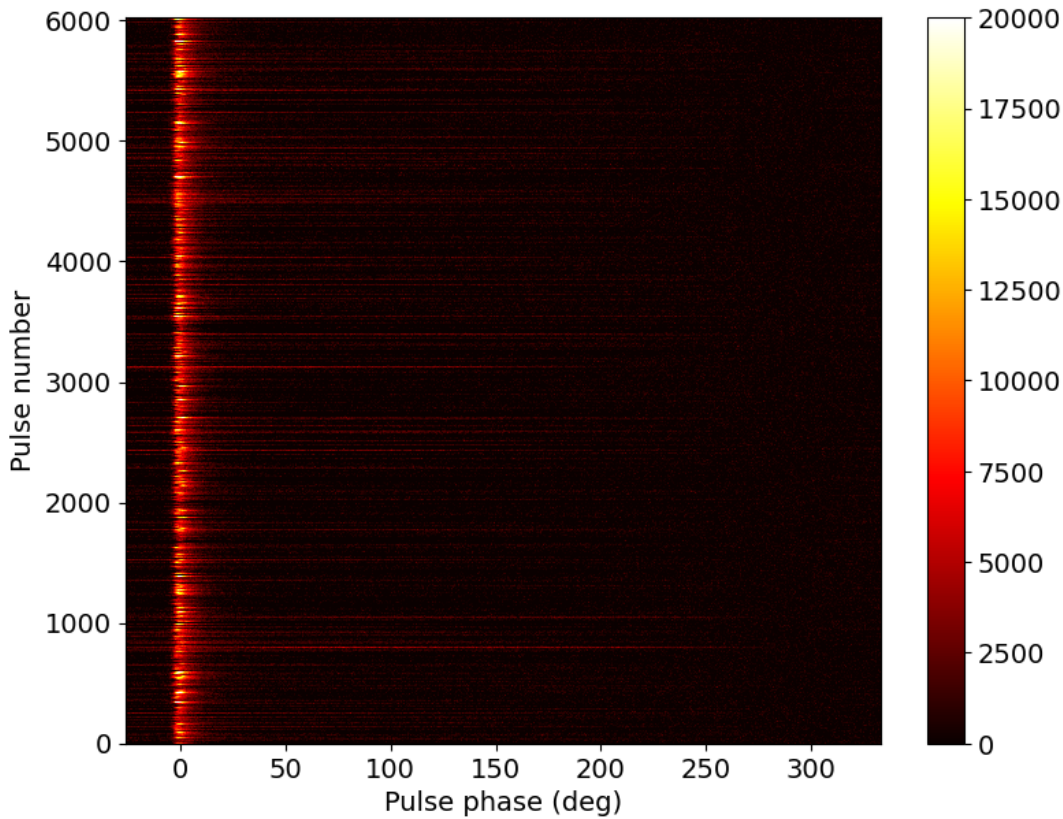


Figure 1.2: Consecutive single pulses are stacked to form a two-dimensional pulse stack showing variability in pulsar signal over time (y -axis; pulse number) and phase (x -axis). The figure shows a pulse stack of over 6000 pulses observed for PSR J1820–0427 at 317 MHz, using uGMRT.

1.3 Integrated pulse profiles

At a given frequency, for the same pulsar, every single pulse, if observable, is vastly different from each other in general, which speaks about the dynamic nature of the pulsar emission process (see Fig. 1.1 and 1.2). However, as most pulsars generally have low levels of detectable emission, a coherent addition of multiple pulses is required to observe a discernable emission. If a large number of single pulses ($\sim 10^3$) from a pulsar are superimposed, then the resultant is called an *integrated profile*. This process of averaging the intensity at each rotation phase is called folding, which essentially represents an average

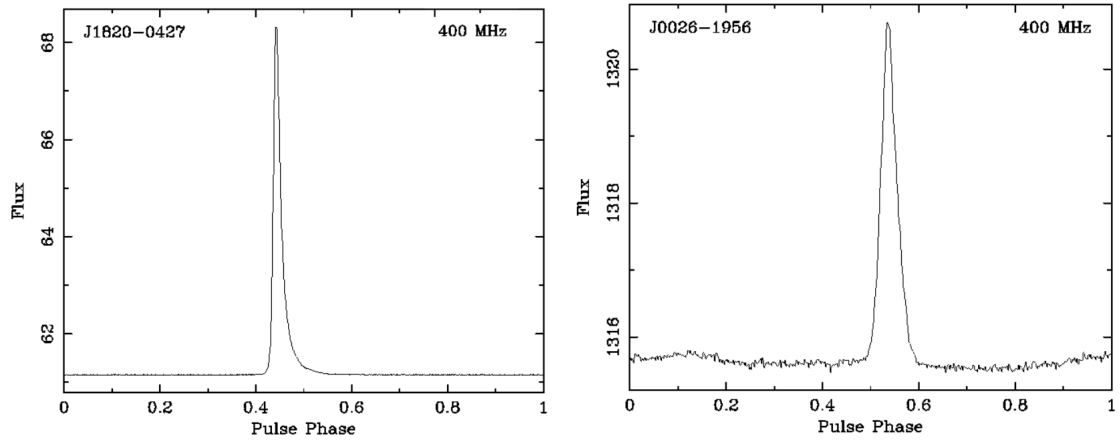


Figure 1.3: Average profile of PSR J1820-0427 (left) and PSR J0026-1955 (right) at 400 MHz integrating ~ 6000 and ~ 2500 single pulses, respectively. The pulse phase on x -axis is synonymous to pulse phase from 0° to 360° . The flux on the y -axis is in arbitrary units.

statistical variation of single pulse intensity across the pulse phase. For most pulsars, this integrated profile is far from a simple Gaussian shape. Instead, each pulsar produces a unique pulse emission pattern contributing to its average profile, somewhat akin to a fingerprint (Lorimer, 2008). The difference in the shape of each pulse profile is due to the size and geometry of the emission beam, as well as the angle between the line of sight and the beam. Fig. 1.3 shows the average profile of two specific pulsars: J1820-0427 and J0026-1955, the detailed properties of which are investigated in this thesis. A few differences between the integrated profiles of the two pulsars are immediately noticeable: (1) the profile on the left is smoother due to more number of pulses being averaged, (2) the profile on the right looks more like a Gaussian than the left one, which seems to have a tail. Generally, pulsar profiles have features which often change with frequency, which is taken as evidence for the *radius-to-frequency* (RFM) mapping, where the frequency of emission behaves as a function of the emission height above the pulsar surface (Cordes, 1978). Thus, pulsar profiles generally have a tendency to be broader at lower frequencies, such that the emission comes from higher emission heights and vice-versa. Over time, for some

pulsars, the integrated pulsar profiles also change due to mode changing, a phenomenon known since the early days of pulsar research (e.g. [Bartel et al., 1982](#)). Until recently, little observational evidence was seen for profile changes over time in millisecond pulsars, but there are exceptions to it, for e.g., [Singha et al. \(2021\)](#).

The average profile of a pulsar reflects the time-integrated outlook of the variable plasma processes occurring within the magnetosphere. The average properties provide information about the magnetospheric properties, such as mean flux density, viewing geometry, emission beam structure, etc. The profile shape also exhibits gradual variation depending on the observing frequency ([Hankins & Rickett, 1986](#)). The emission at different frequencies not only reveals the spectral behaviour but also can be exploited to sample the emission from different heights in the pulsar magnetosphere ([Cordes, 1978](#)).

Generally, individual pulses are not bright enough to be observed above the background noise. Hence, the study of single pulses is limited to pulsars for which sufficiently bright pulses can be observed in the frequency range of interest.

1.4 Propagation effects

The observed pulsar signal is a combination of the intrinsic pulsar emission and any distortions it may have encountered en route to the observer as it passes through the interstellar medium (ISM). These distortions arise from various propagation effects, including diffraction and refraction in the ISM, which depend on the observation frequency. Many of these effects are well observable using pulsed signals, making pulsars useful sources for exploring the interstellar medium. Nonetheless, some of these effects can be mitigated to retrieve the original signal. In the context of this thesis, we will focus on the propagation effects observed at radio frequencies.

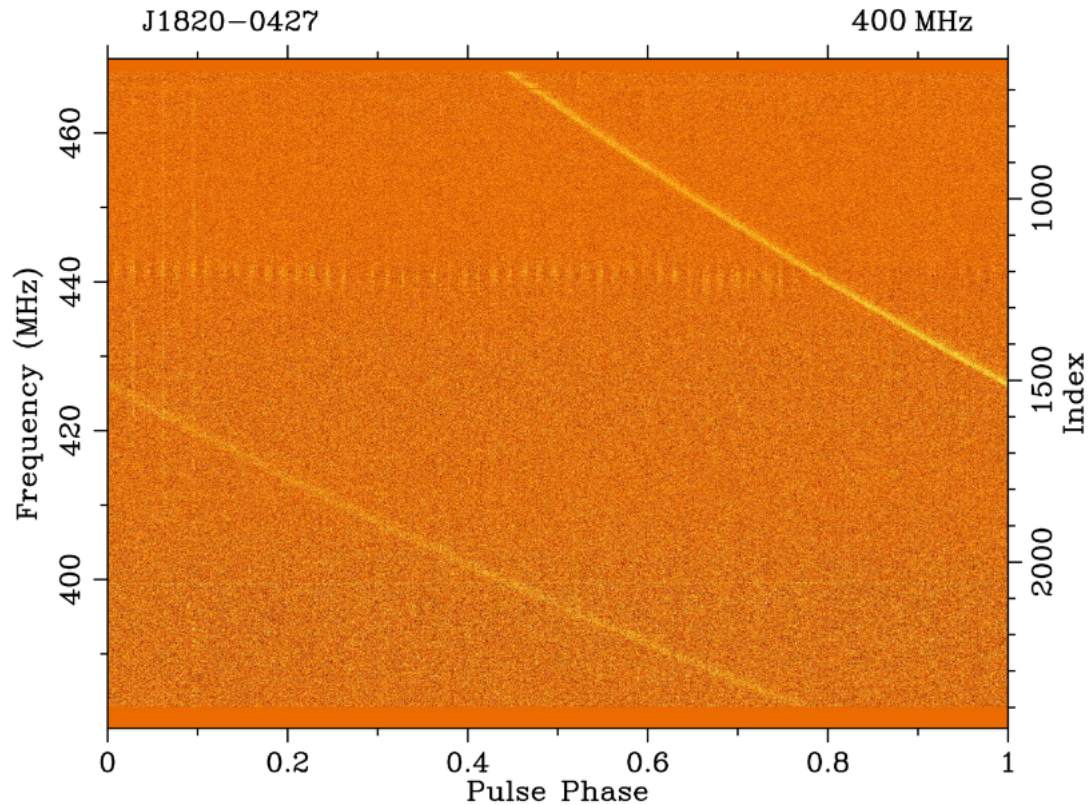


Figure 1.4: The effect of dispersion on a single pulse from J1820-0427 observed using uGMRT. Due to the intervening ISM, the pulsar signal at a higher frequency arrives before the signal at a lower frequency. The colour scale pattern shows the uncorrected dispersed signal as a function of the observing frequency.

1.4.1 Dispersion

As the pulsar radiation passes through the cold, ionised plasma in the ISM, it gets refracted. The refractive index is frequency dependent, leading to a change in the group velocity of radio waves, causing the lower frequency radiation to travel slower than the higher frequency radiation. Consequently, the pulsar signal at higher radio frequencies reaches the telescope earlier compared to that at lower frequencies. The spread in delays in pulse arrival times due to this effect across a finite bandwidth can be seen in Fig. 1.4, where

the pulsar signal at higher frequencies arrives earlier, and that of lower frequencies arrives later. The time delay due to this dispersion, i.e. the dispersion delay (τ), is defined as (e.g., [Lorimer & Kramer, 2004](#))

$$\tau(\nu) = \mathcal{D} \times \frac{\text{DM}}{\nu^2} \quad (1.1)$$

where ν is the observation frequency and \mathcal{D} is the dispersion constant, given by

$$\mathcal{D} \equiv \frac{e^2}{8\pi^2 m_e \epsilon_0 c} \quad (1.2)$$

with e as the electron charge, m_e as the electron mass, and ϵ_0 as the permittivity of free space. The dispersion measure, DM, is defined as

$$\text{DM} = \int_0^d n_e(l) dl \quad (1.3)$$

where $n_e(l)$ is the electron number density along the line of sight, and d is the distance between the pulsar and the observer. Thus, DM represents the column density of electrons along the entire path length, measured in units of pc/cm^3 .

The dispersion delay (τ) is useful for estimating the distances to pulsars. By comparing the arrival times of pulses at different radio frequencies, it is possible to obtain an estimate of the pulsar distance if information about the distribution of electron density along the line of sight is available. The density of free electrons is higher at lower Galactic latitudes ($|b| \lesssim 15^\circ$) than at higher latitudes. Thus, pulsars in the Galactic disk (lower Galactic latitudes) tend to have higher DMs than pulsars located above the Galactic disk. The commonly used electron density model for measuring a pulsar's DM is NE2001 ([Cordes & Lazio, 2002](#)), which also models the distribution of turbulent plasma in the Galaxy. Other models, such as [Yao et al. \(2017\)](#), are primarily electron density models.

The dispersion smearing of pulsar signals due to the ISM can be effectively mitigated through dedispersion, which is performed using two different methods: incoherent dedispersion and coherent dedispersion. In the case of incoherent dedispersion, the signal delays in individual frequency channels are compensated such that the pulsar signal arrives

simultaneously at all frequencies. On the other hand, for coherent dedispersion, a model of the ISM (e.g., NE2001) is employed to reverse the phase delays caused by dispersion.

1.4.2 Scattering

Due to the inhomogeneities and the refractive nature of the ISM, the incident radiation from pulsars is scattered and traverses different paths to the observer. Consequently, the radiation reaches the observer over a spread of arrival times (e.g., [Salpeter, 1969](#); [Scheuer, 1968](#)). As a result, the pulse, as received by the observer, is smeared across time. This temporal broadening is more pronounced at lower frequencies. If we consider the simplest model, where the scattering originates from a single location between the pulsar and the Earth, the result is a one-sided broadening of the pulse, observationally manifesting as an exponential tail. This can be clearly seen in [Fig. 1.5](#), where the measured pulse is observed simultaneously at multiple frequencies. As seen from the figure, the pulse is comparatively less scattered at the highest observed frequency (725 MHz) and more at lower frequencies. However, the overall flux (integrated emission) of a single pulse will still be conserved. The scattering delay (τ_s) induced by this observational effect scales with frequency (ν) as

$$\tau_s \propto \nu^\alpha \tag{1.4}$$

where $\alpha = -2\beta/(\beta - 2)$ with β being the slope of the power spectrum. Assuming a Kolmogorov distribution for the irregularities, where the irregularities in the ISM electron density follow a specific power-law dependence with $\beta = 11/3$, the scattering time scale theoretically obeys the proportionality ([Cordes et al., 1985](#)),

$$\tau_s \propto \nu^{-4.4} \tag{1.5}$$

Thus, the scattering time scale can be substantial at lower frequencies compared to that at higher frequencies ([Fig. 1.5](#)). Furthermore, in some cases, τ_s can be larger than the pulsar rotation period (P_1), in which case part of the flux from one pulse may get mixed

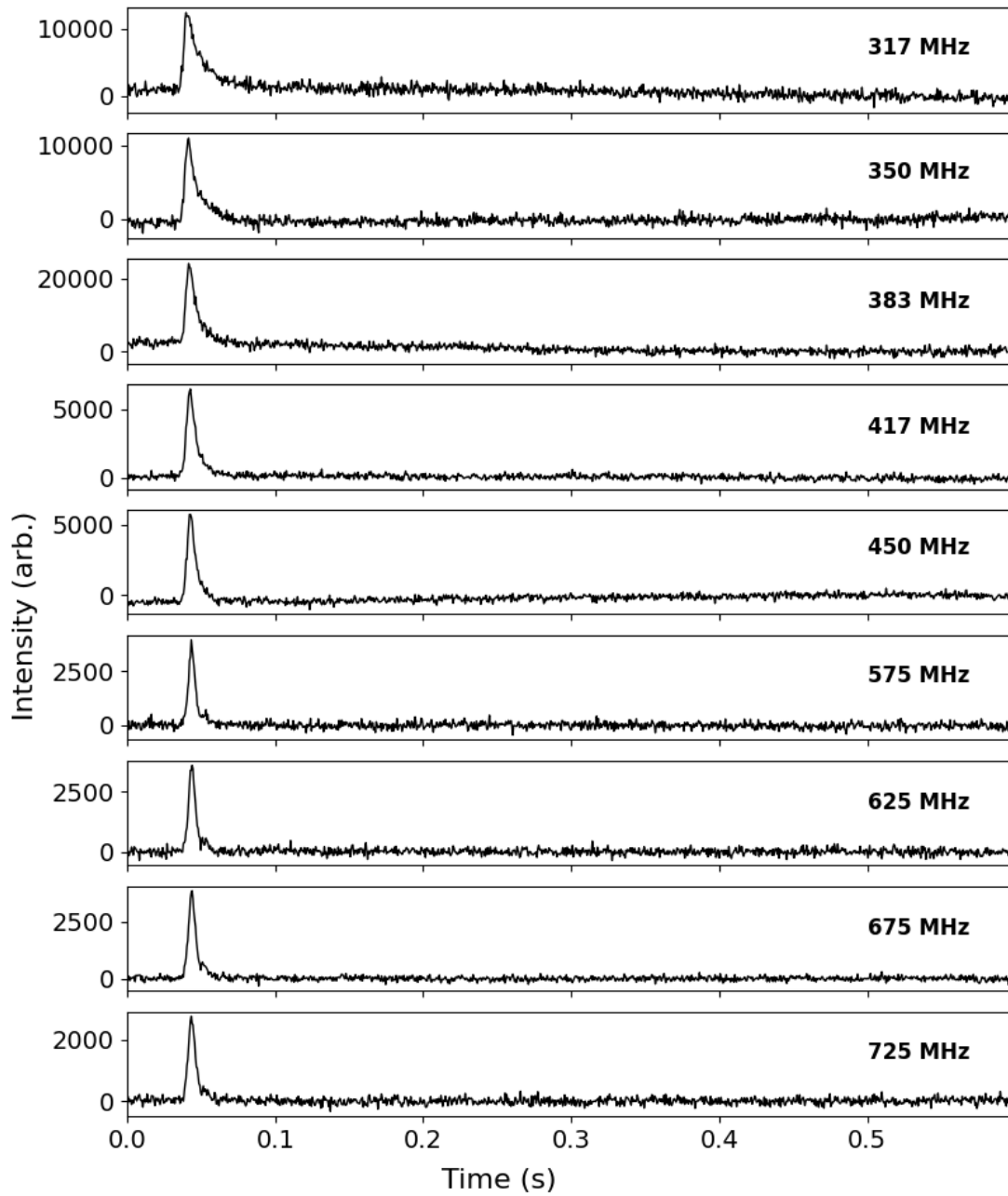


Figure 1.5: Scattering of a single pulse from PSR J1820–0427, simultaneously observed at 300–750 MHz from uGMRT. An increase in scattering time towards lower frequencies can be clearly noted.

with that from the successive pulse, making it difficult to observe some of the very distant pulsars ($DM \gtrsim 500 \text{ pc/cm}^3$) at lower frequencies.

The shape of a scattered pulse profile and its variation with frequency provides valuable information about the structure, behaviour, and properties of the ISM. Particularly, as the impact of scattering due to ISM is more pronounced at lower frequencies ($\nu \lesssim 300 \text{ MHz}$), studies of scattering in pulsar profiles at low frequencies can be very useful in distinguishing between different models of the ISM.

1.4.3 Scintillation

Another consequence of multipath propagation of radio waves from the pulsar through the turbulent and inhomogeneous ISM is the interference between scattered wavefronts as they reach the observer (e.g., [Lang, 1971](#)). The net superposition of the incident wavefronts can be constructive or destructive interference, which leads to large pulse intensity fluctuations, as seen by the observer. Moreover, the interference pattern shifts across the observer's plane due to the relative motion between the observer, pulsar, and ISM. This scintillation phenomenon is essentially an analogue of the optical twinkling of stars caused by the Earth's atmosphere ([Narayan, 1992](#)).

The observed modulation in intensity is a function of both time and frequency and hence, the two observable quantities of interest are the scintillation time scale and scintillation bandwidth, which are essentially the average time scale and bandwidth of intensity modulations in time and frequency. Scintillation generally occurs at time scales much longer than pulsar rotation periods (P_1), especially at frequencies $\gtrsim 100 \text{ MHz}$. [Fig. 1.6](#) shows an example of scintillation for PSR J0026–1955 in the 400-450 MHz frequency range, where the pulsar intensity is seen to vary across time and frequency. The observed emission from the pulsar is bright at certain frequencies for some duration of time, for e.g., over ~ 25 minutes near $\sim 420 \text{ MHz}$.

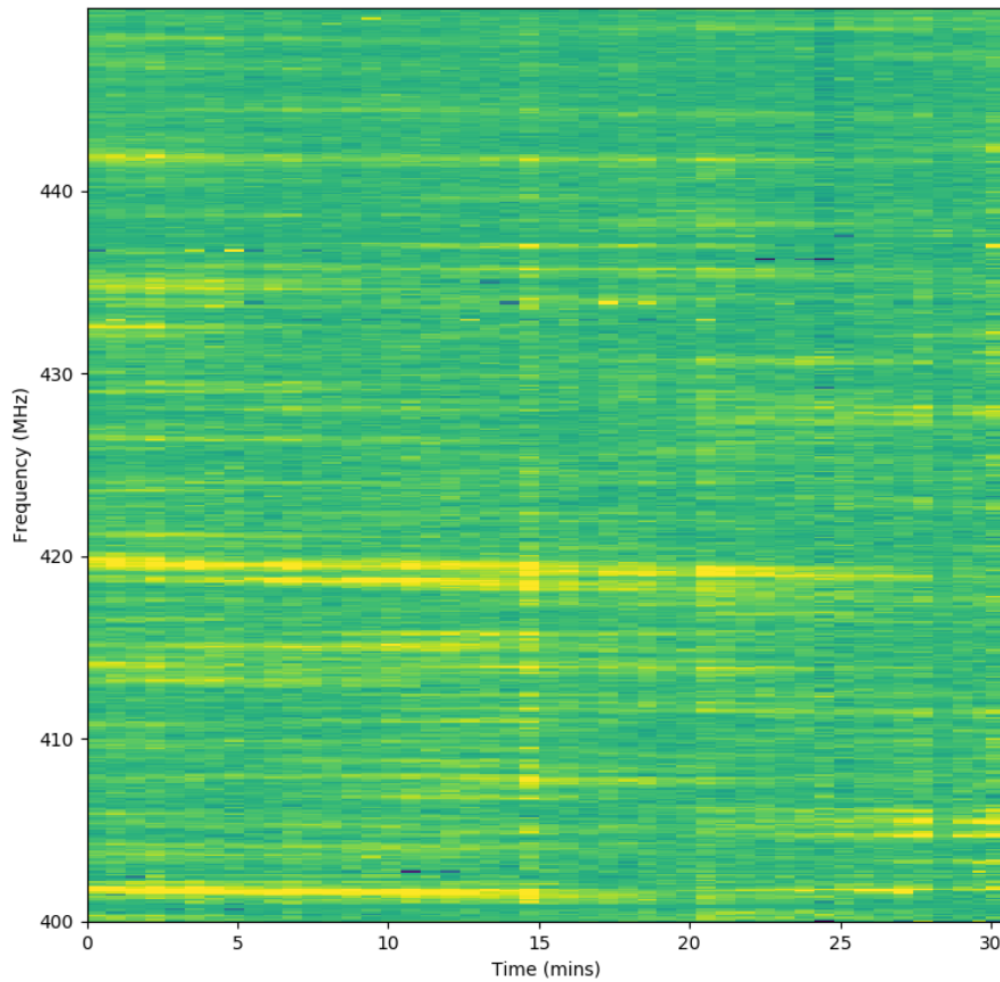


Figure 1.6: Dynamic spectrum of PSR J0026–1955 in a 50 MHz subband, observed from uGMRT. The colour scale represents the intensity of the observed pulsar signal. It can be noted that the pulsar is not uniformly bright at all frequencies across the observed time range.

1.5 Variability in intrinsic pulsar emission

After accounting for all the propagation effects that the pulsar radiation encounters as it traverses through the ISM, the resulting dynamic spectchattrum is expected to be close to the actual pulsar emission. This intrinsic pulsar emission is highly stochastic in nature and is known to exhibit a variety of modulations in pulse amplitudes or phase and even

in structure and polarisation at multiple different time scales. Some of these phenomena, particularly those relevant to this thesis, are described in the following sections.

1.5.1 Pulse-to-pulse amplitude modulation

The amplitude modulation in single pulses of radio pulsars can be affected by both intrinsic and extrinsic factors. Depending on the time scale of observation, pulsars can exhibit different types of variability in their amplitude, for e.g., micro-structures (e.g., [Craft et al., 1968](#)), giant pulses (e.g., [Heiles & Campbell, 1970](#); [Staelin & Reifenstein, 1968](#)), giant micro-pulses (e.g., [Johnston et al., 2001](#)), moding (e.g., [Backer, 1970a](#)), to name a few. Additionally, some pulsars may stop emitting for a certain duration of time, and this is referred to as nulling (e.g., [Backer, 1970b](#)). All these fall under intrinsic variability, and they manifest as a result of time-variable plasma processes in the pulsar magnetosphere, which can be most meaningfully investigated using a detailed analysis of a time series of a large number of pulses. An example of the amplitude modulation in pulsars is shown in [Fig. 1.1](#).

For many pulsars, the distribution of pulse energies follows a log-normal distribution. For example, [Burke-Spolaor et al. \(2012\)](#) find that a significant fraction of their observed sample exhibited a log-normal pulse energy distribution, while only a few displayed a Gaussian pulse energy distribution, while some did not follow any of these distributions. Studying the energetics of single pulses can help provide insights into theoretical pulsar emission models. For example, if the pulsar emission mechanism gives rise to random modulation of pulse intensity, then one may expect a Gaussian distribution of pulse energies. However, any deviation from a Gaussian distribution might indicate a non-random distribution of intensities and, consequently, a more complex emission mechanism.

Observations of single pulses at multiple different frequencies allow us to not only sample different regions of the magnetosphere (Radius to Frequency Mapping; [Cordes, 1978](#)) but also understand the energetics as a function of time and frequency, ultimately

providing useful clues for possible emission mechanisms. Such studies can provide useful means of studying the pulsar magnetosphere and are, therefore, crucial in gaining insights into the variable pulsar emission process. Chapter 4 presents our work on the single pulse modulations in pulsar PSR J1820–0427 using high-quality radio data obtained using the Murchison Widefield Array (MWA) and the upgraded Giant Metrewave Radio Telescope (uGMRT) spanning a frequency range of ~ 170 to 750 MHz.

1.5.2 Subpulse Drifting

Sometimes the individual pulses may also have discrete substructures called ‘subpulses’. These subpulses are regarded as the fundamental components of emission originating from discrete sources within the magnetosphere, and therefore their longitude locations within the pulse window can be interpreted in terms of the physical distribution of emission at the polar emission region. [Drake & Craft \(1968\)](#) were the first to observe the systematic ‘marching’ of these subpulses with phase within the on-pulse window, generally noticeable in a 2D pulse stack. This phenomenon is called subpulse drifting, where the discrete bursts of emission within the pulse window are referred to as ‘subpulses’, and ‘drifting’ refers to the systematic way subpulses arrive earlier or later in successive pulsar rotations leading to diagonal drifting structures in a pulse stack (pulse number vs rotation phase). An example of subpulse drifting as observed in pulsar PSR J1822–2256 is shown in [Fig. 1.7](#).

Subpulse drifting offers unique insights into the underlying emission mechanism in pulsars. The Westerbork surveys by [Weltevrede et al. \(2006, 2007\)](#), and more recently by MeerKAT ([Song et al., 2023](#)) have revealed that a significant fraction of slow pulsars exhibits subpulse drifting alongside pulse-to-pulse variability in the form of amplitude modulation, as described in the previous section. This secondary modulation can provide valuable insights into the complex magnetic field configurations, the structure and dynamics of the pulsar magnetosphere, and the emission processes that govern the observed radiation (e.g., [Bhattacharyya et al., 2009](#); [Bilous, 2018](#); [McSweeney et al., 2017](#)).

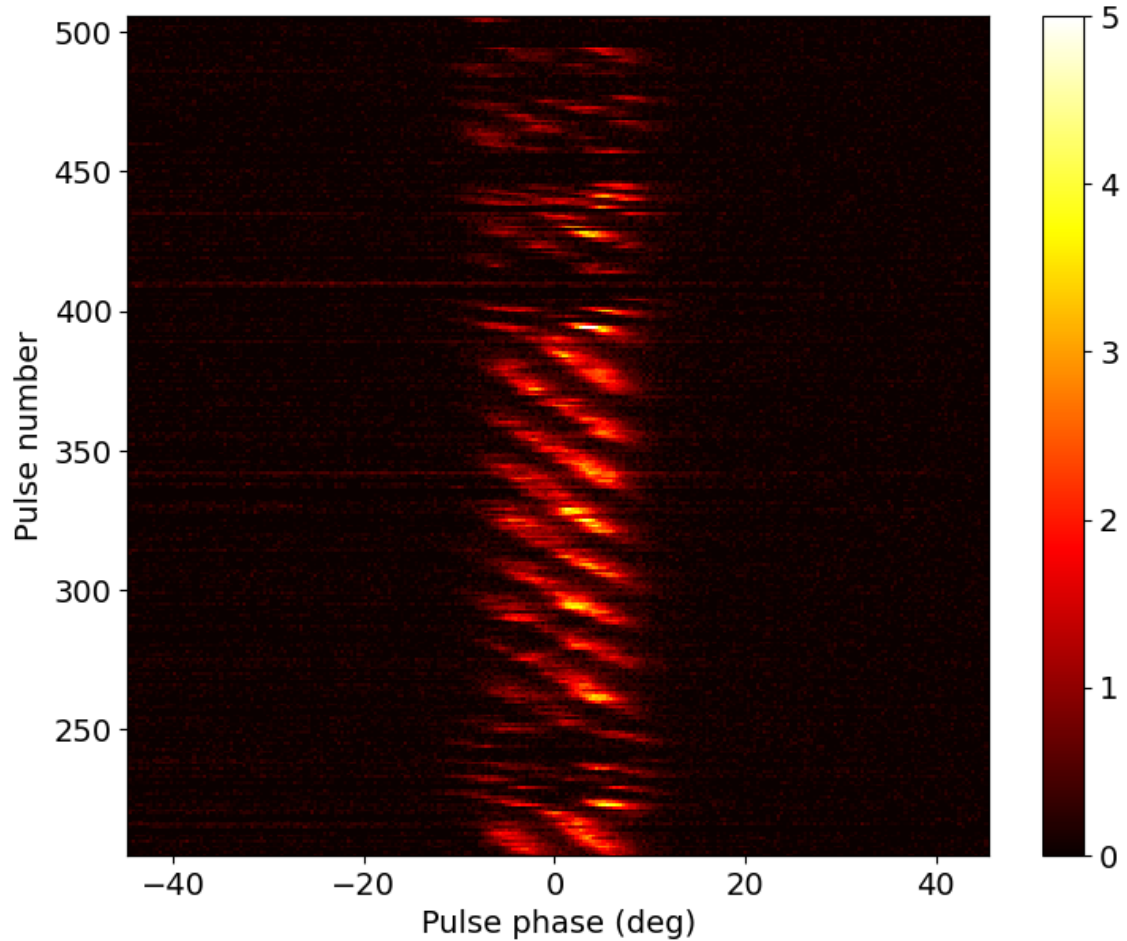


Figure 1.7: A pulse stack of PSR J1822–2256 using observations from uGMRT at 300–500 MHz. Within the on-pulse region, around phase 0° , the pulsar can be seen to exhibit subpulse drifting. It is also known to show multiple kinds of subpulse drifting modes, each with different P_2 and P_3 . A detailed study of the wideband behaviour of the subpulse drifting phenomenon in J1822–2256 is presented in chapter 3.

1.5.2.1 Characterisation of drift bands

In the pulse stack, as shown in Fig. 1.7, the associated sets of subpulses form diagonal structures called *drift bands* that stretch across the on-pulse window. For pulsars with well-defined drifting features, the drift bands can be characterised by the following three basic quantities:

1. **P_2** : The horizontal distance, i.e. the temporal separation between successive sub-pulses within a single pulse, is measured as P_2 , in units of longitude ($^\circ$).
2. **P_3** : On a pulse stack, the vertical separation between drift bands at a given longitude is P_3 , which is measured in units of pulsar rotation period (P_1). Observationally, it is the number of pulsar periods it would take for a subpulse to arrive at the same rotation phase.
3. **Drift rate**: The drift rate is defined as $D = \Delta\phi$ per pulse period ($^\circ/P_1$), where $\Delta\phi$ is the longitude shift in degrees during one pulse period P_1 . Simplistically, it can be visualised as the slope of a drift band.

The drift rate is related to P_2 and P_3 as

$$\frac{D}{P_1} = \pm \frac{P_2}{P_3} \quad (1.6)$$

where all the quantities are in the units of time, and the sign indicates the direction of the drift. A positive value of drift rate indicates a drift from early to later longitudes, while a negative value corresponds to a drift from later to earlier longitudes.

For many subpulse drifting pulsars, the above-listed quantities do not always stay the same. In fact, certain pulsars exhibit more than one drifting patterns, characterised by distinct values for P_2 , P_3 , and D , and the observed emission alternates between these configurations. For such ‘drift mode changing’ pulsars, each subset of quantities (P_2 , P_3 and D) is generally used as a marker to identify the different subpulse drifting modes within a pulsar’s emission. Generally, the time scale of transition between modes is shorter than one pulsar rotation (e.g. [Wang et al., 2007](#)). The duration of individual modes can be anywhere from a few pulses to a few hundred pulses. Another interesting and rare subcategory is ‘bi-drifting’, where the drift direction of subpulses is different in different pulse profile components (e.g. [Champion et al., 2005](#)). Complex phenomena such as bi-drifting and mode changing in pulsars pose some challenges for the current theoretical

models of subpulse drifting. This thesis explores the subpulse drifting and mode-changing phenomenon in two specific pulsars J1822–2256 and J0026–1955, the latter being a new discovery from the MWA (McSweeney et al., 2022).

1.5.2.2 The Carousel Model

Within the first decade of the discovery of the subpulse drifting phenomenon in pulsars, multiple theoretical models were proposed to explain the observed effect (Ruderman & Sutherland, 1975; Sturrock, 1971). One of the popular models at that time successfully accounted for the observed subpulse drifting in pulsars like B0809+74 and B0943+10, which exhibit stable drift rates (e.g., Deshpande & Rankin, 1999; Taylor et al., 1971). In this model, the observations of periodic subpulse modulations suggested the presence of regularly spaced sub-beams that rotate progressively around the magnetic axis of the star (Ruderman, 1972).

The carousel model, introduced by Ruderman & Sutherland (1975), gained attention for its initial success in explaining the subpulse drifting phenomenon. According to this model, the radio wave pattern that ultimately escapes the magnetosphere represents the emission from discrete, localised regions of electrical activity known as ‘sparks’ near the pulsar’s surface. These sparks result from the vacuum discharge at the polar cap, generating electron-positron pairs and subsequent particle avalanches along the magnetic field lines, producing curvature radiation. These sparks move in the azimuthal direction around the magnetic axis due to an $\vec{\mathbf{E}} \times \vec{\mathbf{B}}$ drift, where $\vec{\mathbf{E}}$ and $\vec{\mathbf{B}}$ are the electric and the magnetic field, respectively. The velocity of this azimuthal motion is given by

$$\vec{\mathbf{v}} = \frac{\vec{\mathbf{E}} \times \vec{\mathbf{B}}}{B^2} \quad (1.7)$$

where B is the magnetic field strength. Near the magnetic poles, the strong electric field causes a gap in the charged particle distribution, called the polar gap. Because of the common $\vec{\mathbf{E}} \times \vec{\mathbf{B}}$ drift experienced everywhere in the polar gap, it is reasonable to assume

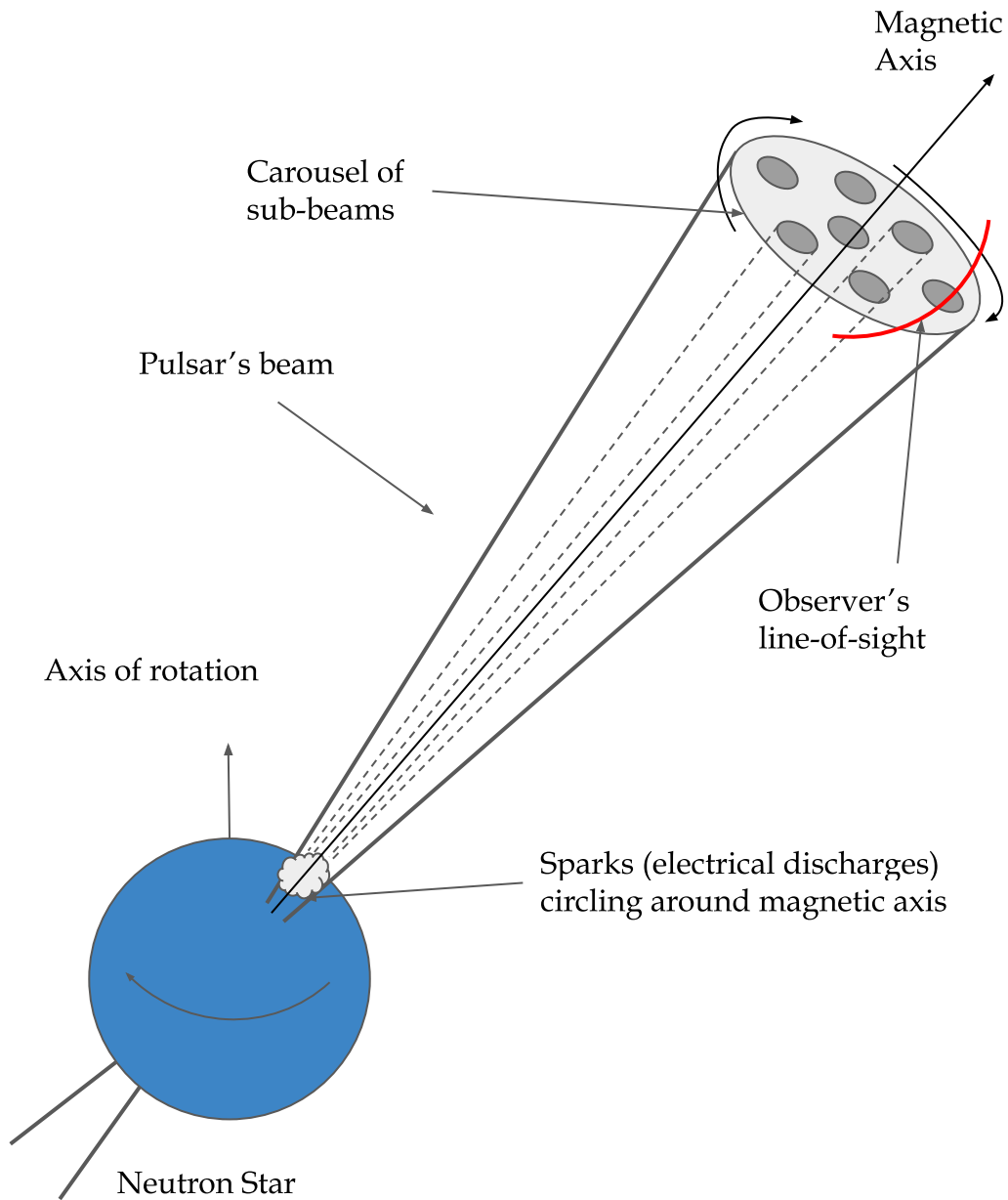


Figure 1.8: A schematic of the carousel model ([Ruderman & Sutherland, 1975](#)) showing sub-beams formed in the pulsar's main beam, around the magnetic axis, due to a carousel of sparks near the pulsar surface. As the pulsar rotates around its magnetic axis, because of the difference between carousel rotation and pulsar rotation, a different configuration of sub-beams is observed every time, which leads to the observed drifting of subpulses.

that the global pattern of sparks is regular and quasi-stable in an arrangement resembling a fairground ‘carousel’. As a result, the geometry of the emission beam directly reflects a configuration of sparks, with the discrete beam associated with an individual spark event called a ‘beamlet’. The location of these sparks on the polar cap determines the geometrical beam pattern corresponding to the instantaneous subpulses within a pulsar’s integrated pulse profile. A schematic of the carousel model is shown in Fig. 1.8.

Considering the carousel model of subpulse drifting, the rotation rate of the carousel with n sparks is defined as P_4 , which is usually different from that of the pulsar period. Thus, for a pulsar with $P_1 \neq P_4$, a different intensity pattern will be observed with each rotation as the observer’s line of sight cuts through a slightly rotated carousel, producing the observed drifting behaviour. In this scenario, P_3 can be interpreted as the measure of time after which a certain spark will return at a particular longitude. Similarly, the quantity P_2 will directly translate to the separation between sparks that cross the observer’s line of sight during a single pulse.

Alternative models have been suggested to interpret the drifting subpulses geometrically. For e.g., [Kazbegi et al. \(1991\)](#) and [Gogoberidze et al. \(2005\)](#) suggest that drift waves in some form of magnetospheric oscillations cause a modulation in the emission region, which are observed as drifting subpulses. According to their model, the subpulses arise from periodic variations in the magnetospheric plasma. [Clemens & Rosen \(2008\)](#) suggest that non-radial oscillations in the emission region itself could be responsible for subpulse drifting without requiring circulations in the magnetosphere. While these models can explain certain phenomena like mode changing, they are unable to satisfactorily account for other phenomena such as bi-drifting.

Furthermore, several pulsars have been found to exhibit more complex subpulse drifting behaviour, which the classical carousel model cannot account for. In particular, phenomena such as bi-drifting, non-drifting core components, drift rate reversal etc., have

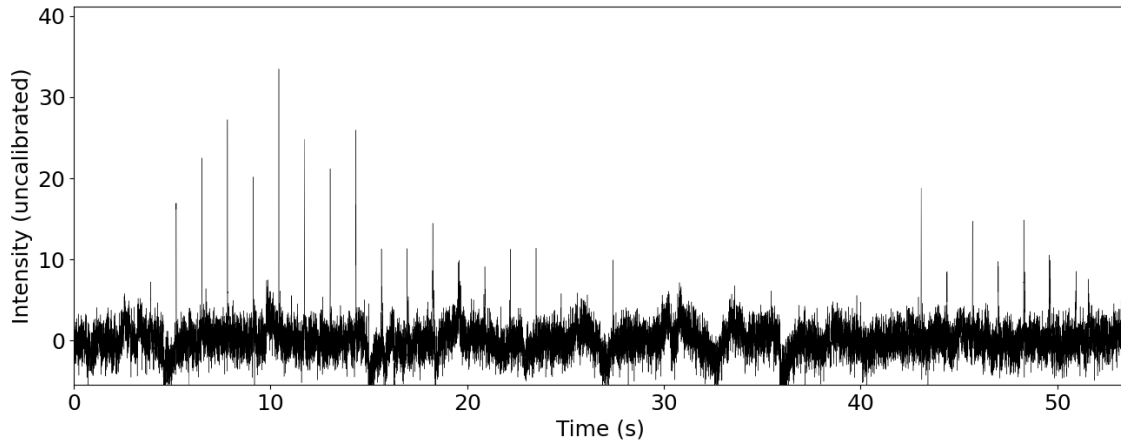


Figure 1.9: Example of nulling shown by PSR J0026–1955 observed at 300-500 MHz, using uGMRT. A few pulses near the beginning and towards the middle of the sequence are missing. The x -axis represents time elapsed (in seconds) since the beginning of the observation.

prompted that modifications are necessary to the original model presented by Ruderman and Sutherland. Ultimately, we still lack a comprehensive theory that can describe many of the observed drifting characteristics. This thesis aims to further explore the phenomenon of subpulse drifting through observational investigations. Importantly, our approach involves using high-quality data and exploiting the capabilities of some of the state-of-the-art radio telescopes, such as the MWA and uGMRT.

1.5.3 Nulling

Another interesting phenomenon in pulsars is ‘nulling’, where the emission ceases abruptly for a few to hundreds of pulse periods ([Backer, 1970a](#)) before it is restored. Oftentimes, nulling is also seen in conjunction with subpulse drifting. An example of sporadic nulling is shown in Fig. 1.9, where a few pulses near the beginning and middle (from ~ 25 - 40 s) of the sequence are missing. The caveat is that any emission that is below the sensitivity threshold of a specific telescope will be treated as a null. Thus, the identification of nulling largely depends upon the sensitivity of a given telescope. However, with the wider

bandwidth and higher sensitivity of next-generation telescopes, it will be possible to search for a low-level emission during the identified nulls. Nulling is seen in about 10% of the known pulsar population, where the onset of a null and the restarting of the emission are both observed to be rapid, i.e., the transition of pulsar emission from an ‘on’ state to an ‘off’ state and vice versa seems to occur within a single pulsar rotation. The fraction of time for which a pulsar is in the ‘off’-state, i.e. a null state, is called the nulling fraction.

The cause of nulling remains largely unexplained. Generally, nulls lasting for one or two pulses are attributed to the stochastic processes within the pulsar magnetosphere (e.g., [Basu et al., 2018a](#)), or a slight variation in the beam such that an empty line-of-sight causes nulls. On the other hand, longer nulls are thought to be related to systematic changes in the plasma processes within the pulsar magnetosphere ([Naidu et al., 2017](#)).

In the case of subpulse drifting pulsars, if nulls and changes in the drift modes are caused by intrinsic changes in the pulsar magnetosphere, then their interactions may prove highly instructive in understanding the underlying physical mechanisms at play in the magnetospheres. The occurrence of nulls is not linked to periodic behaviours such as an eclipsing companion or a precession of the pulsar beam. Thus it is reasonable to consider that nulling is a distinct emission state and that nulling itself may be an extreme form of mode changing, where a pulsar switches between different magnetospheric states ([Gajjar et al., 2014](#)). Interestingly, most theoretical ideas or models tend to focus on the properties of the observed pulsed emission and fall short of fully justifying the lack of emission in the case of the nulls. Hence, the study of pulsars exhibiting both nulling and drifting phenomena is crucial for comprehending the true origin and nature of the nulling phenomenon.

In this thesis, we have discussed pulsars that show both extremes of nulling. For e.g., PSR J1820–0427, which shows no existence of nulling, and PSR J0026–1955, which is seen to null for a large fraction ($\sim 50 - 80\%$) of time. Pulsar nulling is also known to affect

the properties of burst emission before and after its occurrence (e.g., [Lyne & Ashworth, 1983](#)). In this thesis, we also investigate the possible relation between nulling and subpulse drifting modes.

1.6 A Theoretical Outlook

In the previous sections, we have described some of the most important properties of pulsars from an observational and phenomenological point of view. In the following section, we will delve into some aspects of them as physical objects and provide a brief theoretical understanding. Particularly, we explore them as neutron stars, the details of their magnetosphere, and the physical processes that might give rise to electromagnetic radiation.

1.6.1 Neutron stars and Pulsars

The balance between radiation pressure from thermonuclear fusion reactions and gravitational pressure is what holds a main-sequence star together. The outward pressure from fusion can only sustain the inward pressure of gravity until the termination of the thermonuclear reaction at the stellar core. Once the thermonuclear reaction ceases, the gravitational collapse cannot be counteracted, leading to a stellar collapse. For massive stars ($\sim 8 - 20M_{\odot}$), the star collapses due to gravity, triggering a cataclysmic explosion called a “supernova” ([Baade & Zwicky, 1934](#)). During this process, the outer layers of the star are blown away, leaving behind a compact core, mainly composed of heavier elements and atomic nuclei. Theoretically, for massive (parent) stars, if the mass of this nucleus is more than the Chandrasekhar limit ($\sim 1.44M_{\odot}$), it is subject to free fall under intense gravity ([Chandrasekhar, 1931](#)). During this phase, the density of the object is large enough to favour β -decay:



Under this process, the remnant core forms a large number of neutrons,

$$\frac{\text{Chandrasekhar mass}}{\text{Mass of a neutron}} \simeq \frac{1.44M_{\odot}}{1.7 \times 10^{-24}\text{g}} \approx 10^{57} \quad (1.9)$$

thus justifying the name “neutron stars”.

Any further gravitational collapse of neutron stars is counteracted by the neutron degeneracy pressure. Neutron degeneracy is essentially a consequence of the Pauli exclusion principle, which states that no two identical fermions (in this case, neutrons) can occupy the same quantum state simultaneously. As the compact remnant contracts under the pressure of gravity, the energy levels available to the neutrons become limited, forcing them into higher energy levels. The effective pressure resulting from neutron degeneracy counterbalances the gravitational force, preventing further collapse. Though one can imagine that if the remnant is massive enough, it may surpass the neutron degeneracy pressure, thus encouraging further gravitational collapse, resulting in a black hole.

It is important to note that not all neutron stars are pulsars; however, all pulsars are neutron stars. Only the neutron stars that emit beams of radiation from their magnetic poles and whose emission crosses our lines of sight are observed as pulsars. The presence or absence of observable emission from the magnetic poles of a neutron star depends on a number of factors, including, but not limited to, its magnetic field strength, rotational characteristics, and emission mechanisms.

1.6.2 The pulsar magnetosphere

[Goldreich & Julian \(1969\)](#) were the first to prove that an empty pulsar magnetosphere cannot be maintained due to the extreme magnetic fields, thus implying that the magnetosphere cannot be a vacuum and is composed of charged particles. These strong magnetic fields act as a dynamo generating enormous electric fields that extracts elemental particles from the neutron star’s surface, thus forming a ‘plasma-filled magnetosphere’. The charged particles (and the magnetic field lines) are forced to rigidly co-rotate with the star due to

the strong electromagnetic field. However, this co-rotation can only occur up to a certain radial distance ($r_c = cP_1/2\pi$), where the co-rotation velocity $v = \Omega r_c$ (where $\Omega = 2\pi/P_1$) equals the speed of light. This radial distance defines the ‘light cylinder radius’, which divides the magnetosphere into two distinct regions: the ‘closed field lines’ region, with the magnetosphere of high-energy plasma co-rotating with the pulsar, and the ‘open field lines’ region where the magnetic field lines cannot close. It is within the open field lines region of the magnetosphere that the beam or beams of radiation originate. Most popular pulsar emission models assume that the observed radiation is emitted over a cone centred around the magnetic axis. As the pulsar rotates, a pulse is observed if the observer’s line of sight crosses through this cone of emission.

The strong magnetic fields observed in pulsars can be explained by the conservation of magnetic flux from the progenitor star as it transitions into a neutron star. As a rough estimate, for a normal star with polar field (B_{star}) of the order ≈ 100 G and radius $\approx 10^9$ m, the conservation of magnetic flux would yield a remnant (neutron star radius $\approx 10^4$ m) with a magnetic field strength of the order of

$$B_{\text{star}}A_{\text{star}} = B_{\text{NS}}A_{\text{NS}} \quad (1.10)$$

$$B_{\text{NS}} \sim 100 \text{ G} \times \left(\frac{10^9 \text{ m}}{10^4 \text{ m}} \right)^2 \quad (1.11)$$

$$B_{\text{NS}} \sim 10^{12} \text{ G} \quad (1.12)$$

which is the typical value for a canonical pulsar. In general, the pulsar magnetic flux is estimated using its rotation period (P_1) and the slow-down rate (\dot{P}_1). The core assumption here is that the slowing down of the pulsar’s rotation is mainly due to the loss of rotational kinetic energy through dipole radiation. Thus, for a pulsar with an inclination α between its rotation and magnetic axis, the equatorial magnetic field is (e.g., [Lorimer & Kramer, 2004](#); [Ostriker & Gunn, 1969](#)):

$$B \approx 3.2 \times 10^{19} \times \frac{1}{\sin\alpha} \left(\frac{P_1}{s} \dot{P}_1 \right)^{1/2} \quad (1.13)$$

Outside the pulsar, the magnetic field outweighs the gravitational field by a substantial factor and completely dominates all physical processes. For the crab pulsar, the gravitational force is $\sim 10^{12}$ times weaker than the induced electrostatic forces on an electron near the surface.

1.6.3 Emission Mechanism

Even after fifty years since the discovery of radio pulsars, we still lack satisfactory models that can comprehensively explain the physical mechanism responsible for their radio emission (Melrose et al., 2021). However, there is some consensus on some of the general features; for example, it needs to be coherent emission and a mechanism that involves relativistic electrons generated in avalanches, and the emission should originate somewhere along the open field lines that define the polar cap. In the early decades of pulsar research, several ideas were advanced; however, there are observations that argue both in favour and against most of them.

One of the first proposed ideas invoked the generation of emission through the acceleration caused by the large-scale curvature of open magnetic field lines (e.g., Lyubarskii, 1996). This “curvature radiation” is essentially due to the one-dimensional motion of highly relativistic particles along the curved magnetic field lines. Due to the intense magnetic fields within the pulsar magnetosphere, particle (electron or positron) trajectories will be constrained to follow the magnetic field lines. This constrained motion of particles is often referred to as “beads on a string”. Since the field lines are generally curved, the particle experiences a transverse acceleration while in motion. As a result, these particles will emit in the form of ultra-high energy γ -ray photons, which will subsequently undergo pair-production (Sturrock, 1971). The resulting electron-positron pairs are then accelerated to produce more (lower energy) photons, and a particle cascade develops. These cascades create a plasma above the polar cap, from which the radio emission emerges as a beam that aligns tangentially with the open field lines at the emission altitude. This type

of curvature radiation can be considered a special case of synchrotron radiation, where the pitch angle is closer to zero.

Some studies (e.g. [Harding & Preece, 1987](#)) explored the quantisation effects on synchrotron radiation in strong magnetic fields, which is present in the case of pulsars. In the presence of these strong magnetic fields, the momentum and energy of a charged particle are quantised into Landau states (or Landau levels), arising from the interaction between the magnetic field and the particle's motion. The energy spacing of these degenerate levels depends upon the strength of the magnetic field. The discrete Landau levels correspond to particles confined to certain cyclotron orbits, which ultimately affects their emission. For example, let us consider the momentum of charged particles to be quantised into Landau levels. In that case, curvature radiation can be regarded as originating from the lowest Landau level, where the particles have zero momentum orthogonal to the magnetic field, and the entire momentum is in the transversal direction, such that the particles follow the magnetic field lines like "beads on a string". In this picture, synchrotron radiation can be considered a higher Landau level where the particles have a non-zero orthogonal and transversal momentum.

Curvature radiation has faced criticism on both theoretical and observational grounds. The theoretical argument stems from the difficulty of generating coherent emission through curvature radiation, which is essential to account for the observed brightness temperatures (e.g. [Cordes, 1979](#); [Ostriker & Gunn, 1969](#); [Sturrock, 1971](#)). Furthermore, observations of pulsars have revealed numerous instances that deviate from the predictions of the curvature radiation model. For example, the polarisation position angle curves of many pulsars exhibit significant deviations from the expected shape as dictated by the curvature radiation and the dipole field line geometry (e.g., [Mitra et al., 2016](#); [Noutsos et al., 2015](#)). On the other hand, orthogonally polarised modes¹ lack a natural explanation within the

¹For some pulsars, the pulsar polarisation states can switch between two orthogonal modes ([Backer et al., 1976](#)). At some pulse longitudes, the polarisation angle occasionally jumps by 90° while continuing to follow the rotating vector model on the orthogonal track.

context of curvature radiation (e.g. [Gangadhara, 1997](#)). These challenge the validity of the curvature radiation model as the primary mechanism for pulsar emission and as such, call for modifications or extensions to the existing models.

1.7 Motivation and scope of this thesis

The central theme of this thesis is to study ‘organised’² and ‘unorganised’³ single pulse modulation in terms of subpulse drifting and pulse-to-pulse amplitude variability. Single pulse studies provide a wealth of knowledge about pulsar emission, as each pulse is encoded with information about the instantaneous plasma activity in the pulsar magnetosphere. Every pulsar is observationally unique and provides a distinct window for studying pulsar emission. The aim of this thesis is to therefore characterise and understand these modulations and explore them in the context of existing models in an effort to chart the path forward. Our study makes use of multi-frequency high-quality pulsar data at sub-GHz frequencies using the Murchison Widefield Array (MWA) and the upgraded Giant Metrewave Radio Telescope (uGMRT). Exploiting the unprecedented sensitivity and wideband coverage of these state-of-the-art telescopes, in this thesis, we conducted a detailed investigation of single pulse characteristics in these pulsars. The thesis is organised as follows.

1. **Chapter 1** introduces the motivation of this thesis.
2. **Chapter 2** briefly introduces the telescopes used to acquire the data used in this work, along with the software used for preliminary data analysis.
3. The major contributions to this thesis focus on understanding the pulsar emission mechanism by studying three specific pulsars - J1822–2256 (**Chapter 3**), J1820–

²Organised modulations in pulse amplitude and phase are revealed in observations in the form of repeating patterns in pulse sequences (e.g., subpulse drifting).

³The underlying pulsar emission processes may give rise to variations in single pulse amplitude and phase, which can be quite erratic with no specific order, defined as unorganised modulations.

0427 (**Chapter 4**), and J0026–1955 (**Chapter 5**), as briefly summarised below.

4. Finally, **Chapter 6** presents a summary of the main findings emerging from this thesis and a discussion on potential future extensions of this work.

Chapter 3

Subpulse drifting in pulsar radio emission is considered to be one of the most promising phenomena for uncovering the underlying physical processes. In this work, we have presented a detailed study of such a phenomenon in observations of PSR J1822–2256, made using the upgraded Giant Meterwave Radio Telescope (uGMRT). Observations were made simultaneously using the Band 3 (300-500 MHz) and Band 4 (550-750 MHz) receivers of the uGMRT. The pulsar is known to exhibit subpulse drifting, mode changing, and nulling. Our observations reveal four distinct subpulse drifting modes of emission (A, B, C, and D) for this pulsar, with the drift periodicities of $17.9 P_1$, $5.8 P_1$, $8 P_1$, $14.1 P_1$, respectively (where P_1 is the pulsar rotation period), two of which exhibit some new features that were not reported in the previous studies. We also investigate the possible spark configuration, characterised by the number of sparks (n) in the carousel patterns of these four drift modes, and our analysis suggests two representative solutions for the number of sparks for a carousel rotation period, P_4 , which lies in the range of 13 to 16. The large frequency coverage of our data (300-750 MHz) is also leveraged to explore the frequency dependence of single-pulse characteristics of the pulsar emission, particularly the frequency-dependent subpulse behaviour and the emission heights for the observed drift modes. Our analysis suggests a clear modal dependence of inferred emission heights. We discuss the implications for the pulsar emission mechanism and its relation to the proposed spark configuration.

Chapter 4

In this work, we have studied the pulse-to-pulse variability in PSR J1820–0427 and its frequency dependence using high-quality, wide-band observations made from the upgraded Giant Metrewave Radio Telescope (uGMRT; 300-750 MHz) and the Murchison Widefield Array (~170-200 MHz). The low-frequency data reveal a previously unreported feature in the average profile (at 185 MHz) after accounting for the effects of temporal broadening arising from multi-path scattering due to the Interstellar Medium (ISM). We advance a new method for flux density calibration of beamformed data from the uGMRT and use it to measure the single pulse flux densities across the uGMRT band. Combined with previously published measurements, these flux densities are best fit with a power-law spectrum with a low-frequency turnover. We also use calibrated flux densities to explore the relationship between pulse-to-pulse variability and the spectral index of individual pulses. Our analysis reveals a large scatter in the single-pulse spectral indices and a general tendency for brighter pulses to show a steepening of the spectral index. We also examine the frequency-dependence of the pulse-fluence distribution and its relation to the Stochastic Growth Theory.

Chapter 5

PSR J0026–1955 was independently discovered by the Murchison Widefield Array (MWA) recently. The pulsar exhibits subpulse drifting, where the radio emission from a pulsar appears to drift in the spin phase within the main pulse profile, and nulling, where the emission ceases briefly. The pulsar showcases a curious case of drift rate evolution as it exhibits rapid changes between the drift modes and a gradual evolution in the drift rate within a mode. Here we report new analysis and results from observations of J0026–1955 made with the upgraded Giant Meterwave Radio Telescope (uGMRT) at 300-500 MHz. We identify two distinct subpulse drifting modes: A and B, with mode A sub-categorised into A0, A1, and A2, depending upon the drift rate evolutionary behaviour. Additionally,

the pulsar exhibits short and long nulls, with an estimated overall nulling fraction of $\sim 58\%$, which is lower than the previously reported value. Our results also provide evidence of subpulse memory across nulls and a consistent behaviour where mode A2 is often followed by a null. We investigate the drift rate modulations of J0026–1955 and put forward two different models to explain the observed drifting behaviour. We suggest that either a change in polar gap screening or a slow relaxation in the spark configuration could possibly drive the evolution in drift rates. J0026–1955 belongs to a rare subset of pulsars which exhibit subpulse drifting, nulling, mode changing, and drift rate evolution. It is, therefore, an ideal test bed for carousel models and to uncover the intricacies of pulsar emission physics.

Chapter 2

Data Acquisition and Pre-processing

“A straight line may be the shortest distance between two points, but it is by no means the most interesting.”

- The Doctor

This chapter covers high-level overviews of the two major radio astronomy facilities used in this thesis to observe pulsars and some important aspects of data acquisition and analysis. These telescopes are the upgraded Giant Metrewave Radio Telescope and the Murchison Widefield Array, which are described in §2.1 and §2.2, respectively.

The study of pulsars below ~ 1 GHz is aided by their characteristic brightness at lower frequencies. The upgraded Giant Metrewave Radio Telescope (uGMRT) offers simultaneous wide-frequency coverage, enabling high-sensitivity multi-frequency observations of pulsars. On the other hand, the Murchison Widefield Array (MWA) has a unique capability of recording complex voltages for off-line beamforming at frequencies below 300 MHz, which is particularly useful for studying the low-frequency spectrum of pulsar emission.

We summarise the methods and software used to process the pulsar data in §2.3, where the focus is primarily on describing the general methodology, the pre-processing procedures, and the software for the analysis relevant to this thesis. Subsequent chapters



Figure 2.1: Antenna C3 of the uGMRT telescope, alongside a model of the array configuration. The antenna is 45 meters in diameter and is part of the central square. *Image Credit: Parul Janagal*

will present more details on the datasets used in each work.

2.1 The upgraded Giant Metrewave Radio Telescope

The Giant Metrewave Radio Telescope (GMRT) is a state-of-the-art radio interferometer located near Pune, in central western India (Fig. 2.1). In 2019, it was also recognised as a pathfinder telescope for the Square Kilometre Array (SKA). The GMRT consists of 30 parabolic reflector antennas, each with a diameter of 45 meters, arranged in a Y-shape configuration (Swarup et al., 1991). Of the 30 antennas, 12 are placed in a central $1\text{km} \times 1\text{km}$ region to form a compact configuration, while the remaining dishes form an approximate ‘Y’ shape, with 6 dishes located in each of the three arms. The maximum

baseline between the GMRT antennas is ~ 25 km, and the whole array has an effective area of $\sim 30,000$ m², which makes it one of the most powerful among currently operational low-frequency interferometric telescopes in the world. The GMRT is a remarkable feat of modern science and engineering, with its unique mesh design for antennas called SMART, which stands for Stretch Mesh Attached to Rope Trusses. Following a recent upgrade (hence the name upgraded GMRT or uGMRT), the array is currently operational at four discrete radio bands, providing seamless coverage from 120-1600 MHz, with a maximum instantaneous bandwidth of up to 400 MHz (Gupta et al., 2017; Reddy et al., 2017). The large bandwidths of uGMRT mean much higher sensitivity and better spectral and time resolution. For the work discussed in this thesis, we have utilised the array in two specific configurations, as detailed below.

2.1.1 Phased Array

In the phased array (PA) mode, the voltage signals from each antenna are processed through a real-time digital beamformer, which performs a coherent addition of signals from all the antennas working at the time of the observation. Here, the signals from each antenna are appropriately delayed, and phase adjustments are applied so that the synthesised beam can be pointed in the chosen direction (Gupta et al., 2000). The PA mode provides a sensitivity that is \sqrt{N} (N is the number of antennas used for observation) times larger compared to the incoherent addition of detected signals in an Incoherent array (IA).

A common strategy employed for some of our observations is to subdivide the array into two separate “subarrays”. For e.g., the antennas within the central square form one subarray (short baseline), and the antennas located along the arms form a second (more extended baseline) array. These subarrays can be used simultaneously or independently. For e.g., the subarrays can be configured at different frequencies and can be used to observe any source simultaneously at multiple frequency bands. Usually, the shorter baselines in a subarray configuration are used for lower frequencies and longer baselines

for higher frequencies because de-phasing between antennas increases with decreasing observational frequency. For calibration in pulsar observations, a nearby compact radio source is observed periodically, ideally once every hour, to account for the changing ionospheric conditions. At the start of an observing session, observations are also made of a bright pulsar for performing a quick assessment of the goodness of calibration solutions; for this, the incoming pulsar data are synchronously folded to assess the strength of the pulsar signal, which can be taken as a proxy for the goodness of calibration solutions.

2.1.2 Interferometer

As mentioned earlier, the uGMRT is primarily an interferometric array capable of making high-resolution radio images of the sky with a typical angular resolution of $\sim 5\text{-}10''$. In this mode, instead of adding the signals from each of the 30 antennas, signals from pairs of antennas are cross-correlated, giving $^{30}C_2$ combinations to form interferometric baselines. This cross-correlation provides a set of overlapping ‘visibilities’, which contain information about the amplitude and phase of the signal received by each pair. These visibilities can then be Fourier transformed and inverted to reconstruct a two-dimensional image of the radio sky. This technique, called aperture synthesis, provides high angular resolution and sensitivity owing to the large number of baselines. For pulsar science, the interferometer mode is typically used for studying the pulsar environments, source localisation, etc.

2.2 The Murchison Widefield Array

The Murchison Widefield Array (MWA) is a low-frequency (80-300 MHz) aperture array telescope consisting of a large number (4096) of dipole antennas, which are grouped into 256 tiles, where each ‘tile’ is a regular 4×4 grid (Fig. 2.2). These tiles are distributed over a ~ 6 km-diameter region of the Western Australian desert within the Inyarrimanha Ilgari Bundara, the CSIRO Murchison Radio-astronomy Observatory. Each dipole antenna is



Figure 2.2: One of the 256 “tiles” that make up the MWA telescope. Each tile has 16 cross-dipole antennas, which are connected to an analogue beamformer (white box). (Image credit: Dr John Goldsmith/Celestial Visions, 2012)

a simple bow-tie-shaped structure, as shown in Fig. 2.2. When radio waves are incident on these antennas, they induce an electrical current (voltage signals). The signals from each antenna are amplified and digitised before being combined and processed by a digital signal processing system, as described in the following sections.

The original MWA was comprised of 128 tiles, with a maximum baseline of ~ 3 km (Tingay et al., 2013). In 2017, the array was upgraded with the addition of a further 128 tiles and extending the baseline to ~ 6 km (Wayth et al., 2018). This Phase-2 array upgrade included no new digital signal processing equipment (i.e. receiver and the correlator remain the same), nevertheless improving the sensitivity in imaging by almost an order of magnitude (owing to the longer baselines). For the work presented in this

thesis, the MWA observations were made at a central frequency of 185 MHz with a 30.72 MHz wide bandwidth.

2.2.1 The Voltage Capture System

MWA data are recorded using the Voltage Capture System (VCS; Tremblay et al., 2015), which records Nyquist-sampled dual polarisation voltages from each of the 128 tiles (short baseline configuration), and hence an aggregate data rate of 28 TB per hour. The channelised voltages can be processed offline using a suite of software tools which essentially form the subsystems in the high-time resolution processing signal path. The analogue signals from the dipole antennas are first processed through a real-time analogue beamformer, which delays the signal from each dipole by appropriate amounts to form a primary beam pattern (typically $\sim 20^\circ$ across at 185 MHz), for steering the telescope to the targets of interest.

After analogue beamforming, the 256 independent real voltage signals (2 polarisations for each of the 128 tiles) are digitised at a sampling rate of 655.36 MHz. The signals are then channelised using a two-stage polyphase filterbank (PFB). At the first stage, the data are “coarsely” channelised into 256×1.28 MHz channels, from which 24 (user-selected) $\times 1.28$ MHz channels are transported to the central processing facility. The second stage of PFB channelises each of the 24 coarse channels further with a 10 kHz frequency resolution, finally giving a contiguous bandwidth of 30.72 MHz, spread across 3072×10 kHz fine channels, with a native resolution of $100 \mu s$.

2.2.2 Tied-array Beamforming

The MWA has an offline implementation of tied-array beamforming to combine the signals from multiple tiles. Beamforming is a signal-processing technique that can be used to provide a maximum instantaneous sensitivity, which is important for pulsar observations. This is done by calculating the time delays and phase differences between the signals

received by each antenna and applying them before performing a coherent addition. Assuming good calibration solutions, this action combines the signals to maximise the final sensitivity achievable, which is crucial for high-time resolution single pulse studies, such as those performed as part of this thesis.

Unlike other telescopes with dedicated pulsar backends, beamforming of MWA-VCS high-time resolution data is accomplished offline once the data are transported to the Pawsey Supercomputer, where all the post-processing is carried out. Essentially, the channelised voltages recorded from each tile are processed offline using the software tied-array beamformer (Ord et al., 2019) by summing coherently after calibration.

2.3 Data Processing

This section describes the generic software and post-processing routines used in our analysis. The software detailed below are used to handle the output data formats from the telescopes used for this thesis. These software packages convert the telescope data into standard file formats, which can then be used for further analysis through more specific analysis tools and techniques.

2.3.1 PRESTO

PRESTO (Pulsar REsearch and Search TOolkit; Ransom, 2001) is a software package primarily used in searching for accelerated pulsars, i.e., pulsars in a binary system. The PRESTO pipeline involves performing an extensive search for periodic signals that may help indicate the presence of a pulsar. The software first processes the digitised (and channelised) data from the telescope and corrects for the effects of dispersion by performing incoherent dedispersion (as described in §1.4.1). Following the dedispersion, the data are searched for periodic signals using a Fast Fourier Transform (FFT) algorithm. Finally, after a range of checks and scrutiny to confirm the likelihood of being a pulsar candidate, the software also provides a range of tools for further analysis.

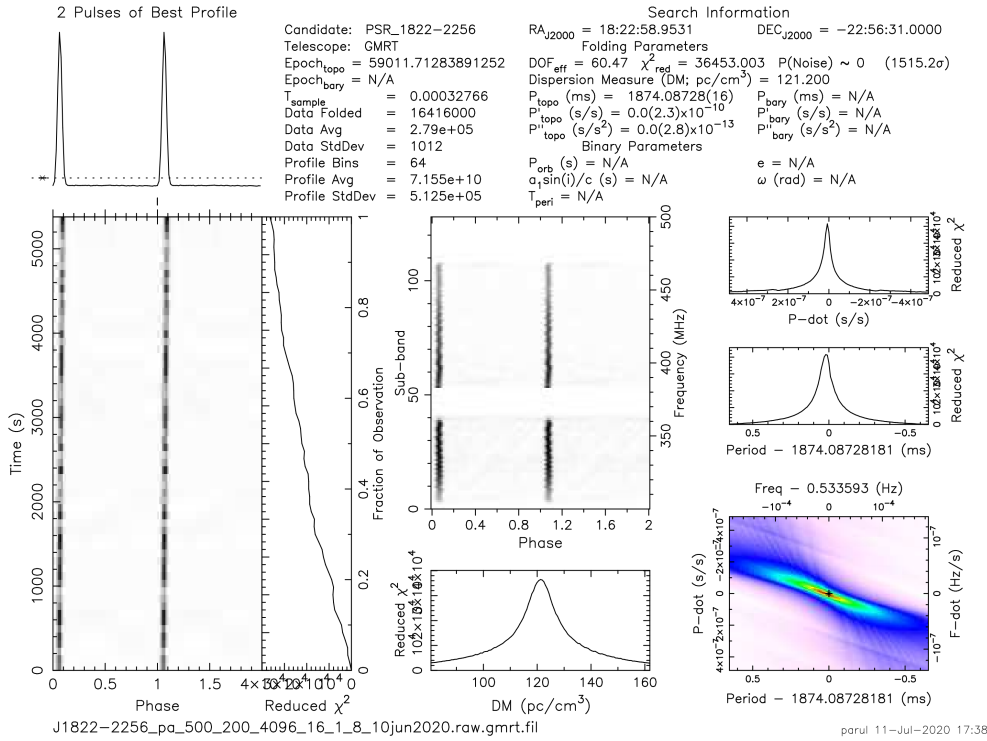


Figure 2.3: A PRESTO diagnostic plot for PSR J1822–2256, observed with Band 3 (300–500 MHz) of uGMRT. The bottom-left panel shows a pulse stack of the observed signal. The average pulsar profile is shown at the top left. The wide-band nature of the pulsar can be seen in the top-middle figure. The peak in the bottom-middle plot shows the DM at which the signal, when de-dispersed, has the largest S/N. The plots on the right show a search over P and \dot{P} .

A typical PRESTO diagnostic plot is shown in Fig. 2.3, which is from one of our observations of PSR J1822–2256 studied for the thesis. The plot shows the temporal persistence of the pulsar signal in the bottom left panel, with the average pulsar profile at the top. The middle panel shows the phase and frequency plot of the time-average signal across the observed frequency range. In all these plots, the pattern is repeated twice for better visual appeal. It is typical to allow PRESTO to search in the DM , P , and \dot{P} parameter space. This is particularly useful if one or more of these parameters is variable or known with only limited precision. Analysing a PRESTO diagnostic plot is one of the basic steps

in pulsar data processing, as part of a sanity check to assess if the pulsar is detected and to obtain its fundamental parameters, such as the topocentric period and DM at the time of observation.

2.3.2 DSPSR

DSPSR (Digital Signal Processing for Pulsar Search and Research; [van Straten & Bailes, 2011](#)) is a software package designed to process and analyse pulsar time series data. It can handle large volumes of data and cater to a wide range of telescope data formats, including those from the uGMRT and the MWA. We primarily used this package to convert the telescope data into PSRCHIVE data format. This step uses the pulsar ephemeris to detect and channelised data into multi-dimensional data cubes called archives. Every single pulse archive file contains information related to the observation frequency, pulse number, pulse phase, polarisation, etc., representing the different dimensions. These archives can then be further processed using the suite of tools that comprise the PSRCHIVE software.

2.3.3 PSRCHIVE

The output from DSPSR is obtained in the form of multiple single-pulse archive files, each containing a single pulse from the observed pulsar. These files can then be combined into a single concatenated archive and used for further processing using multiple routines from PSRCHIVE ([Hotan et al., 2004](#); [van Straten et al., 2012](#)). PSRCHIVE provides a range of tools for handling and analysing pulsar data, including routines for folding and stacking pulsar data and estimating pulsar timing parameters. It contains a suite of applications for visualising pulsar data and producing publication-quality plots of pulsar profiles and other data products.

We used several routines within PSRCHIVE to analyse the single pulse archives obtained from DSPSR and for data visualisation. The `pazi` subroutine of PSRCHIVE

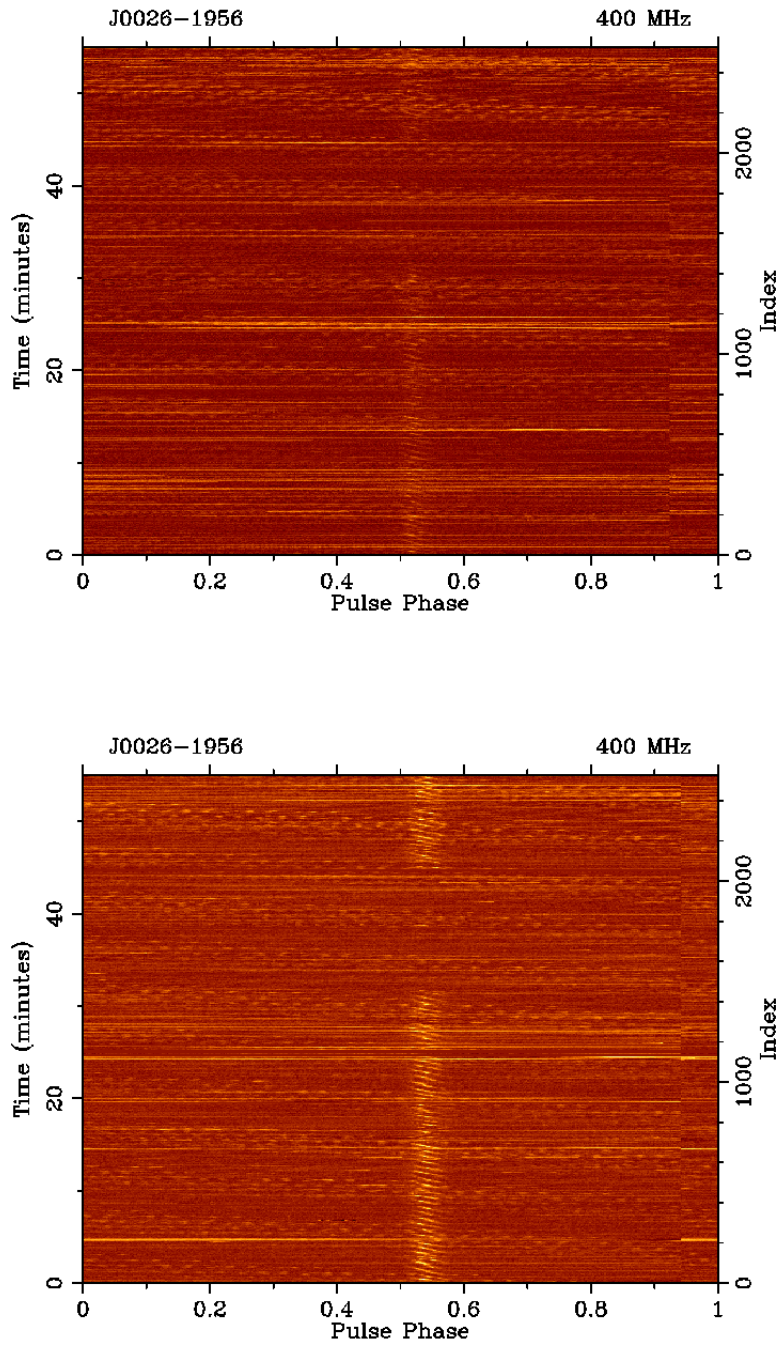


Figure 2.4: *Top:* Pulse stack before using the pazi subroutine for RFI mitigation. *Bottom:* Pulse stack after a few rounds of manual RFI cleaning using the pazi subroutine. The subpulse drifting features and pulsar nulling can be clearly observed in the lower panel.

was especially used for removing RFI (radio frequency interference)¹ instances in both frequency vs phase and time vs phase data. For example, the top panel in Fig. 2.4 shows a pulse stack of single pulse archives of PSR J0026–1955, obtained using DSPSR and plotted using the `pav` sub-routine of PSRCHIVE. In the top panel (before excising RFI), the pulsar is barely visible near phase 0.5. After a few rounds of manual cleaning through `pazi`, a substantial improvement can be seen, as shown in the bottom panel of Fig. 2.4, where the pulsar is clearly visible. Oftentimes, it is a standard practice to excise a small number of frequency channels (typically $\sim 5\%$) near the band edges, where the receiver/backend response is generally lower. It is important to consider a balance between data quality and the amount of data excised during data cleaning. If the data are partially useable, depending upon the science case, they can be retained, even with some residual RFI. However, clear instances of RFI which completely saturate the data points must be removed.

2.3.4 CASA and SPAM

In pulsar work, imaging is typically employed mainly to study the surrounding regions or positional determination (e.g., in the case of newly discovered pulsars). However, simultaneous imaging data, if available, can allow us to calibrate the pulsar time series data. The upgraded GMRT provides this capability, allowing for concurrent imaging and phased array observations. For reducing such imaging data, we have used CASA (Common Astronomy Software Applications; McMullin et al., 2007) and SPAM (Source Peeling and Atmospheric Modeling; Intema, 2014a).

The CASA package is a data processing package used in processing data from both single-dish and aperture-synthesis telescopes. It provides a suite of tools for calibration, imaging, and data analysis from radio telescopes.

¹Non-astronomical signals of terrestrial or instrumental origin that degrade the quality of astronomical data.

SPAM is radio astronomy data processing software developed by [Intema et al. \(2009\)](#) (see also [Intema, 2014b](#)), which is a fully automated software based on the Astronomical Image Processing System (AIPS; [Greisen, 1998](#)). SPAM includes direction-dependent calibration, modelling, analysis, and imaging to correct ionospheric dispersive delays. It uses the ParseITongue interface ([Kettenis et al., 2006](#)) to access AIPS tasks, files, and tables. The software has two main processing steps: a pre-processing step that converts raw data into pre-calibrated visibility data sets and a main pipeline that converts pre-calibrated visibility data into Stokes I continuum images.

In the main pipeline, firstly, the data goes through a direction-dependent (ionospheric) calibration, where the parameters vary with the viewing direction. Next, a model of the sky is created using the calibrated data, which is used to correct for ionospheric delays. After applying the phase calibration, the data are then imaged, and the resulting image is used to create a new sky model. This process of iterating between imaging and sky modelling is called “peeling”, which allows for better correction of ionospheric delays. Once the final sky model is created, the data are imaged, resulting in a high-quality image of the target sky. An example of the final image processed using SPAM is shown in [Fig. 2.5](#).

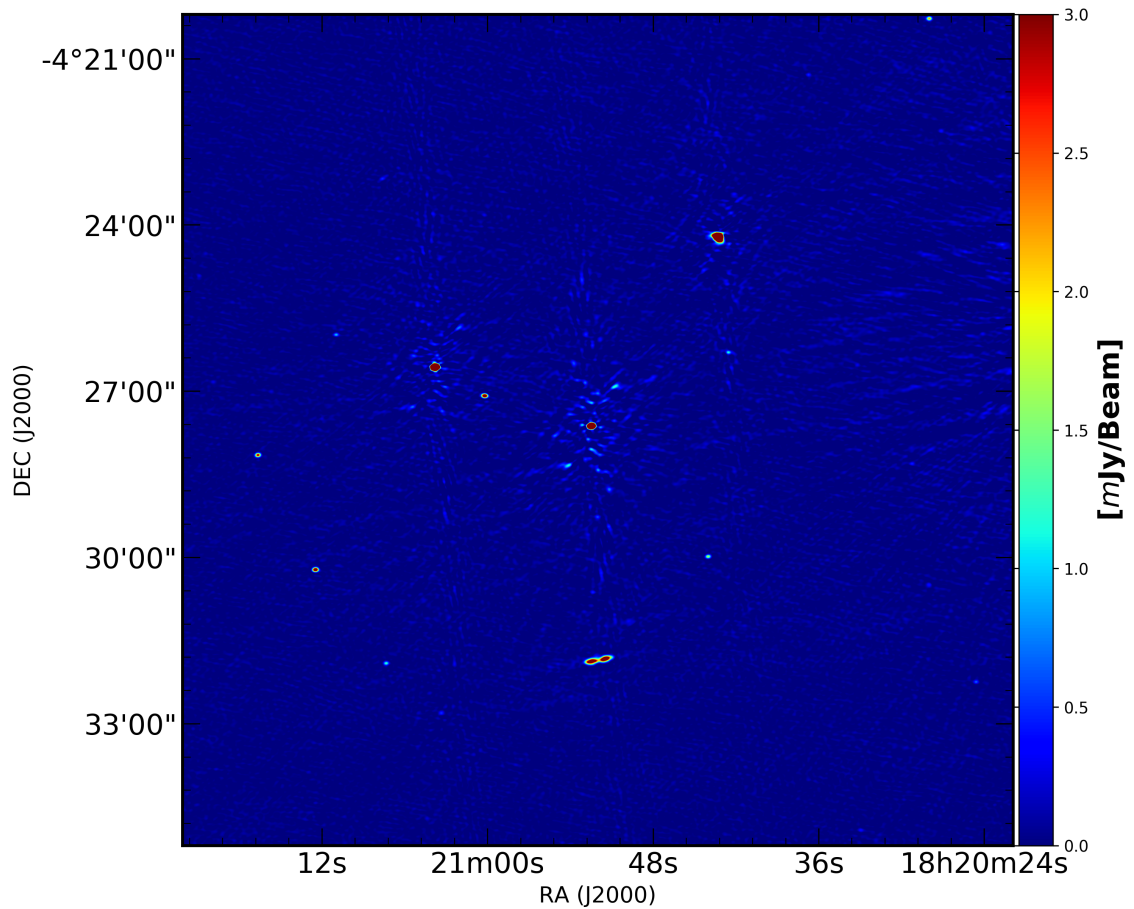


Figure 2.5: A radio image of the sky near PSR J1820–0247 at 550 MHz. The pulsar is at the phase centre of the image. This data was reduced using the SPAM pipeline described in §2.3.4.

Chapter 3

Subpulse drifting in PSR J1822-2256

“There’s always something to look at if you open your eyes!”

- The Doctor

This chapter is a faithful reproduction of *Revisiting the sub-pulse drifting phenomenon in PSR J1822–2256: Drift Modes, Sparks, and Emission Heights* by [Janagal et al. \(2022\)](#).

The discovery of pulsars ([Hewish et al., 1968](#)) is considered to be one of the significant findings in astronomy in the last century. Pulsars are rapidly rotating (spin periods from \sim ms to s), highly magnetized ($\sim 10^8 - 10^{12}$ G) neutron stars ([Gold, 1969](#); [Hewish et al., 1968](#)) that have proved to be enormously insightful to study physics in extreme environments. Even after more than half a century since the discovery of pulsars, their emission mechanism and even the distribution of the emission regions in the magnetosphere are poorly understood. Several observed pulsar phenomena, such as nulling, mode changing, subpulse drifting, etc., directly probe the emission from these compact objects. Studying these phenomena can potentially provide vital clues for uncovering the physical processes that govern how pulsars work.

At the level of individual pulses, pulsar emission typically consists of one or more distinct components known as subpulses. [Drake & Craft \(1968\)](#) were the first to observe the

phenomenon of drifting subpulses, whereby individual subpulses appear to drift in pulse longitude within the on-pulse region with time. As a result, the subpulses are observed to shift in phase systematically within the average pulse window between successive pulses. Several early studies delineated these pulse-to-pulse variations as a characteristic property of pulsar emission (Backer, 1973; Taylor & Huguenin, 1971). When these individual pulses are stacked vertically to form a two-dimensional (2D) pulse stack, the subpulses tend to follow a systematic shift within the on-pulse region visually. This systematic shift resembles a set of discrete diagonally oriented bright regions called *drift bands*. The drift bands may undergo amplitude and phase modulation with time, thereby changing the subpulse intensity or the phase at which it occurs.

The observations of a periodic subpulse modulation suggested the presence of regularly spaced sub-beams that rotate progressively around the magnetic axis of the star (Ruderman, 1972). Subsequently, a detailed explanation was presented in terms of the polar gap theory of Ruderman & Sutherland (1975). This theory suggested that the pattern of radio waves that ultimately escape the magnetosphere is the emission signature of a set of discrete, localised pockets of quasi-stable electrical activity called *sparks* that exist very close to the pulsar surface. The sparks are the sites where the vacuum at the polar cap discharges into electron-positron pairs, which leads to an avalanche of particles streaming through the magnetic field lines and producing curvature radiation. These sparks move about the magnetic axis due to an $\mathbf{E} \times \mathbf{B}$ drift in an arrangement resembling a fairground "carousel". As a result, the geometry of the emission beam directly reflects a configuration of sparks, with the discrete beam associated with an individual spark event called a "beamlet". The location of these sparks on the polar cap determines the geometrical pattern of the instantaneous subpulses within a pulsar's integrated pulse profile. The carousel rotation rate, P_4 , is usually different from that of the pulsar period. Such a model results in observing a different intensity pattern with each rotation as the observer's line of sight cuts through a slightly rotated carousel, producing the observed drifting behaviour.

The vertical separation between driftbands at a given longitude is P_3 , which is measured in units of P_1 , the pulsar rotation period. Therefore, P_3 is a measure of time after which a spark will return at a particular longitude. The horizontal distance between any two subpulses within a given pulse is measured as P_2 in units of longitude. This quantity directly translates to the separation between sparks that cross the observer's line of sight.

While theorists have investigated the phenomenon of subpulse drifting for years, there are still multiple questions that are yet to be answered. Even though the carousel model has been scrutinised thoroughly over the years, there are some outstanding issues with the quantitative predictions of this theory. For instance, the carousel model relies on the curvature radiation mechanism for explaining the coherent radiation, which is difficult to justify from our current knowledge of plasma physics (Melrose, 2017). It is also not clear to what extent the rotation frequency of the star aliases the observed drift rates. The model may require modifications or extensions to explain the observed phenomena like drift mode switching (Huguenin et al., 1970), nulling (Backer, 1970b), bi-drifting (Qiao et al., 2004), etc. In essence, subpulse drifting is a vital phenomenon in understanding the physics behind the radio emission mechanism in pulsars (Rankin, 1986) and is known to be prevalent among a substantial fraction ($\sim 50\%$) of known pulsars (Weltevrede et al., 2007).

Though there has been significant progress in the last 50 years towards understanding the pulsar emission process, the complex nature of pulsar emission, the exact location of emission, distribution of pulse emitting region, etc., remains poorly understood. The advent of wideband instruments and faster processing techniques brings new opportunities for further detailed investigation of the subpulse drifting phenomenon. The increased sensitivity of radio telescopes provides a unique opportunity for in-depth observations of the single pulse behaviour of pulsars with much finer time and frequency resolution.

Even though the observational investigation of pulsar emission phenomenology has

been an active area of research for the past several decades, many questions remain open. In this study, we used the upgraded Giant Meterwave Radio Telescope (uGMRT) in a dual-band phased array mode to simultaneously cover the frequency range of 300-750 MHz to study the single pulse behaviour of PSR J1822–2256 (B1819-22). The focus of this paper is a single pulses study of J1822–2256, which is a relatively less studied, bright, long period ($P_1 = 1.874$ s) pulsar with a dispersion measure (DM) of 121.2 pc cm^{-3} . As with several other pulsars, J1822–2256 is known to switch between a few different emission modes over the timescale of a single pulsar rotation (e.g., [Redman et al., 2005](#), [McSweeney et al., 2017](#)), changing the longitude positions of subpulses from one pulse to another. PSR J1822–2256 shows distinct drift modes, often characterised by an abrupt change in the drift rate along with amplitude modulation. The subpulse drifting properties of this pulsar have been previously investigated by [Basu & Mitra \(2018\)](#); [Joshi et al. \(2018\)](#); [Naidu et al. \(2017\)](#); [Serylak et al. \(2009\)](#); [Weltevrede et al. \(2006, 2007\)](#). The mode changing varies the value of P_3 over different modes of emission, implying a change in either the rotation speed of the carousel or in the distribution or number of sparks. Previous studies ([Basu & Mitra, 2018](#); [Serylak et al., 2009](#); [Weltevrede et al., 2006](#)) have reported the existence of multiple drifting modes, including two modes, corresponding to P_3 values of $16 P_1$ and $6 P_1$ respectively, and a non-drifting mode. In addition, [Basu & Mitra \(2018\)](#) also found a transitional mode at $14 P_1$, that the pulsar sometimes exhibits before entering in mode A. [Joshi et al. \(2018\)](#) have found three modes of drifting corresponding to P_3 values of $17 P_1$, $7.5 P_1$, and $5 P_1$. This pulsar also has a wide profile with about an 8% duty cycle, and thus, the line-of-sight of earth-based observer samples a large section of the polar cap.

Another intriguing phenomenon is pulse nulling, whereby no detectable emission is seen above the telescope’s sensitivity threshold for some time, after which the pulsar emission reappears suddenly to its normal state. The definition of nulling clearly depends upon the sensitivity of the telescope. With the wider bandwidth and higher sensitivity of our data, it is possible to search for a low-level (and persistent) emission during the

nulls. To date, nulling (Gajjar et al., 2012; Wang et al., 2007) has been observed in a large number of pulsars. The pulsar J1822–2256 is also studied to null with a nulling fraction of $\sim 10\pm 2\%$ (Basu & Mitra, 2018; Joshi et al., 2018; Naidu et al., 2017).

In this paper, we present a detailed investigation of single-pulse properties of PSR J1822–2256 at 300–750 MHz using the uGMRT. The remainder of the paper is organised as follows. The observations and data processing are summarised in section 3.1 and 3.2.1. In section 3.2.2, we revisited the subpulse drifting modes for this pulsar in light of the high-sensitivity multi-frequency data. Other characteristics, including brief analysis of P_2 , P_3 , and nulling, are described in section 3.2.3 to 3.2.5. Section 3.2.6 describes to the frequency evolution of the subpulse behaviour. A discussion based on the results of our study is presented in section 3.3, including the relationship between different modes and the carousel geometry. Finally, our conclusions are presented in section 3.4.

3.1 Observations

The Giant Metrewave Radio Telescope (GMRT) is a radio interferometric array with 30 antennas, each of 45-meter diameter, configured in a Y shape over an area of 28 km² (Swarup et al., 1991). In a recent upgrade, the system was equipped with wide-band receivers and digital instrumentation to provide a near-seamless coverage in frequency from 120 MHz to 1600 MHz (Gupta et al., 2017; Reddy et al., 2017), and is now called the upgraded GMRT or uGMRT. We used the phased array mode of the uGMRT, where the incoming signals from all antennas are coherently combined for maximum sensitivity for pulsar observations. For our observations, we used 13 antennas for Band 3 (300–500 MHz) and the same number for Band 4 (550–750 MHz), where we recorded the total intensity data. Observations were made at two epochs, separated by ~ 10 days, simultaneously at both frequency bands. At Epoch 1, we recorded 1.5 hours of data, containing ~ 2900 pulses. Epoch 2 was ~ 53 minutes long and recorded ~ 1700 pulses. The observation details are summarised in Table 3.1.

Table 3.1: Details of observation of J1822-225 using uGMRT

	Band 3		Band 4	
	Epoch - 1	Epoch - 2	Epoch - 1	Epoch - 2
Obs. Length (s)	5400	2880	5400	2880
MJD	59010	59020	59010	59020
Singlepulse S/N	33.29	8.62	2.99	2.82
Freq. Res. (kHz)	48.828	48.828	48.828	48.828
Time Res. (μ s)	836.82	836.82	373.29	373.29
No. of Antennas	13	13	13	13
No. of Pulses	2879	1704	2879	1704

The data were recorded with a time resolution of 327.68μ s, and a frequency resolution of 48 kHz, i.e., 4096 frequency channels over the 200 MHz observing band. Given the pulsar DM of 121.2 pc cm^{-3} for this pulsar, the dispersive smearing is 116μ s across each channel at the highest observation frequency (750 MHz) and 1.82 ms at the lowest (300 MHz) observation frequency. These numbers imply an effective resolution of 116μ s and 1.82 ms at the highest and lowest frequency channel, respectively.

The data were integrated to 1.826 ms, with 1024 bins across the pulsar period. The resulting data were written in the filterbank format and subsequently converted to single pulse archives by processing using the DSPSR package ([van Straten & Bailes, 2011](#)). The single pulse files were then frequency scrunched and combined using the routines from PSRCHIVE ([Hotan et al., 2004](#)). Finally, the frequency scrunched single pulse sequence file was manually searched for radio frequency interference (RFI) using the interactive RFI zapping subroutine `pazi` of PSRCHIVE. The RFI-excised file was then converted into an ASCII format that contained the pulse time series and was used for all subsequent analyses.

Table 3.2: Drift mode measurements of J1822–2256

Mode	Average Burst Length	Mean P3 (P1)	$\sigma_{P_3}^a$	O^b (%)
A	83	17.92 ± 0.02	2.0	46
B	10	5.84 ± 0.16	3.6	19
C	15	7.97 ± 0.15	2.5	17
D	22	14.09 ± 0.02	0.9	6
Pseudo Null	2	-	-	5
Real Null	8	-	-	5
Unknown ^c	10	-	-	2

^a Standard deviation of P_3 in each mode

^b % of the occurrence of the particular drift mode

^c Unknown: pulses that could not be classified in one of the four modes of emission.

3.2 Analysis

The wide bandwidth capability of the uGMRT provides greater sensitivity for single pulse studies. The improvement enables approximately $6 \times$ increase in the usable bandwidth and, thence, a sensitivity boost by over a factor of two for any single pulse work. The simultaneous multi-frequency observations allowed us to study the subpulse drifting, mode changing, and nulling phenomenon over an extended (and nearly continuous) frequency range from 300 to 750 MHz.

The single pulse sequence reveals the presence of multiple emission modes with distinct characteristics. Examples of two-dimensional (2D) pulse stacks are shown in Fig. 3.1. Here, the x -axis represents the pulse phase, where the pulse longitude range 0 - 360° corresponds to the phase range $0 - 1$. The four panels represent the four distinct drift modes (A, B, C, and D) that we observed for this pulsar. Each of the sub-pulse drifting modes is further described in Section 3.2.2. The high-sensitivity single-pulse observations allowed us to identify the emission modes visually. Furthermore, the pulsar also exhibits significant variation in its drifting behaviour, modulating the intensity and the apparent position of the subpulses. The following sections describe the analysis performed to study the sub-pulse drifting behaviour of the pulsar.

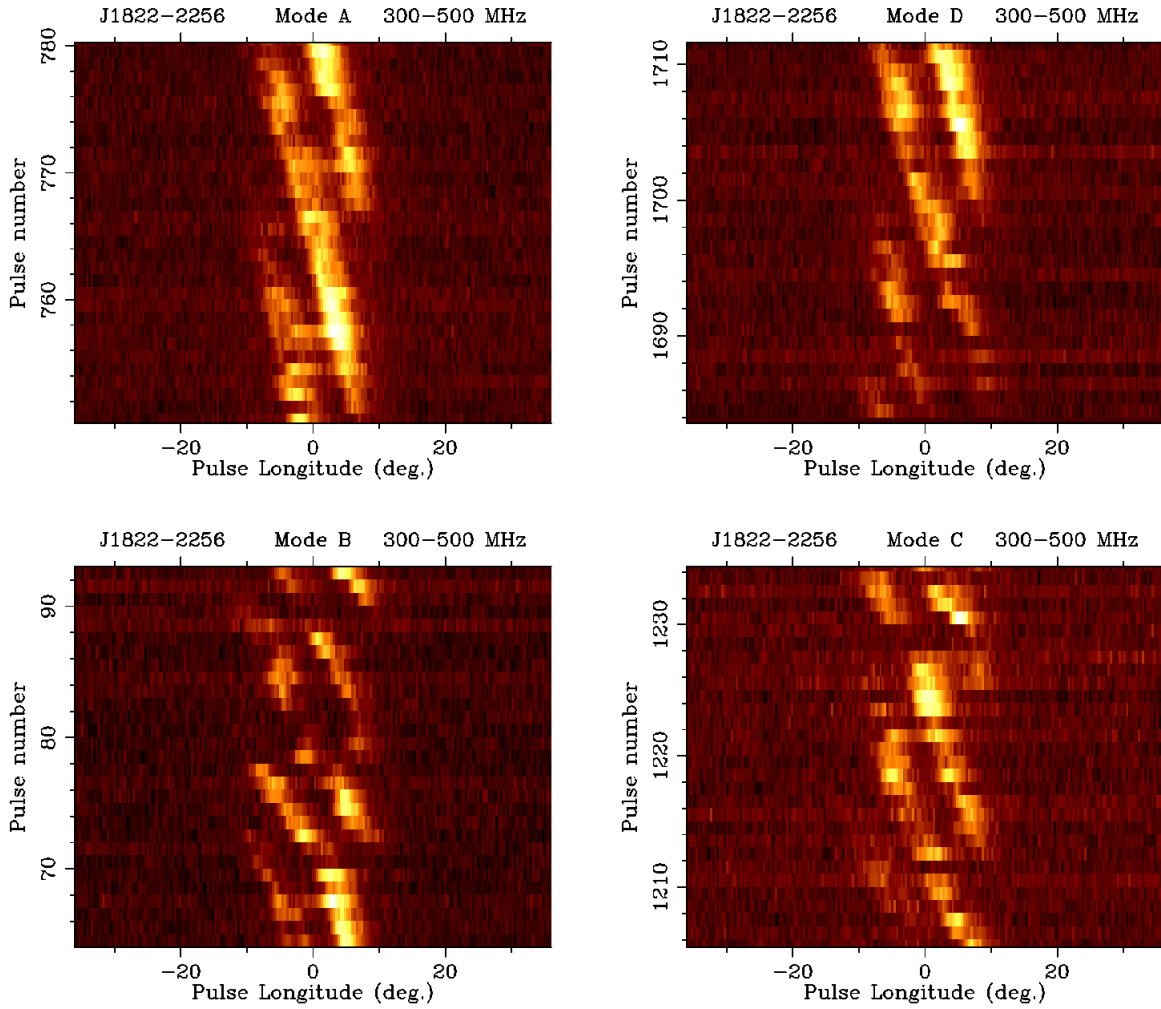


Figure 3.1: 2D-pulsestacks displaying the subpulse drifting modes of emission observed for J1822-2256. The modes A, B, C, and D are arranged anti-clockwise. Here, the x -axis shows the pulse phase, whereas the y -axis is the pulse number. The figure clearly shows drift patterns and their distinct behaviour, representing the four different drift modes.

3.2.1 Mode change boundaries and characterising P_3 values

To determine the mode change boundaries, we employed the Phase Averaged Power Spectrum (PAPS) method described in [Smits et al. \(2005\)](#). We first visually selected a trial sequence of pulses that roughly belonged to one kind of specific drifting sequence. For each of these pulse sequences, we obtained the distribution of intensity values across

the pulse number at a fixed phase. We then performed a Fourier transform of the intensity distribution at each phase to obtain the power spectrum for each phase bin within the on-pulse region. Finally, all the power spectra were averaged over phase, giving a PAPS from 0 to 0.5 cycles per period.

An example is given in Fig. 3.2, showing the PAPS for a pulse sequence corresponding to mode A. Whenever a peak was found in the PAPS, the beginning and end of the pulse sequence were adjusted to get the highest signal-to-noise ratio (S/N) for the peak. The S/N of the peak was calculated by dividing the peak value of the PAPS by the root mean square value of the rest of the PAPS. The start and end pulse numbers of the sequence were then visually inspected to check their coherence with the values calculated from PAPS. We used the reciprocal of the frequency of the centre of the peak in the PAPS to calculate the P_3 value for the respective drift sequence. The resulting P_3 values of each sequence for Epoch 1 and Epoch 2 data are shown in Fig. 3.3. The frequency resolution, given by the inverse of the number of pulses in the sequence, was taken as the error on the peak position.

3.2.2 Modes of Emission

Previous studies of PSR J1822–2256 have revealed multiple distinct modes of emission. Our analysis suggests the presence of four subpulse drifting modes, including some new features that were not reported earlier. We used the P_3 value as well as the average drift profile as the primary criteria for identifying these modes. A summary of the drift mode statistics is given in Table 3.2. Fig. 3.4 shows the average profile of all the categorised modes at both the observed frequency bands along with the full pulsar profile in each band. The centred on-pulse window lies roughly in the pulse longitude range $-20^\circ \lesssim \phi \lesssim +12^\circ$ for Band 3 (300-500 MHz) and $-15^\circ \lesssim \phi \lesssim +10^\circ$ for Band 4 (550-750 MHz), where the longitude $\phi = 0^\circ$ is the centre of the profile where the maximum average flux density is maximum.

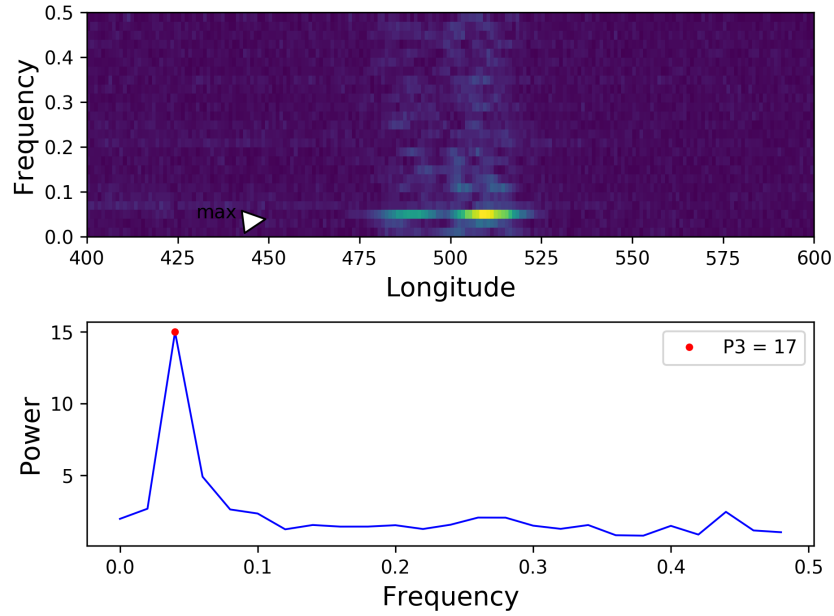


Figure 3.2: LRFS and PAPS for the mode A pulse sequence shown in Fig. 3.1. The top panel shows the Longitude Resolved Fluctuation Spectra (LRFS) of the sequence. The bottom panel shows the phase/longitude averaged value of the LRFS, i.e. PAPS. The maximum intensity mark on the top panel corresponds to the peak in the bottom panel. The inverse of this peak frequency position is P_3 .

3.2.2.1 Mode A

Mode A shows prominent drift bands with a characteristic drifting behaviour (Fig. 3.1) with a mean P_3 value of $17.9 P_1$. The P_3 values of different occurrences show a spread of $\sim 2 P_1$ from the mean P_3 . This mode was previously reported in the literature (Basu & Mitra, 2018; Joshi et al., 2018; Weltevrede et al., 2007). Our observations suggest an occurrence fraction of 46%. The average profiles for mode A at Band 3 and Band 4 are shown in Fig. 3.4, and can be compared to the integrated profile of other modes.

3.2.2.2 Mode B

The pulsar frequently transitions to mode B, which is present for approximately 19% of the time during our observations. This is likely to be similar to mode B as mentioned in

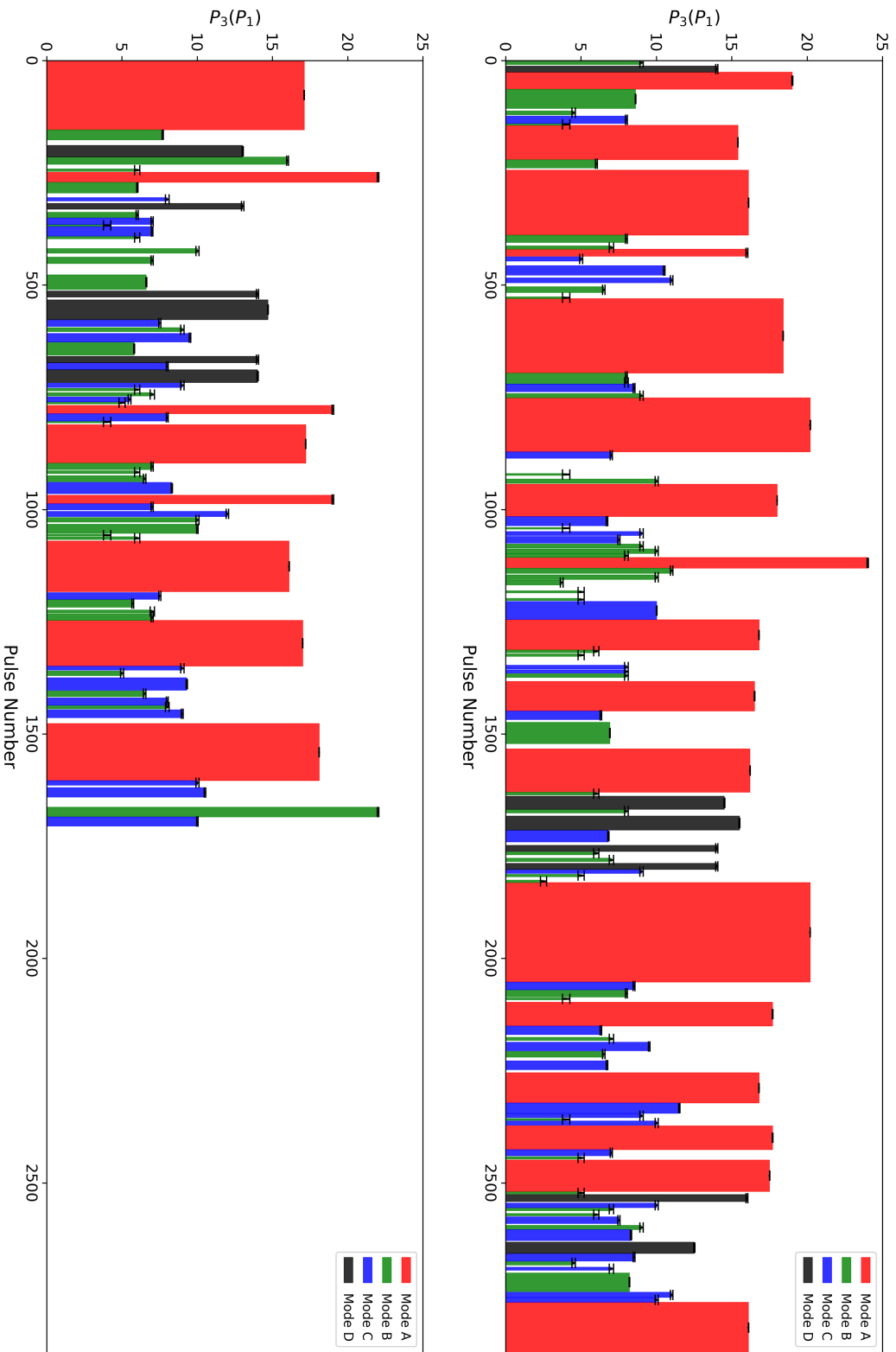


Figure 3.3: A plot of P_3 values for Epoch 1 (top) and Epoch 2 (bottom) of J1822-2256 as calculated using the Phase Averaged Power Spectrum (PAPS). The x-axis shows the pulse number, and the y-axis shows P_3 in units of P_1 . A single block represents a continuous stretch of pulses showing one kind of subpulse drifting mode. The error bars are defined as the inverse of the number of pulses in the respective sequence.

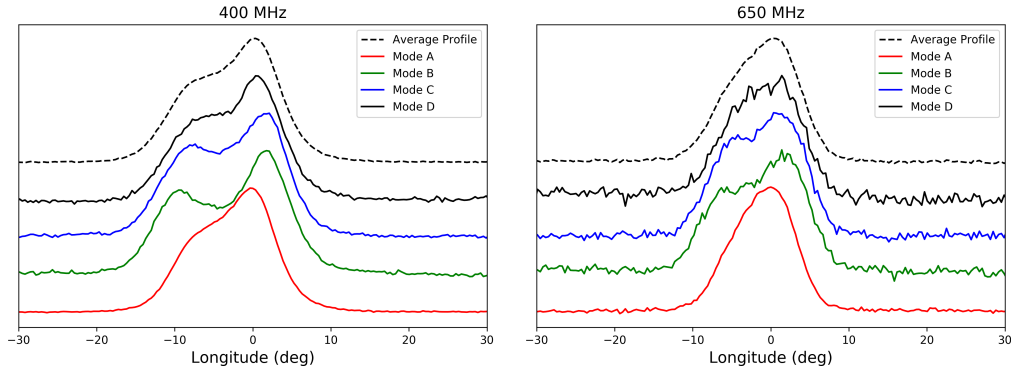


Figure 3.4: Average profiles of different modes of emission of J1822–2256 at Band 3 (300-500 MHz) and Band 4 (550-750 MHz). The black dashed lines show the average profile, and the rest show the colour-coded average profile for each mode. The profiles are given arbitrary constant shifts along the y-axis for display purposes. Apart from the variation of the profiles across the different modes, the frequency-dependent behaviour of the profiles in each mode can also be observed here.

Basu & Mitra (2018); however, their study showed this mode to be a non-drifting mode. Our analysis shows mode B drifting with a mean P_3 value of $5.8 P_1$. Joshi et al. (2018) find a similar mode with P_3 of $5 P_1$ which they refer to as mode C. The P_3 values of different occurrences of this mode show a wide spread of $\sim 3.6 P_1$ from the mean P_3 . In our case, mode B occurs in short bursts, with frequent nulls (Fig. 3.1). We categorised all pulse sequences as mode B, where the drift modes had discontinuities in the drift bands or where the mode length was less than ten pulses. In these cases, a full drift mode is not observed; however, partial drift bands are visible with the characteristic drift rate of mode B. The average profile for mode B (Fig. 3.4) shows a double-peaked structure with widely separated components due to the broken features.

In some cases in the pulse train, the driftbands had a few instances that are marked by an apparent lack of emission in either the middle or the latter half of the drift sequence, leaving the rest of the sequence relatively intact, whereas, in other cases, the drift sequences exhibited a greater suppression of the intensity, such that it becomes relatively difficult

to discern a drift band, even though the drifting feature itself is present (Fig. 3.1). The modes of the latter type were classified as mode B.

3.2.2.3 Mode C

We measure a slightly different mean P_3 for this mode; however, it could possibly be the same as the mode C mentioned in Basu & Mitra (2018), as the values are consistent within the error bars. Joshi et al. (2018) also mention a drifting mode at $7.5 P_1$ which they call mode B. In our case, mode C shows a mean P_3 of $\sim 8 P_1$ with different occurrences showing a spread of $\sim 2.5 P_1$ from the mean P_3 . In mode C, the drift sequences showed an occasional lack of detectable emission in the drift band (Fig. 3.1). In all such cases, the lack of emission is typically seen in the centre or the top part of the drift sequence. Unlike mode B, it is easier to discern and construct a well-connected drift band for mode C, even if a detectable emission was absent for some pulses. It is also possible that modes B and C are related, and the drift bands become irregular as they go to lower P_3 values. The corresponding average profile for mode C (Fig. 3.4) shows two components, similar to that of mode B, but with much more closely separated profile components and a smaller profile width.

3.2.2.4 Mode D

We observed another mode – mode D – which is present only for about 6% of the observing duration. This mode has no visible breaks in the drift sequence. However, it shows occasional intensity variations over the drift band, usually brighter in the leading part of the profile (Fig. 3.1). It displays a characteristic drifting nature similar to mode A, but a mean P_3 value of $\sim 14 P_1$ and a different average profile (Fig. 3.4). The P_3 values of different occurrences of this mode show a spread of $\sim 1 P_1$ from the mean P_3 . Basu & Mitra (2018) found a transitional mode at a similar P_3 value, which occurred mostly when the pulsar was transitioning from mode A to any other mode. However, we choose to call

this type of pulse sequence mode D because of the characteristic difference between the two modes, i.e., most of the occurrences of mode D for our case were preceded by a null. Out of the 13 occurrences of mode D in our observations, only two were found to follow immediately after another mode, namely mode B or C. [Joshi et al. \(2018\)](#) do not report any mode occurring at this P_3 .

3.2.3 P_3 distribution

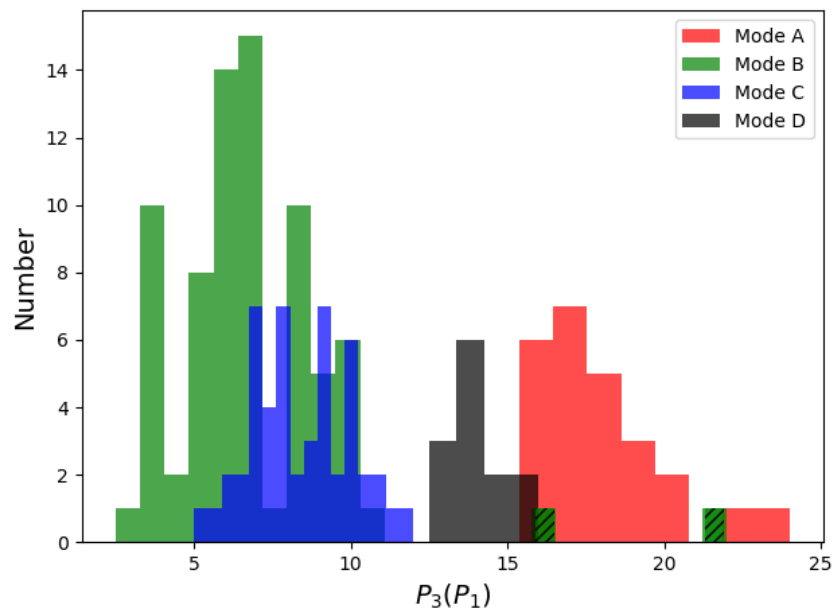


Figure 3.5: Plot of the distribution of the P_3 values for J1822–2256 as calculated by PAPS. The different modes are displayed with different colours. The green-dashed data are part of mode B but are due to sequences which were affected by RFI and also showed an apparent lack of emission within the drift band.

Fig. 3.5 shows the distribution of P_3 values for the full observations, where colour-coded values represent different drift modes. The P_3 values span a large range of values, with mode B showing the smallest value, in which fewer pulses show multiple short-duration bursts. Mode A exhibits the largest values for P_3 with fewer longer duration bursts and a larger occurrence fraction. The two mode B occurrences at $P_3 \sim 16$ and 22

P_1 (Fig. 3.5, shown in green-dashed) are due to sequences that were affected with RFI and also showed no detectable emission within the drift band at times. Since these show the typical characteristics of mode B, i.e., an apparent lack of emission in some parts of the drift band and a wide average profile, the two occurrences were included in mode B. We also searched for the possibility of a correlation between the mode lengths and the P_3 values for each mode. However, our analysis showed no such significant correlation.

3.2.4 Nulling behaviour of J1822–2256

Individual pulses tend to vary in intensity on a variety of timescales, and this is attributed to intrinsic emission processes. A notable phenomenon is pulse nulling, whereby there is no detectable emission above the sensitivity limit of a given observation. In our analysis, we found two different kinds of nulls for J1822–2256. Each of the single pulses was visually inspected to check for any emission feature within the on-pulse longitude ranges. Pulses that did not show a detectable emission feature in the on-pulse region were categorised as null. The pulsar shows regular broadband nulls for about 5% of the total observing time, with an average null length of eight pulses. The averaged profile constructed from these nulls shows a noise-like behaviour at both the observing frequencies.

The null occurrences which were less than or equal to two pulses in length were separately combined to form an average profile. This profile shows discernible low-level emission in both the observing bands, as shown in Fig. 3.6. Pulses of this kind amount to 4% of the observing duration, and we refer to them as *pseudo nulls*. On a single pulse level, these *pseudo nulls* show precisely the same behaviour as the real nulls. These pseudo nulls mostly occur around modes B and C and occasionally before transitioning to a different mode.

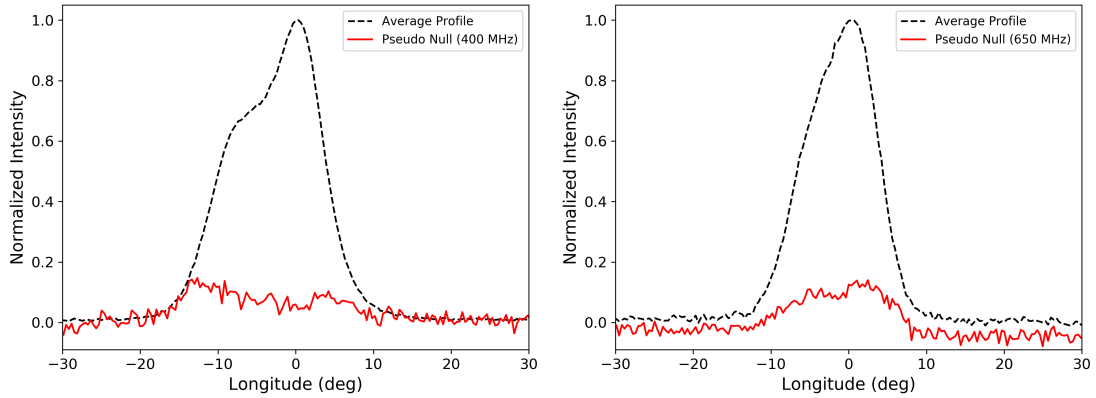


Figure 3.6: Profile of pseudo nulls vs full pulse profile for Band 3 (left) and Band 4 (right).

3.2.5 Characterising P_2

We also calculated the separation between two successive subpulses within a single pulse, which is the periodicity P_2 . Abrupt changes in the number or position of the sparks may lead to a varying value of P_2 . For calculating this parameter, we used the Two-Dimensional Fluctuation Spectra (2DFS; [Edwards & Stappers, 2003](#)) method. For each set of pulses within a given mode, we first performed an FFT at each longitude/phase of the 2D-pulse stack and then performed an FFT for each pulse in the pulse train. This exercise gave two peaks in the resulting 2-dimensional transform. One corresponds to the periodicity in the vertical direction, i.e., for each phase (P_3), and another peak corresponds to the periodicity within each pulse (P_2). The average P_2 at Band 3 was calculated to be $12.8^\circ \pm 0.7^\circ$ and $13.4^\circ \pm 1.4^\circ$ at Band 4 over all modes. Given the small frequency gap between the two bands and the width of the individual bands themselves, the P_2 values are consistent within errors.

3.2.6 Investigation of the frequency dependence of profile components

The wide-band nature of our data provides us with the advantage over previous studies, as it also allows studying the frequency evolution of the subpulse drifting phenomenon.

A frequency evolution of modal profiles is clearly seen in our observations (Fig. 3.4), whereby the average profile changes with an increase in frequency. The characteristic double-peaked structure becomes less separated at a higher frequency for each mode, and the profile becomes narrower.

Using the advantage of the large bandwidth provided by the uGMRT, we can also divide the observation bandwidth into smaller chunks (i.e., sub-bands). We split the observations into 100 MHz bandwidths centred at four central frequencies of 350 MHz, 450 MHz, 600 MHz, and 700 MHz. This exercise resulted in sub-banded data points to investigate the frequency evolution of the pulsar emission. We then studied the individual modal profiles at each frequency and examined their evolution.

We attempted to fit a combination of Gaussians to all the modal profiles, and a double Gaussian function was found to be the best model. This is a favoured model for our case because, on the single pulse level, the pulsar shows two subpulses within a given pulse, which eventually gives rise to a double-peaked profile. The frequency evolution of these two components of the double Gaussian function was examined for each mode and is plotted in Fig. 3.7. The different panels correspond to the different drift modes, where the mean position of the individual Gaussian peaks (of the double Gaussian function) is plotted against the frequency. The mean positions on the left (in orange) correspond to the leading peak in the Gaussian fitted profile, whereas the ones in blue correspond to the trailing peak. A clear trend is noticeable in the mean positions, which can be seen with increasing frequency for both components.

3.2.7 Probing the emission geometry with polarisation observations

Polarimetric observations can be used to constrain the pulsar geometry and the location of radio emission. The pulsar radiation is thought to be strongly polarised either along or orthogonal to the open magnetic field lines. When the pulsar beam sweeps past the observer's line of sight, the position angle (PA) of the linear polarisation changes, resulting

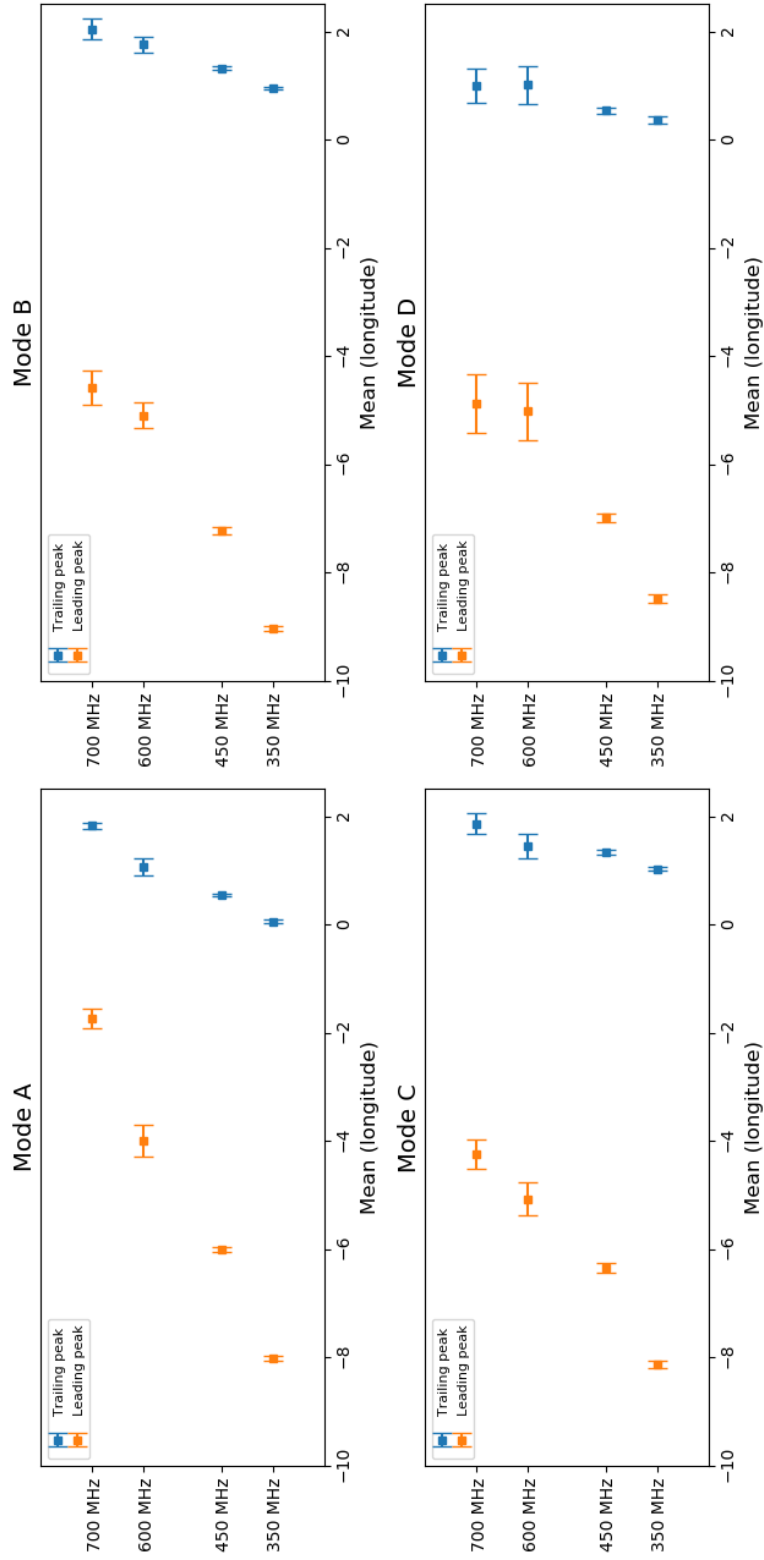


Figure 3.7: Plot of mean longitude position of pulse profile components. The points on the left (orange) correspond to the leading components, whereas the points on the right (blue) correspond to the trailing component of the profile.

in an S-shaped curve. The inclination angle, α , between the magnetic and rotational axes and the impact parameter, β , which is the smallest angle between the locus of the line of sight of the pulsar beam and the magnetic axis, determine the shape of the S-shaped curve. In the rotating vector model (RVM, [Radhakrishnan & Cooke, 1969](#)), the characteristic S-shape curve of PA vs pulse phase is used to determine the geometrical angles for a pulsar. We use this for our analysis to infer the pulsar beam geometry.

To constrain the pulsar geometry and determine the α and β angles, we used the polarimetric data made available by [Johnston & Kerr \(2017\)](#). The data were taken using the Parkes radio telescope (recently given the indigenous name *Murriyang*) at 1.4 GHz with high time and frequency resolution. We used `PSRSalsa` ([Weltevrede, 2018](#)) to fit the RVM and compute α and β from the polarimetric data. For this pulsar, the value of α could not be well constrained. Fig. 3.8 shows the PA fitting for the Parkes data with $\alpha = 23.9^\circ$ and $\beta = 5.7^\circ$, along with the average profile.

Additionally, the steepest gradient (SG), which is defined as $\sin \alpha / \sin \beta$, can be used to estimate the profile shape. For a central cut of the emission beam, the profile will have multiple components with core and conal emission; consequently, the value of SG would be higher. For our case, the value of SG is $\sim 4^\circ / ^\circ$, implying a conal cut of the emission beam.

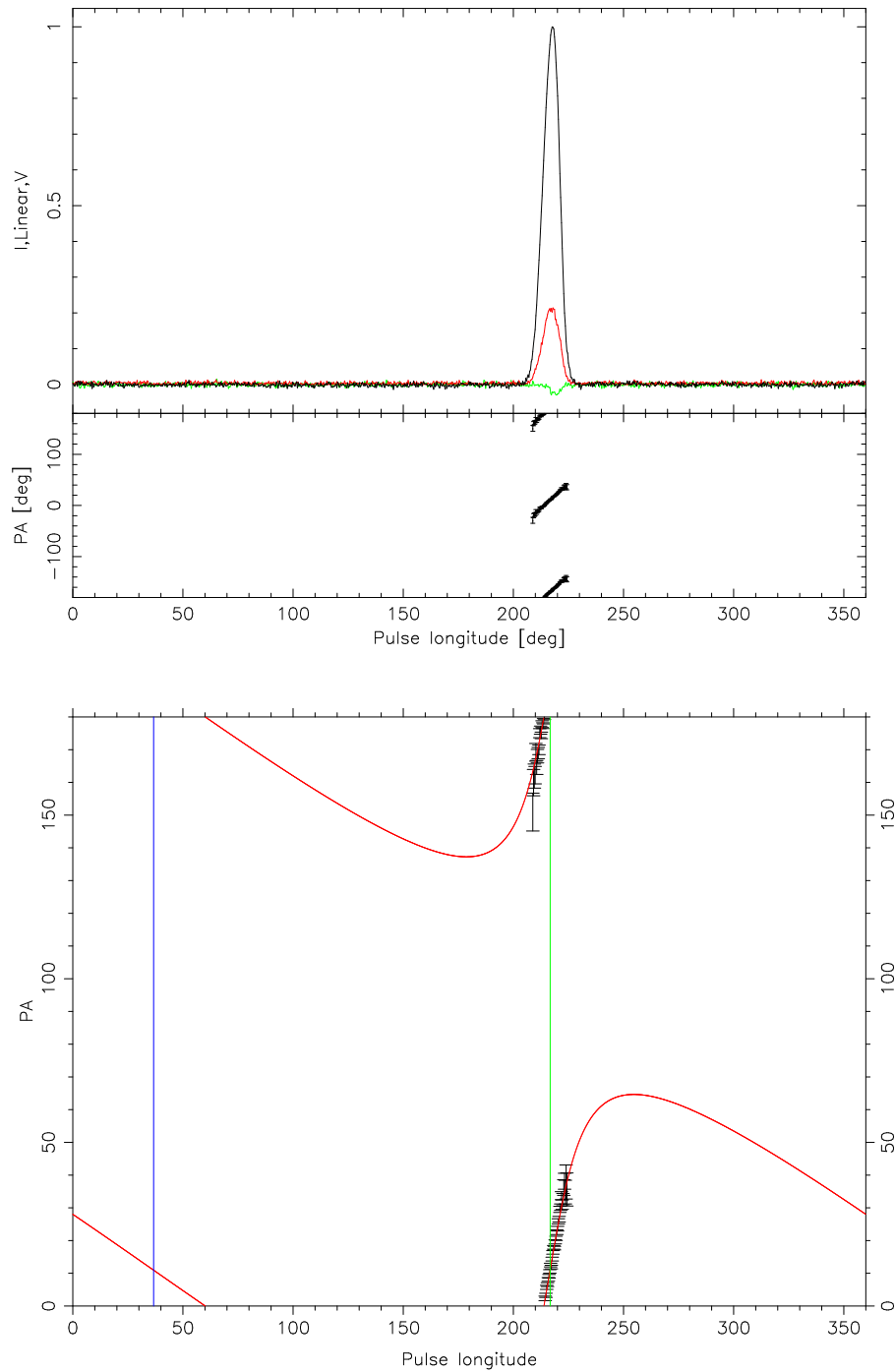


Figure 3.8: *Top*: Average profile of J1822–2256 at 1400 MHz. *Bottom*: Polarisation Angle fit for 1400 MHz profile of J1822–2256 obtained from Parkes data. The green line denotes the zero crossing point of PA, and the blue line is 180° offset from that.

3.2.8 Determination of emission heights for the emission modes

Fig. 3.7 shows how the two components of the average profile change with an increase in frequency; as seen from this figure, the profile becomes narrower with an increase in frequency. This phenomenon, common to many pulsars, is usually ascribed to the radius-to-frequency mapping (RFM, Cordes, 1978), which suggests that emissions at different frequencies originate at different altitudes in the pulsar magnetosphere. The association of higher frequency emission with lower altitudes (and the lower frequency with higher emission altitudes) comes from the dipolar shape of the magnetic field lines expected in the emission region since tangents to the field lines subtend a smaller angle to the magnetic axis closer to the surface, giving rise to a smaller conal opening angle.

To calculate the height above the pulsar surface at which the emission at a particular frequency arises, we need to calculate the half-beam opening angle, Γ , which is determined as the angle between the magnetic axis and the cone of emission. Since the cone has a certain thickness, one can consider the half-opening angle as that corresponds either to the inner or outer edge of the cone or somewhere in the middle. Here, we choose the outer edge since the corresponding points in the profile (i.e. the leading and trailing edges) are relatively easy to measure, even when the components start to merge at higher frequencies. In particular, we assume that the 10% pulse width, W_{10} , is a good approximation to where the emission from the outer conal edge appears. Using the three sides of a spherical triangle formed between the magnetic axis, rotation axis, and line of sight, we can write

$$\cos \Gamma = \cos \alpha \cos(\alpha + \beta) + \sin \alpha \sin(\alpha + \beta) \cos\left(\frac{W_{10}}{2}\right) \quad (3.1)$$

We used $\alpha = 23.9^\circ$ and $\beta = 5.7^\circ$ for this case (as calculated using the 1.4 GHz Parkes data). Once the half beam opening angle has been obtained from eqn. 3.1, we can calculate the angle subtended by the emission site with the magnetic axis, θ , as (Gangadhara, 2004)

$$\sin^2 \theta = -\frac{1}{6} \left(\cos \Gamma \sqrt{8 + \cos^2 \Gamma} + \cos^2 \Gamma - 4 \right) \quad (3.2)$$

Assuming that the radius of the neutron star is much smaller than the light cylinder radius ($r_p \ll R_{LC}$), we can calculate the emission height, r , normalised to the light cylinder radius (R_{LC}) as

$$\frac{r}{R_{LC}} \approx \frac{\sin^2 \theta}{s^2} \quad (3.3)$$

where s is the footprint parameter, and the location of the footprint is on the neutron star surface, which is assumed to be spherical. We have assumed that the radiation from the outer edge of the cone originates from the last open field line, for which $s = 1$. Using the viewing geometry obtained from the Parkes data, and the light cylinder radius, $R_{lc} = \frac{cP_1}{2\pi} \cong 89,450$ km, we calculated the emission heights for all modes separately at the four central frequencies. Fig. 3.9 shows the emission heights at multiple observation frequencies. Here, the different colours correspond to the four modes of subpulse drifting found in our study. We used the α and β values obtained from polarimetric analysis of the high-quality Parkes data, which are different from the ones calculated by [Basu & Mitra \(2018\)](#). The error bars could not be calculated for this case due to the poorly constrained pulsar geometry. However, the trend in emission heights across the different modes, throughout multiple trials of pulsar geometry, remained the same. The possible sources of uncertainty on the emission heights could be the error in constraining α and β values and the error due to signal-to-noise of the average profile, propagating in the 10% profile widths.

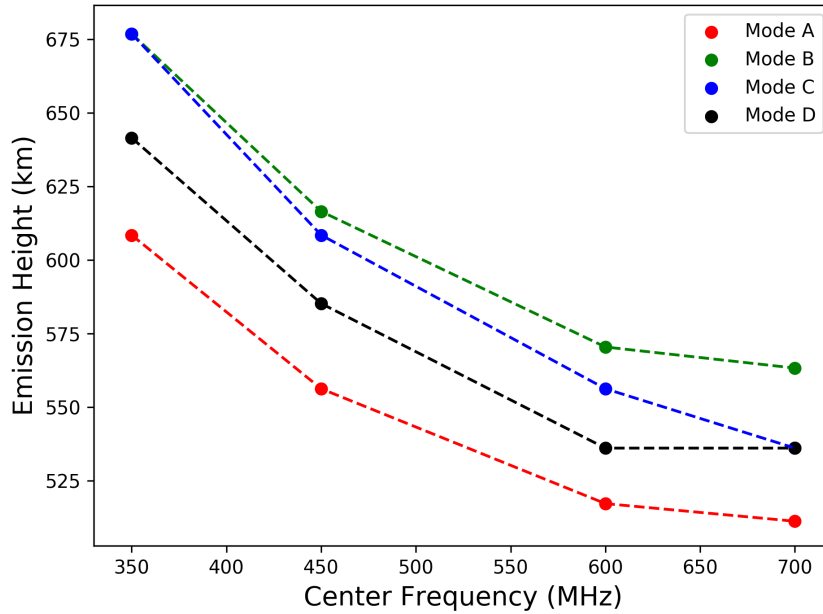


Figure 3.9: Plot of emission heights for different modes with frequency. Different colours represent the different subpulse drifting modes.

3.3 Discussion

In this paper, we have presented the results from the first simultaneous wide-band multi-frequency study on the pulsar J1822–2256 using the uGMRT. This pulsar is known to exhibit subpulse drifting, mode changing, as well as nulling and is, therefore, a promising candidate for studying the pulsar emission mechanism. As discussed in the previous section, our analysis suggests the presence of new features in some of the drift modes of emission, which were not reported by previous work. We also present insightful results relating to mode-dependent emission heights. In this section, we discuss the implications of our results on the pulsar emission process in an effort to shed some light on the possible modifications needed in the carousel model for this pulsar. Specifically, we consider the spark carousel geometry and the relation between different modes and their inferred emission heights.

To summarise, we have found four subpulse drifting modes for the pulsar J1822–2256, including some new features that were not studied before. Modes A and C were commonly found in all previously published literature, with our P_3 values consistent within their error bars. We found another subpulse drifting mode at $P_3 \sim 5.8 P_1$ with interesting features. This mode could be similar to mode B, which was categorised as a non-drifting mode by Basu & Mitra (2018). It was also referred to as mode C in Joshi et al. (2018). Results reported by Basu & Mitra (2018) were from observations made at 322 MHz with 33 MHz bandwidth. However, having higher sensitivity due to a factor of six increase in the observing bandwidth, we and Joshi et al. (2018) have found the drifting nature in mode B (mode C for Joshi et al., 2018). Serylak et al. (2009) also reported the presence of a ‘nulling or rapidly changing drift mode’, which could be the same as mode B in our case. In addition, we have found another subpulse drifting mode - mode D. Even though Basu & Mitra (2018) found a transitional mode A at the same P_3 as our mode D, the primary characteristic between the two modes is different. In the case of Basu & Mitra (2018), they claimed that this mode occurred after mode A in most cases, whereas, in our data, most of the occurrences of mode D are preceded by a null. With such varying values for P_3 for all the modes and order of appearance of modes, the pulsar possibly shows an evolving subpulse drifting behaviour altogether. It is also possible that observations made at different epochs find the magnetosphere in different dynamical states, resulting in observed differences in subpulse drift properties by individual studies.

3.3.1 Spark calculation

We now attempt to determine the number of sparks in the carousel by assuming they are equally spaced in the magnetic azimuthal direction. The behaviour of drift bands is determined by the number of sparks, n , and the rotation rate of the carousel, P_4 , i.e. the time for the sparks to complete one revolution around the polar cap. However, the observed drifting could be aliased due to an under-sampling of the subpulse motion or the

observer's inability to distinguish between subpulses (van Leeuwen et al., 2003). Because we can only observe the position of a subpulse once per pulsar rotation, it is rather difficult to determine the real speed of carousel rotation exactly.

We have found different P_3 values for the different modes of J1822–2256, which can be explained by a change in the number of sparks or the carousel rotation rate. In the general case, the carousel rotation rate may be aliased with the star's rotation, with the observed P_3 obeying the relation

$$\frac{1}{P_3} = \left| \frac{n}{P_4} - k \right| \quad (3.4)$$

Here we have followed the overline notation used by McSweeney et al. (2019), where $\overline{P_3}$ is P_3/P_1 and $\overline{P_4}$ is P_4/P_1 . The parameter $k = [n/\overline{P_4}]$ is the aliasing order, with square brackets denoting rounding off to the nearest integer.

Because of the free choice of P_4 for each mode, it is not easy to find the correct aliasing order, k . However, the carousel rotation speed cannot easily change its magnitude or direction on the timescales in which the drift modes change, which, in our case, is around one pulsar rotation. For PSR B1918+19, Rankin et al. (2013) suggested keeping P_4 constant while allowing a change in n . In that case, k cannot be 0 for all drift modes since, otherwise, the drift rate would be the same for all four modes.

The challenge is, therefore, to find values for $\overline{P_4}$ for which integer values of n_A, n_B , etc. can be found to predict the correct values of $\overline{P_3}$ from eqn. (3.4). Given the ranges of $\overline{P_3}$ values available for each mode (as per Fig. 3.5), it is possible that many solutions can be found that are broadly consistent with the $\overline{P_3}$ values for each mode. Given this, we will opt to favour $\overline{P_4}$ values that are closer to the theoretical value predicted by the Ruderman-Sutherland model, which is

$$\overline{P_{4,RS}} \approx 5.7 \times \left(\frac{P_1}{s} \right)^{-3/2} \left(\frac{\dot{P}}{10^{-15}} \right)^{1/2} \quad (3.5)$$

n_A	n_B	n_C	$\overline{P_{3A}}$	$\overline{P_{3B}}$	$\overline{P_{3C}}$	k	$\sim \overline{P_4}$
14	12	13	17.7	5.2	8.1	+1	14.84
31	33	32	18.0	5.3	8.2	+2	15.08

Table 3.3: Carousel parameters for J1822–2256

where \dot{P} is the spin-down rate (i.e. the first derivative of the spin period), which is $1.35439 \times 10^{-15} \text{ s s}^{-1}$ for PSR J1822–2256 [Manchester et al., 2005](#). For J1822–2256, eqn. (3.5) gives $\overline{P_{4,RS}} \approx 2.79$.

We searched for solutions by brute force, i.e., testing every value $0 < \overline{P_4} \lesssim 30$ at increments of 0.01. For each $\overline{P_4}$, we used eqn. (3.4) to find the best values of n that produce the nominal $\overline{P_3}$ values for each mode. We repeated this exercise for each k in $[-2, -1, 1, 2]$, i.e. up to second-order aliasing.

Interestingly, we were not able to find any solution that was consistent with all four modes by this method. One possible reason for this is our implicit requirement that all four modes belong to the same aliasing order may not hold; it may well be the case that some modes have (for example) $k = 1$, while others have $k = 2$. Nevertheless, we found that solutions with mixed aliasing orders usually required the number of sparks to jump by a large amount between the modes, which seems counter to the types of solutions obtained for other pulsars, for which the number of sparks only ever jumps by one or two during mode switches (e.g. [McSweeney et al., 2019](#), and references therein).

When we restricted our search to just those that satisfied three of the four modes, we were able to find solutions for both first and second-order solutions. The solutions with the smallest $\overline{P_4}$ values tended to be in the range $13 \lesssim \overline{P_4} \lesssim 16$. Table 3.3 shows a few representative solutions that were found for modes A, B, and C for both first and second-order aliasing.

It is interesting to note that, for these solutions, $\overline{P_4}$ is very close to the observed $\overline{P_{3D}} \approx 14$, a scenario in which the $\overline{P_3}$ value predicted by eqn. (3.4) becomes very sensitive

to the precise value of \overline{P}_4 . A situation like this may go some way to explaining the difficulty of finding solutions that fit all four modes simultaneously. However, in the case of PSR J1822–2256, our ability to identify the correct solution is more likely to be limited by the uncertainties on the \overline{P}_3 values rather than the precision used in the search procedure. Nevertheless, we reiterate that, among the solutions found by the above procedure, the most common values found for \overline{P}_4 fell in the range $13 \lesssim \overline{P}_4 \lesssim 16$.

3.3.2 Modes and implications for pulsar emission

In this study, we have identified four distinct subpulse drifting emission modes in our observations and calculated the possible spark configuration for three out of four drift modes. With these calculated numbers of sparks, the occurrence fraction of each mode, and the average burst lengths, we can comment on the steadiness of modes.

With a P_3 of $\sim 18 P_1$, mode A has the largest occurrence fraction and average burst length. Therefore, sparks giving rise to mode A seem to be comparatively long-lasting. The two peaks in the average profile, corresponding to the leading and the trailing edge of the profile, are closest for mode A.

The bursts of mode B, despite being short, show partially organised drifting, along with the largest variation in P_3 values (Fig. 3.5). This mode is possibly the same as the non-drifting mode mentioned in Basu & Mitra (2018) and mode C for Joshi et al. (2018). According to our classification, the defining feature of this mode was the apparent lack of emission in some parts of the drift sequence (Fig. 3.1). The average profile of this mode shows two widely separated components, with a generally large P_2 value and the broken drift sequences. According to our calculation, mode B has the smallest burst length, and it shows the second-highest occurrence fraction. Using these characteristics, we can infer that the sparks responsible for mode B are the most unstable, i.e., short-lived. This mode was also seen to be the most susceptible to pseudo nulls, which are generally two to three pulses wide. For this pulsar, most of the pseudo nulls are seen around mode B. This could

be due to the relatively low stability of sparks; therefore, higher chances of the observer's line of sight passing through a minimum between sub-beams.

Mode C, in our observations, occasionally shows the occurrence of drifting that is akin to mode B, i.e. broken drift sequences. However, the primary difference between the two modes is that the P_3 value is larger for mode C, and the drift sequences do not generally have more than one break. Compared to mode C mentioned in the previously published literature, this mode shows a slightly different P_3 value but still within the error bars. On average, in our data, the burst length for mode C is 15 pulses, which is considerably higher than that of mode B. Frequent transitions between mode B and mode C were also noted and are generally bridged by the occurrence of a pseudo-null. These pseudo nulls, as mentioned in [Maan \(2019\)](#) for PSR B1237+25, may represent the chance positioning of the observer's line of sight across the minima between the sub-beams in the carousel, as against the physical cessation of the emission in the actual nulls.

The least observed mode in our data is mode D, with an occurrence fraction of about 6%. [Basu & Mitra \(2018\)](#) found a transitional-A mode at a similar P_3 , which was seen occasionally when the pulsar transitions from mode A to some other mode. Interestingly, in our case, most of the occurrences of this mode were preceded by a null. We did not find any correlation between the occurrence of mode D and mode A. The drifting pattern of this mode looks similar to mode A but with a different P_3 value of $14 P_1$. Given the low occurrence rate and a large average burst length, we can interpret that the sparks responsible for this mode are long-lasting but stay dormant for longer times and activate less frequently.

The phenomenon of subpulse drifting is thought to be due to the rotation of conal sparks around the magnetic axis. When the line of sight cuts through the conal part of the emission beam, subpulse drifting is observed. The closer the line of sight moves towards the magnetic pole, the less prominent will be the observers drifting. In our case,

drifting is observed throughout the full profile, implying that the observer's line of sight is possibly cutting through the conal sparks. This is also in accordance with the inference made by [Basu & Mitra \(2018\)](#), where they have used the steepest gradient point of the polarisation position angle to suggest that the observer's line of sight cuts the emission beam tangentially. If the line of sight cuts through the core region of the pulsar beam closer to the magnetic pole, no drifting will be observed in the section corresponding to the core region. This implies that the mean position of the profile component will not change. However, as shown in [Fig. 3.7](#), both the profile components, trailing and leading, are drifting with a certain trend in frequency, implying that the observer's line of sight is cutting through the conal sparks.

In addition, our analysis reveals a different evolution of the leading and trailing profile components with frequency. As shown in [Fig. 3.7](#), the leading components show a higher degree of evolution than the trailing component. We also calculated the aberration and retardation effects which could possibly affect the frequency-dependent shifts. However, our calculations (based on the heights inferred in the following section) showed the effects to be too small to cause any noticeable change. Therefore, such behaviour can be explained with a carousel that might be offset from the magnetic axis or has an irregular shape ([Jones, 2013](#)). In such a scenario, the sparks in the trailing component could be closer to the magnetic axis and, therefore, show a lower degree of frequency evolution than the sparks in the leading profile component, which might be further away from the magnetic pole.

3.3.3 Emission heights for modes

Using the radius to frequency mapping explanation, we extracted the information about the emission heights from our multi-frequency observations of J1822–2256. Based on our calculations, we find that this pulsar's emission heights depend upon the pulsar geometry, specifically α , which is not well constrained. Using the Parkes 1400 MHz data, we have

constrained the emission heights to ~ 500 to 700 km in the observed frequency range with the geometry that we find most plausible.

As evident from the calculation in section 3.2.8, the emission heights are related to the profile width. Consequently, one can notice that the profile for mode A is narrower, which can be because the open magnetic field lines are not as much separated at lower heights. The same argument follows for the other modes as well, where mode B shows a broader profile than mode C and is emitted from a higher emission height.

Interestingly, we also noticed that the emission heights are anti-correlated with P_3 . Thus, mode B, which has the lowest P_3 value, is emitted from a higher altitude in the pulsar magnetosphere than mode A, which has a higher P_3 value and is inferred to have lower emission heights. A similar trend of heights is followed at all the frequencies as well as multiple trial geometries. Considering only the emission from modes A, B, and C (accounting for almost 94% of the total pulsar emission), some spark solutions infer that the emission heights are proportional to the number of sparks calculated for each of the modes. However, our spark analysis shows multiple possible solutions for this pulsar. Hence, other clues, such as the modal profile width, P_2 , P_3 , etc., can help determine which spark solution is more likely. To the best of our knowledge, it is for the first time that such a trend between P_3 and emission height has been seen in a sub-pulse drifting pulsar. It can potentially serve as a vital clue for understanding the pulsar emission process and the spark behaviour in the pulsar magnetosphere.

3.4 Summary

In this paper, we have presented the results from the first wide-bandwidth single pulse study of PSR J1822–2256, covering a frequency range of 300-750 MHz. Observations were made using the upgraded GMRT in the dual-frequency mode. Our analysis confirms the previously reported subpulse drifting modes and uncovered some additional features

which were not studied earlier, possibly due to the limited sensitivity of those observations. Using our observations, we have been able to study the drifting behaviour of this pulsar over a wider frequency range. We have presented a new subpulse drifting classification for this pulsar, based on the modes' average profiles and the corresponding P_3 values. We identify at least four different subpulse drifting modes with clearly distinguishable characteristics.

Our analysis also reveals that the pulsar exhibits short-duration pseudo nulls in addition to genuine nulls. On an individual pulse level, both types of nulls show similar noise-like behaviour. However, a low-level emission is observed in the average profile constructed from pseudo nulls across the observing frequency range. These pseudo nulls are primarily present in modes B and C, which have the lowest P_3 values and occasionally exhibit the apparent lack of emission in the drift bands. Previous studies suggested the presence of such pseudo nulls due to the observer's line of sight passing through a minimum of sparks.

We have also studied the frequency-dependent subpulse behaviour of different modes by segmenting the 200 MHz observing bandwidth into 100 MHz sub-bands. This exercise resulted in sub-banded data points to investigate the frequency evolution of the pulsar. Based on an observed evolution of profile components, where the leading components seem to evolve faster than the trailing component, we have proposed that the underlying carousel could either be offset from the magnetic pole or have an irregular shape. Such a carousel geometry would imply certain sparks closer to the magnetic pole, showing a lower degree of frequency evolution.

With the resultant multi-frequency measurements, we were also able to demonstrate the confirmation of radius-to-frequency mapping for each of the modes across the frequency range of our data. Further, we used the modal frequency evolution to estimate the emission heights. Our results show that the emission heights at different frequencies are dependent upon the mode. Our analysis has revealed an anti-correlation between the

inferred emission heights and the measured P_3 values. Interestingly, solutions were found in which the inferred emission heights were directly correlated to the number of sparks. If such a correlation is true, this will imply that the numbers of sparks in a mode are directly related to the emission height, for at least 94 % of the emission for this pulsar. Our results may provide vital clues toward understanding the pulsar emission mechanism and refining the spark model.

Chapter 4

Single-pulse study of PSR J1820-0427

“Never cruel or cowardly. Never give up. Never give in.”

- The Doctor

This chapter is a faithful reproduction of *Single-pulse analysis and average emission characteristics of PSR J1820–0427 from observations made with the MWA and uGMRT* by [Janagal et al. \(2023\)](#).

Pulsars are rotating neutron stars, which are the sites of highly energetic physical processes owing to their extreme environment of strong gravitational and magnetic fields and high densities. The impeccable periodicity of pulsars was one of the qualities that led to their discovery ([Hewish et al., 1968](#)). Their rotation causes highly collimated radiation beams to sweep across the observer’s line of sight for only a brief amount of time, producing a pulsed emission (e.g., [Manchester & Taylor, 1977](#)). Radio emission from pulsars is conjectured to originate within the open field lines in the magnetosphere, with the emission beam centred on the magnetic axis (e.g., [Radhakrishnan & Cooke, 1969](#)). However, despite a wealth of observational data, the emission mechanism remains not well understood.

Radio pulsars are known to exhibit a variety of amplitude modulation in single pulses,

owing to both intrinsic and extrinsic factors. Even though the integrated pulse profile stays stable over the long term, individual pulses show considerable variation in intensity and shape on a wide range of time scales. The intrinsic variabilities affect pulsar emission at multiple time scales. At the shortest time scales ($\sim \mu\text{s}$), pulsars reveal single pulse variabilities such as micro-structures (e.g., [Craft et al., 1968](#)), giant pulses (e.g., [Hankins et al., 2003](#); [Heiles & Campbell, 1970](#); [Staelin & Reifenstein, 1968](#)), and giant micro pulses (e.g., [Johnston et al., 2001](#)). At longer time scales of seconds to minutes, the variability is seen in the form of drifting sub-pulses (e.g., [Drake & Craft, 1968](#); [Janagal et al., 2022](#)), where, as the pulsar rotates, substructures within the pulse are seen to form a regular drifting pattern with longitude. On similar time scales, pulsars also show ‘moding’ where they switch between multiple emission or drifting modes, average pulse profile, intensity, polarisation, etc. (e.g., [Backer, 1970a](#); [Cordes, 2013](#)). On the scale of a few seconds to several minutes, cessation of emission from some pulsars is observed for a certain amount of time, known as nulling (e.g., [Backer, 1970b](#)) All these features comprise the intrinsic variability behaviour of single pulses.

At radio frequencies, apart from the intrinsic activity of the pulsar, propagation effects also cause inter-pulse variability (e.g., [Lyne et al., 1971](#); [Rankin et al., 1970](#)), in the form of extrinsic factors. The interstellar medium (ISM) plays a role in the modulation of pulsar signals that we observe. Propagation of radio pulsar emission through the ISM causes scattering of the signal and shows up as scintillation on the different timescales of up to tens of minutes (e.g., [Lang, 1969](#); [Sutton, 1971](#)).

The time variable plasma processes in the pulsar magnetosphere can be most meaningfully investigated using the analysis of single pulses. As mentioned earlier, these individual pulses are affected by the intrinsic and extrinsic factors leading to significant amplitude modulation, which often have a frequency dependence. Studying the single pulses at multiple frequencies allows us to not only sample different regions of the magnetosphere (Radius to Frequency Mapping, [Cordes \(1978\)](#)) but also understand the energy

variation with time and frequency, ultimately providing clues to the possible emission mechanisms. Thus, multi-frequency studies of single pulses can be used to investigate the emission properties of the radiation processes in the magnetosphere. A detailed study of these individual pulses can yield constraints on the theoretical models of emission and the distribution of emitting particles, bringing useful insights into pulsar emission physics.

The Stochastic Growth Theory (SGT) has been used to explain the observed pulse energy distribution of several pulsars (e.g., [Cairns et al., 2003a,b, 2004, 2003c](#); [Robinson, 1995](#)). Theories such as the SGT, help understand the possible emission mechanisms that may give rise to the observed log-normal statistics of single pulse intensities. Some of these aspects can be meaningfully investigated using simultaneous single-pulse observations spanning a large range in frequency. Observational investigations by [Kramer et al. \(2003\)](#) studied the single pulse behaviour of pulsars PSR B1133+16 and PSR B0329+54 at multiple simultaneous frequencies from 200 MHz to 5 GHz. Their results shed light on the frequency-dependent behaviour of pulse-to-pulse modulation properties and the asymmetric distribution of single pulse spectral indices. Another aspect is the prevalence of log-normal type statistics across a wider population of pulsars. Using the data from the High Time Resolution Universe survey, [Burke-Spolaor et al. \(2012\)](#) studied the single pulse energetics and modulation of 315 pulsars at 1352 MHz. They found that over 40% of the observed sample exhibited a log-normal pulse energy distribution, only a few displayed a Gaussian pulse energy distribution, while the others were not fitted by either distribution. Single pulse analysis of this kind provides new avenues for looking at the instantaneous plasma activity in the pulsar magnetosphere, and such studies have the potential to yield valuable clues to understanding the spectral behaviour of single pulses and the overall pulsar emission mechanism.

Single pulse studies of pulsars necessitate exceptionally high-quality data. The main requirements for such an investigation are - (1) the pulsar should be bright such that single pulses are detectable, (2) low Radio Frequency Interference (RFI) conditions, (3)

single pulses should be free of other phenomenologies such as nulling or moding. Often, a combination of these conditions is hard to achieve, thus limiting such studies. PSR J1820–0427 is a bright “normal” pulsar, with a period of 0.598 seconds and a dispersion measure (DM) of $84.435 \text{ pc cm}^{-3}$. The pulsar has a featureless profile at low frequencies and does not show any kind of modulation (e.g., subpulse drifting, moding, or nulling). Such typical character of the source makes PSR J1820–0427 an attractive candidate for studying the emission and basic characteristics of pulsars.

Single pulse studies have been rare in the past due to limited telescope sensitivity. Pulse-to-pulse variability and pulse fluence analyses of pulsars have often evaded attention, mainly because of the low single pulse signal-to-noise ratio (S/N). However, such studies can provide a unique instantaneous window into the pulsar magnetosphere and are thus important in gaining insight into the pulsar emission process. In this work, we present a single pulse analysis of the pulsar PSR J1820–0427 using high-quality data obtained from the upgraded Giant Meterwave Radio Telescope (uGMRT) and the Murchison Widefield Array (MWA). In this paper, we investigate the pulse-to-pulse variability and their frequency dependence to study pulsar emission further. The details of observations used in this work are mentioned in section 4.1. The phased array processing, imaging analysis, and single pulse calibration are described in section 4.2. This section also outlines the novel approach we have developed to measure single pulse flux densities. These calibrated single pulse flux densities are further utilised to study the pulse-to-pulse modulation through investigations of spectral index variation, fluence distribution, etc. We have also studied the average emission characteristics of J1820–0427 and their evolution at simultaneously observed frequencies. The analysis and results from our study are elaborated in section 4.3. We have discussed the implications of our results in section 4.4, and section 4.5 presents a summary of our work.

4.1 Observations

Observations of PSR J1820–0427 were carried out using the uGMRT and the MWA at multiple epochs. The uGMRT was used in a dual-band phased-array mode to simultaneously cover the frequency range of 300–500 and 550–750 MHz. The MWA observations were made in the 170–200 MHz band. Thus, the pulsar was observed over a frequency range from 170 to 750 MHz, i.e. more than two octaves. A summary of observational details is presented in Table 4.1, and further details are summarised below.

4.1.1 The uGMRT

The Giant Metrewave Radio Telescope (GMRT) is a radio interferometric array with 30 antennas, each of 45-meter diameter, spread over an area of 28 km² in a Y shape (Swarup et al., 1991). After a recent upgrade, the system was equipped with wide-band receivers and digital instrumentation to provide a near-seamless coverage in frequency from 120 MHz to 1600 MHz (Gupta et al., 2017; Reddy et al., 2017). In the phased array mode, the incoming signals from all antennas are combined coherently to achieve maximum sensitivity for pulsar observations. The observations were made simultaneously at Band 3 (300–500 MHz) and Band 4 (550–750 MHz) of the uGMRT, where only the total intensity was recorded. For these observations, 13 antennas from the central square and the arms were configured at Band 3. For Band 4, 13 antennas from the Y-shaped arms were used, therefore using the largest baselines. The observations were made at two epochs, ~ 10 days apart, simultaneously at both frequency bands in the identical configuration. Along with the phased array observations, the uGMRT also recorded visibilities that can be used to image the pulsar field. At each epoch, the pulsar was observed for roughly one hour, giving close to 6000 pulses per epoch (see Table 4.1).

In our uGMRT observations, the PSR J1820–0427 showed very bright radio pulses, along with low RFI conditions, which made this observation suitable for single pulse analysis. The wide bandwidth of uGMRT observations and the impeccable signal-to-

MJD	Receiver	Frequency (MHz)	Δf (kHz)	Δt (μ s)	Δt_{eff} (ms)	N_{Ant}	N_{Chan}	N_{Pulses}	Obs. Time (min)
59009	uGMRT	300-500	48	327.68	0.43 - 1.25	13	4096	6020	60
59009	uGMRT	550-750	48	327.68	0.33 - 0.39	13	4096	6020	60
59019	MWA	170-200	10	100	1.43	128	3072	4515	45
59019	uGMRT	300-500	48	327.68	0.43 - 1.25	13	4096	6020	60
59019	uGMRT	550-750	48	327.68	0.33 - 0.39	13	4096	6020	60

Δf is the frequency resolution of observation

Δt is the time resolution of observation

Δt_{eff} is the effective time resolution

N_{Ant} is the number of antennas (tiles for MWA) used for the observation

N_{Chan} is the number of frequency channels used in the observation

N_{Pulses} is the number of pulses recorded in the observation

Table 4.1: Table of observations for PSR J1820–0427

noise ratio resulting from its high sensitivity is evident in Fig. 4.1. Here, the y -axis shows the increasing frequency scale from 300-750 MHz, and the x -axis shows a part of the entire pulsar period. All the intensities are normalised to adjust the colour scale in the 0-1 range. Band 3 of uGMRT covers 300-500 MHz and Band 4 550-750 MHz, and an empty region of zero intensity was added in the 500-550 MHz range. The signal strength changes as a function of frequency due to the pulsar's spectrum, and moreover, the pulsar profile evolution with frequency can also be noted, where the profile seems to get wider with decreasing frequency.

4.1.2 The MWA

The MWA observations were made at a central frequency of 185 MHz. The MWA comprises 128 tiles, (where a 'tile' is a $4m \times 4m$ dipole array) and during our observations, operated in Phase-2 extended array configuration (Tingay et al., 2013; Wayth et al., 2018). The data were recorded using the Voltage Capture System (VCS, Tremblay et al. (2015)), which records Nyquist-sampled dual polarisation voltages. In this mode, the channelised voltages are recorded from each tile, which can be processed offline using the software tied-array beamformer (Ord et al., 2015), by summing coherently after calibration. We observed the pulsar in full polarisation mode at 185 MHz over a contiguous bandwidth of 30.72 MHz, spread across 3072×10 kHz fine channels. The recorded voltages can also be used to create visibilities, and further obtain the images and source flux at 185 MHz. PSR J1820-0427 was one of the 18 pulsars detected in a single observation under the project G0071, the data from which have been utilised for different projects including developing image-based methods for identifying pulsar candidates (Sett et al., 2022), and for investigating the ionospheric refraction offsets in tied-array beamforming (Swainston et al., 2022a). Details on these pulsars, including their profiles and flux densities are reported in a forthcoming publication (Bhat et al., 2023a,b). For the data used in this work, the pulsar was observed for 45 minutes, giving close to 4500 pulses per epoch.

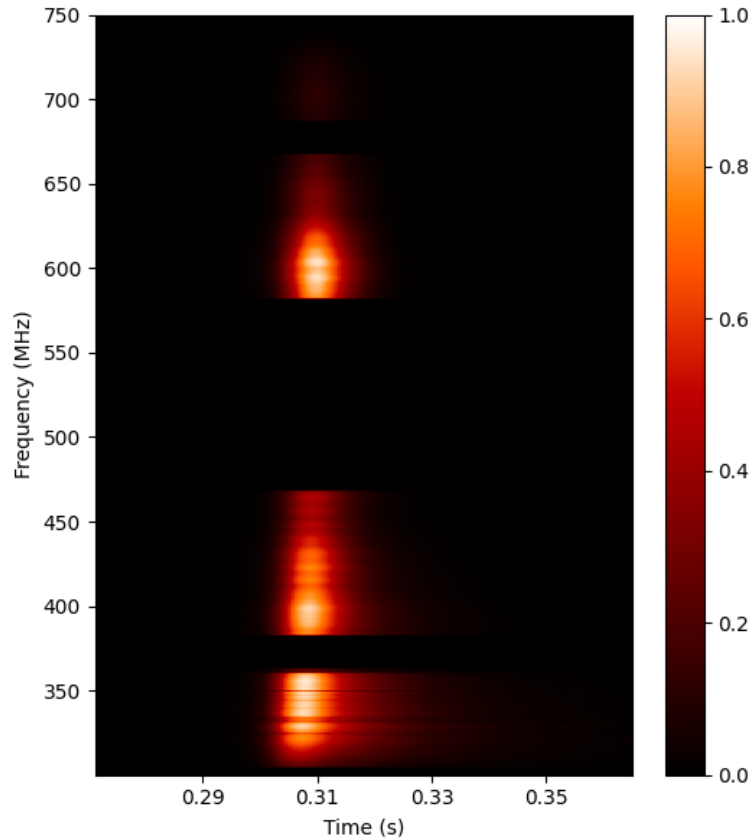


Figure 4.1: Wide-frequency spectral evolution of PSR J1820–0427 observed using uGMRT. The figure combines Band 3 (300–500 MHz) and Band 4 (550–750 MHz) observations, with frequency increasing from bottom to top. The colour contrast shows the intensity of the pulsar. Apart from the range between 500–550 MHz, the missing chunks correspond to the persistent RFI channels and are removed automatically.

4.2 Data Processing

As described earlier, observations were made such that both beamformed and visibility data can be extracted from both MWA and uGMRT. In the following sections, we describe the procedures adopted for data processing for both phased array and imaging data from these two telescopes.

4.2.1 uGMRT

4.2.1.1 Imaging

The visibility data were recorded in the Long Term Accumulation (LTA) format and were processed using SPAM (Source Peeling and Atmospheric Modeling, [Intema \(2014a\)](#)) pipeline and CASA (Common Astronomy Software Applications, [McMullin et al. \(2007\)](#)) for calibrating the single pulses obtained from the beamformed data. The CASA package is a data processing package used to process data from both single-dish and aperture-synthesis telescopes. SPAM is radio astronomy data processing software developed by [Intema et al. \(2009\)](#) (see also [Intema, 2014b](#)), which is a fully automated software based on the Astronomical Image Processing System (AIPS, [Greisen \(1998\)](#)). SPAM includes direction-dependent calibration, modelling, and imaging for correcting ionospheric dispersive delays. It uses the ParselTongue interface ([Kettenis et al., 2006](#)) to access AIPS tasks, files, and tables. SPAM consists of two main processing steps: (1) a pre-processing part that converts raw data from individual observing sessions (LTA format) into pre-calibrated visibility data sets, and (2) a main pipeline which converts pre-calibrated visibility data into stokes I continuum image.

We used the SPAM pipeline to obtain the Stokes I continuum image. After converting LTA files in the .UVFITS ¹ format, SPAM derives the calibration and flagging information from the primary calibrators. These solutions are then applied to the target. The data were automatically split into smaller subbands by SPAM, such that the primary beam for each subband does not vary substantially within the frequency range. SPAM automatically splits the Band 3 data into six equal subbands, whereas Band 4 data was split into four subbands of equal bandwidth. These subbands were further used to study the frequency evolution of the pulsar emission.

Each sub-band was processed individually, keeping the reference frequency same for all the subbands created from one band. For Band 3, the reference frequency was 400 MHz

¹a FITS file with telescope metadata and visibility information

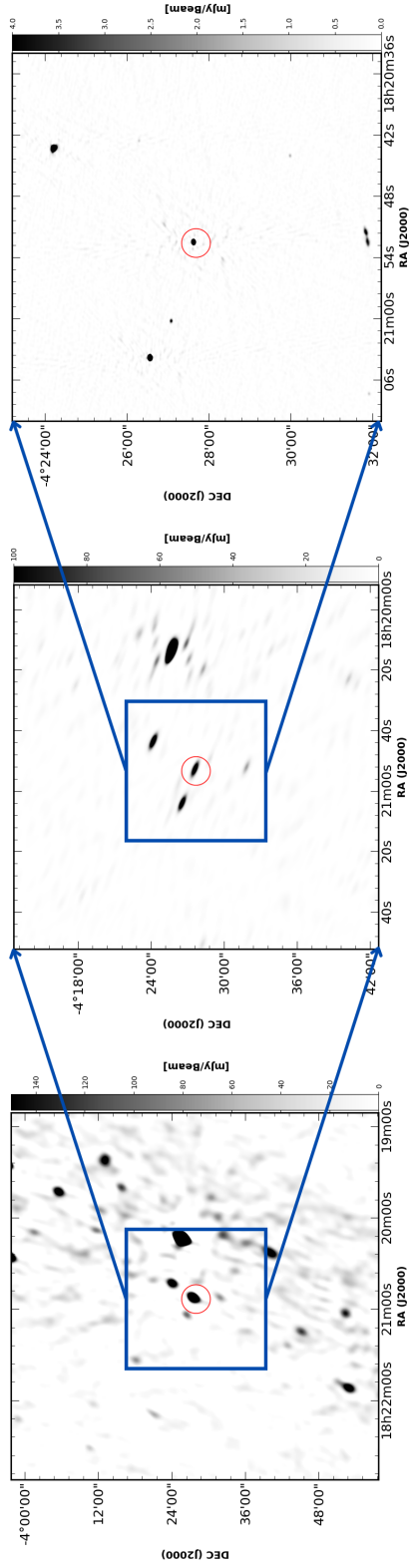


Figure 4.2: *Left*: MWA Stokes I image of the $1 \times 1 \text{ deg}^2$ field (at 185 MHz) with the position of the target pulsar in the centre, with the rms sensitivity is $\sim 500 \mu\text{Jy/beam}$. *Middle*: Combined uGMRT Band 3 (300-500 MHz) image of $0.5 \times 0.5 \text{ deg}^2$ field, where the rms sensitivity is $\sim 300 \mu\text{Jy/beam}$. *Right*: Combined uGMRT in Band 4 (550-750 MHz) image of $0.15 \times 0.15 \text{ deg}^2$ field, with a much higher sensitivity of $\sim 100 \mu\text{Jy/beam}$. In all the images, the pulsar is at the phase centre, as indicated by the red circle.

Frequency (MHz)	Bandwidth (MHz)	Flux \pm Error (mJy)	Off-source RMS (μ Jy)/beam	Restoring Beamsize
185	30.72	790 \pm 63	500	83'' \times 55''
317	33	256.58 \pm 2.06	360	73'' \times 25''
350	33	206.15 \pm 0.85	340	66'' \times 23''
383 ^a	33	132.80 \pm 1.30	380	60'' \times 21''
417	33	145.84 \pm 0.14	110	55'' \times 19''
450	33	125.87 \pm 0.45	120	51'' \times 18''
483	33	-	-	-
575	50	76.43 \pm 0.53	110	5'' \times 3''
625	50	62.60 \pm 0.38	80	4'' \times 3''
675	50	50.30 \pm 0.37	80	4'' \times 3''
725	50	41.96 \pm 0.38	80	4'' \times 2''

^a Only for epoch 1

Table 4.2: Multi-frequency flux density measurements of J1820–0427 obtained from imaging the pulsar field using MWA (185 MHz) and uGMRT(317-725 MHz). The flux densities and their respective errors are added in quadrature for multiple epoch observations. Data at 483 MHz was unusable and was discarded for this work. At Epoch 2, data at 383 MHz was unusable, thus only the values from Epoch 1 were used.

and for Band 4, it was 650 MHz. The targets in each subband are then calibrated, where the different target fields are separated. In the main SPAM pipeline run, the representative resolution of the model image was set as 10'' for Band 3 subbands and 6'' for Band 4 subbands. Out of the total six subbands in epoch 1 Band 3 observation, only five were usable. However, for epoch 2, Band 3, we had to discard data from two subbands due to poor data quality. The poor data quality in these cases is due to RFI being limited to certain frequencies. Thus, subbands where most of the data were flagged by SPAM were discarded, whilst subbands with no persistent or frequency-limited RFI were used in further analysis. Each SPAM pipeline run on a sub-band yielded a final image and a calibrated visibility data set (.SP2B.CAL.RR.UVFITS). Imaging was performed on the final calibrated data using the CASA task `tclean`. To get the flux density of PSR J1820–0427, we used the polygon drawing option in `casaviewer` to roughly make a polygon around the source of interest and then fit the selected region using a Gaussian to get the integrated flux density value.

As seen from Fig. 4.2, our analysis attains S/N of ~ 1000 for simultaneous imaging detection of this pulsar. The observation details and imaging results for all the observed frequencies are summarised in Table 4.2. An image of the pulsar field at Band 3 and 4, combining all the subbands, is shown in Fig. 4.2. The Band 3 image (middle) shows a 0.5-degree cropped region around the pulsar, and the Band 4 image (right) shows a 0.15-degree region around the pulsar. In the images, the pulsar is at the phase centre, denoted by a red circle. The colour bar shows the associated flux density scale in mJy/beam. The Band 3 image in Fig. 4.2 is visibly elongated, as compared to the Band 4 image. This is because the telescope configuration used for Band 3 observations comprised primarily antennas located within the central square plus a few additional antennas, thus covering predominantly shorter baselines ($\lesssim 1$ km). However, Band 4 observations were made using antennas located along the three arms that make the Y-shaped array, and hence covering mostly longer baselines (~ 1 -25 km).

4.2.1.2 Phased Array Beam

The uGMRT phased array data were recorded with a time resolution of $327.68 \mu\text{s}$ and a frequency resolution of 48.83 kHz. The 200 MHz observing band was split into 4096 frequency channels. The resulting data were written in the filterbank format and subsequently converted to single pulse archives using the DSPSR package (van Straten & Bailes, 2011).

Each single pulse archive file was split into multiple subbands that were identical to those used in the SPAM pipeline, using the `psrsplit` subroutine of PSRCHIVE (Hotan et al., 2004). For Band 3 observations, all single pulse archives were split into six subbands, with centre frequency matching the SPAM subband files. Similarly, single pulse archives from Band 4 observations were divided into four subbands. Single-pulse archives of each frequency subband were then frequency averaged and combined using the `pam` and `psradd` routines from PSRCHIVE. Data corresponding to the unusable SPAM subbands

were discarded. The phased array observation made using uGMRT showed a total S/N of close to 10,000, thereby yielding a mean single pulse S/N of ~ 100 . The data were also manually searched for stray RFI occurrences using the interactive RFI zapping subroutine `pazi` of PSRCHIVE. The RFI-excised file was then converted into an ASCII format, which contained the single pulse time series. This time series was subsequently calibrated in units of Jansky (Jy), the details of which are described in section 4.2.3.

4.2.2 MWA

4.2.2.1 Imaging

The xGPU software correlators (Clark et al., 2013) were used to create “visibilities” at 1s time resolution from the raw voltages recorded with the VCS. These visibilities were then converted into CASA measurement set format (McMullin et al., 2007) using the COTTER software (Offringa et al., 2015). The application of calibration and the removal of RFI-affected channels using AOFlogger (Offringa et al., 2012) were also done during this conversion. The calibration solutions were obtained from the Murchison Widefield Array All-Sky Virtual Observatory (MWA-ASVO, Sokolowski et al. (2020)). WSCLEAN (Offringa et al., 2014) was used to form images in the instrumental polarisation, which were then converted to Stokes IQUV images using the MWA full embedded element beam model (Sokolowski et al., 2017). The images generated were 8192×8192 pixels, with a pixel size of 0.049 degree/pixel, producing $40^\circ \times 40^\circ$ images. The mean standard deviation of the Stokes I image used for processing is ~ 5 mJy/beam around the centre of the image (see Sett et al. (2022) for further details). For PSR J1820–0427, the estimated flux density at 185 MHz was 790 ± 63 mJy. Fig. 4.2 (left) shows the $1 \times 1 \text{ deg}^2$ region around the pulsar (red circle) at 185 MHz.

4.2.2.2 Phased Array Beam

The MWA phased array data were generated with a time resolution of $100\mu\text{s}$ and a frequency resolution of 10 kHz. The 30.72-MHz observing band was centred at 185 MHz. For the MWA tied-array beamformer, signals from each antenna were recorded by the MWA VCS. The voltages from all antenna elements are then calibrated and combined coherently (Ord et al., 2019), in offline processing on the Pawsey supercomputer. The resulting data were written in the PSRFITS format (Hotan et al., 2004) and were subsequently converted to single pulse archives using the DSPSR (van Straten & Bailes, 2011) and PSRCHIVE (Hotan et al., 2004) package. The data were exceptionally clean and required no RFI excision. However, the mean single pulse S/N ~ 10 , and therefore, the data quality is not good enough to perform a detailed single pulse analysis. The single pulse archives were thus time-scrunched, thus giving an average profile, which was further converted into ASCII format for further analysis.

4.2.3 Flux Density Calibration

Flux density calibration for pulsar observations generally relies on the use of noise diodes, which are typically available for most single-dish telescopes such as Parkes (Murriyang). Even though the GMRT antennas are equipped with switchable noise diodes, their synchronisation across the array is currently not a functional mode for the uGMRT. We have, therefore, developed a new method that takes advantage of the fact that concurrent imaging is possible with uGMRT while recording beamformed (phased array) data. Basically, visibility data are imaged first to obtain calibrated images (in units of Jy), which are then used to bootstrap to achieve a first-order calibration of the beamformed data in flux density units.

The underlying assumption is that the sensitivity of the telescope is comparable in both modes of operation, i.e. phased array and imaging interferometer. This would necessarily imply that the RMS noise of the receiver is identical for the beamformed

pulsar detection using the phased array beam and an imaging detection using the cross-correlated visibilities. Therefore, using the off-source RMS from each image (see Table 4.2) and applying a suitable scaling factor, we have calculated the equivalent RMS of the off-pulse region (in the phased array mode) of the average pulsar profile as

$$\sigma_{\text{PA}} = \sqrt{n_{\text{binoff}}} \times \sigma_{\text{Img}} \quad (4.1)$$

where σ_{PA} is the RMS value in the phased array mode, σ_{Img} is the image RMS, and n_{binoff} is the number of bins in the off-pulse duration. Using the average pulsar profile for each frequency, the on-pulse region was defined as where the pulse intensity drops to less than 5% of the peak intensity. The quantity n_{binoff} was then calculated by subtracting the number of bins in the on-pulse region from the total number of phase bins in the pulse profile. This scaling factor accounts for a fraction of the pulsar period during which no emission was seen from the pulsar, i.e., when the pulsar was “off” in its duty cycle. Further, according to our assumptions, this σ_{PA} should be the same as the RMS noise of the off-pulse region in the averaged profile (arbitrary units). Therefore, we calculated the conversion factor $\sigma_{\text{PA}}/\sigma_{\text{offpulse}}$ and applied it to our analysis to bring the beamformed time series data in physical units (Jy). As a useful cross-check, we calculated the mean flux density from the average profile of the scaled beamformed data. This number, in principle, should be equal to the flux density obtained from the imaging analysis, assuming various factors that impact or alter the sensitivity achievable in practice are accounted for (e.g. some degree of de-phasing of the array that may be caused over time). Barring a few outlier cases, the calculated flux density values were found to be in $\sim 20 - 30\%$ agreement with the measured flux density values. We have, therefore, used these calibrated time series to perform all the analyses henceforth.

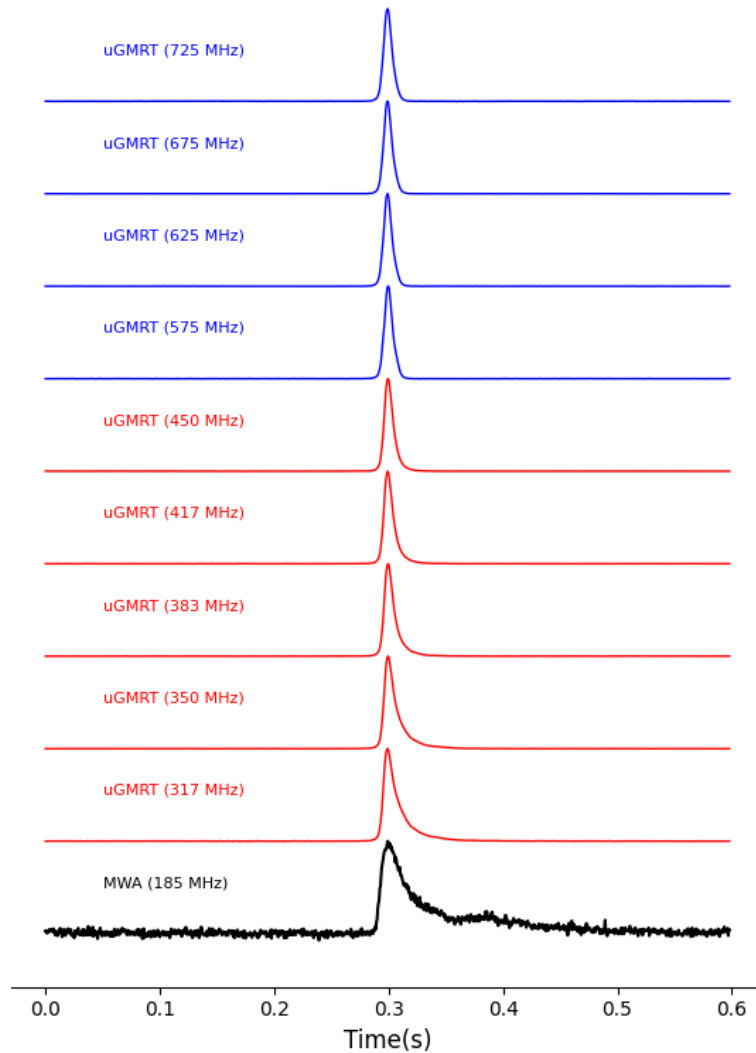


Figure 4.3: Normalised average profiles of PSR J1820–0427 at all the observed frequencies from 185 MHz to 750 MHz. The 185 MHz observation was made using MWA, while the rest were made using uGMRT. The MWA profile has 512 time bins, whereas the uGMRT profiles are made with 1024 time bins. In the figure, x -axis is the time scale, with the average profile peaks aligned at the centre. The average profiles made using the uGMRT data show the impeccable data quality with off-pulse intensity close to zero. The scattering tail can also be seen at the lower frequencies, and an extra component rising at 185 MHz towards the trailing edge.

4.3 Analysis and Results

4.3.1 Profile Evolution

Fig. 4.1 shows the time-averaged frequency structure of the pulse profile with phase, which also illustrates the frequency-dependent behaviour of the profile width and the pulse intensity. The profile width increases with decreasing frequency. Similar information is shown in Fig. 4.3, where average profiles of PSR J1820–0427 at multiple observing frequencies are shown. The x -axis shows time equivalent to one pulsar period (0.598s), where the peak of every averaged profile for each frequency is centred at the midpoint. The 200 MHz bandwidth of uGMRT data were divided into several subbands following the exercise in section 4.2. The Band 3 uGMRT data were divided into six equal subbands and data at Band 4 were divided into four equal subbands. As shown in Fig. 4.3, the average pulsar profile has a single sharp peak, with a scattering tail most pronounced at the lower frequencies. The excellent quality of the uGMRT data can also be seen clearly in each of the averaged profiles at frequencies from 317 to 725 MHz, where the off-pulse noise is negligible.

The pulsar profile at the MWA frequency band (170-200 MHz) shows a secondary feature near the trailing end of the profile, for which no counterparts are visible in the uGMRT bands. Past observations at higher frequencies (Kijak et al., 1998; Zhao et al., 2019) have reported a multi-component profile at frequencies above ~ 1.5 GHz; however, no such extra components are known at lower frequencies.

4.3.2 Pulse-to-pulse Variability

Fig. 4.4 shows the pulse train (a sequence of 400 pulses) at different frequencies across the uGMRT bands, where pulse-to-pulse variations can be readily observed. Amplitude fluctuations in pulsars can arise due to both intrinsic and extrinsic effects. While there seem to be multiple instances of large amplitude pulses, they do not fit the standard criteria of giant pulses, which require flux densities of tens or hundreds of times larger than the

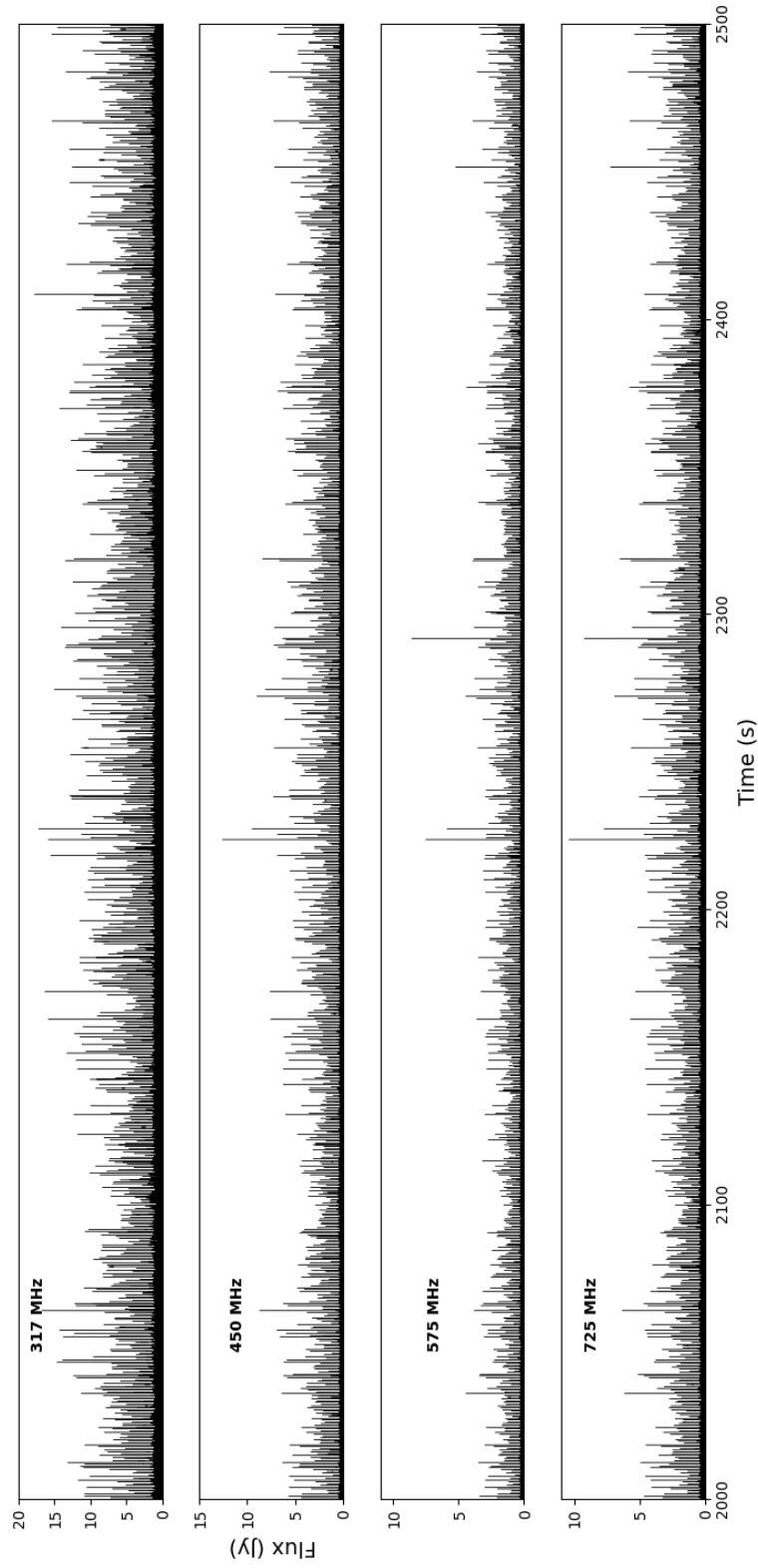


Figure 4.4: Calibrated single pulse train for PSR J1820–0427 at multiple observation frequencies for uGMRT Epoch 1. The high variability of single pulses can be seen, which decreases with higher frequency. A single high amplitude pulse also emerges at higher frequencies (around 2225s), showing a peculiar spectral index.

average pulsar flux. Moreover, in contrast with previous studies on nulling statistics (Biggs, 1992), which suggested a small nulling fraction of the order of $<1\%$ for this pulsar, our analysis does not reveal any instances of true nulls, despite having over 12000 pulses observed at multiple epochs and frequencies, with each pulse having a S/N of ~ 100 .

The fluctuations in pulse-to-pulse intensities can be quantified in terms of the modulation index, to further investigate the single pulse variability. Modulation Index (m) is defined as $-\sqrt{\langle \Delta I^2 \rangle} / \langle I \rangle$, where I is the pulse intensity, and the angle brackets represent averaging over a large ensemble of adjacent pulses and can be computed as a function of the pulse phase, ϕ . We found the modulation index for this pulsar to be close to 0.5, with variations along the on-pulse phase. This number is slightly higher than the minimum on-pulse, phase-resolved modulation index of ~ 0.34 calculated in Burke-Spolaor et al. (2012). In the observed frequency range of 300 to 750 MHz, the modulation index shows a maximum near the peak pulse phase and falls off at the tails.

Using the calibrated single pulse data, we further studied the spectral behaviour of individual pulses. We estimated the spectral index for each pulse using the flux density estimates at every two consecutive frequencies, following the relation -

$$\alpha(n) = \frac{\log[S_{\nu_1}(n)/S_{\nu_2}(n)]}{\log(\nu_1/\nu_2)} \quad (4.2)$$

where n is the pulse number, S_ν is the flux density at frequency ν , and α is the spectral index. Thus, an $\alpha(n)$ value was calculated for every pulse using the flux density at consecutive observed frequencies. The spectral index values obtained in this study were seen to vary drastically from pulse to pulse and over the consecutive frequency pairs. This will be discussed in detail in section 4.4.2.

4.3.3 Pulse Fluence Distribution

The investigation of pulse energy distribution provides insights into the radio pulsar emission mechanism and the physical state of the pulsar magnetosphere (e.g., Burke-Spolaor et al., 2012; Cairns et al., 2003c). Many of the observed phenomena, including

pulse-to-pulse variability (in pulse amplitude, structure, etc.), point to the fact that physical conditions in the magnetosphere tend to change on very short time scales, i.e., the pulsar emission process is inherently dynamic in nature. Observations such as the distribution of single pulse energies can provide a window to the instantaneous state of pulsar plasma and the nature of emission mechanisms that give rise to the observed distribution (e.g., [Burke-Spolaor et al., 2012](#)).

For the following exercise, we only used the calibrated uGMRT single pulse data. Single pulses at 185 MHz using MWA had low S/N and could not be used to study the pulse energy distribution using single pulse data. We visually determined the on-pulse region in each observation using the average profile. The on-pulse region was selected as the width at which the flux density drops to less than roughly 5% of the maximum flux density in the average profile. The on-pulse energy (E) was calculated for every single pulse by integrating the calibrated flux in the on-pulse region. The estimated pulse energy has units of mJy ms, i.e., pulse fluence. A histogram of pulse fluence was then constructed to study the distribution.

In Fig. 4.5, each panel shows the pulse fluence distribution of PSR J1820–0427 at different subband frequencies. It is evident that the pulse energies follow a log-normal distribution at all the observed frequencies. The log-normal distribution is the probability distribution of a random variable whose logarithm is normally distributed. We fitted a log-normal model to the observational data using a least-squares fitting method, defined using the parameters μ and σ :

$$N(E) = \frac{A}{E} \exp\left[-\frac{(\ln(E) - \mu)^2}{2\sigma^2}\right] \quad (4.3)$$

where E is the pulse fluence, A is the scaling factor, and $N(E)$ is the log normal distribution of fluence with parameters μ (mean) and σ (standard deviation). We found the log-normal pulse fluence distribution best describes our data and over the observed wide-frequency range and both epochs. A goodness-of-fit (GoF) was also calculated for each case to determine the quality of the fit. The parameter μ and σ , along with the GoF, are given in

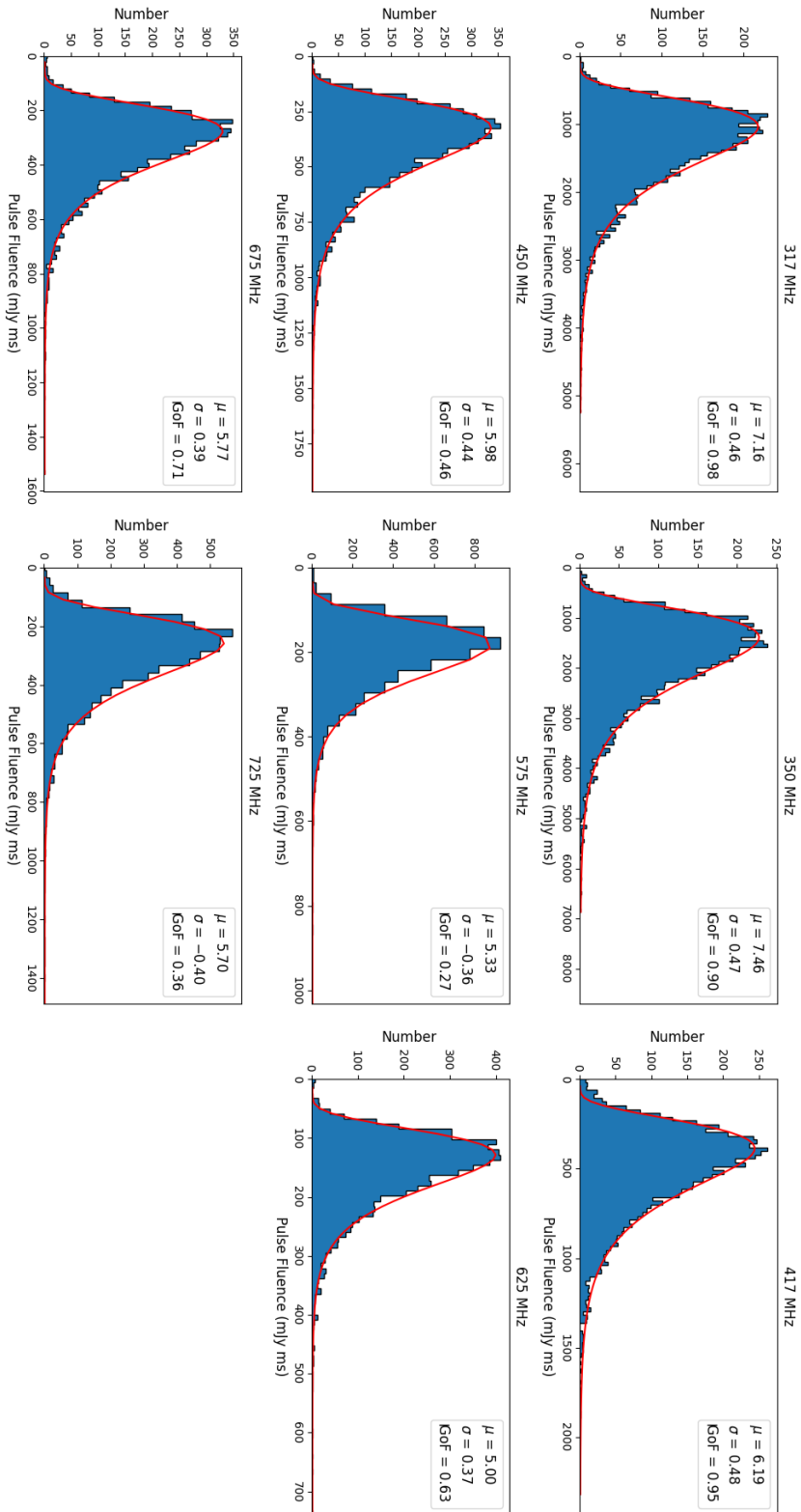


Figure 4.5: Pulse fluence histograms for uGMRT observations from Epoch 2. Each panel represents the pulse fluence distribution at a frequency mentioned at the top of each panel. In support of theories like the Stochastic Growth Theory (SGT), we found a log-normal distribution of pulse energies consistent at all frequencies. The histogram is fitted with a log-normal distribution shown as the red curve, with the parameters mentioned in the top right corner of each subplot.

Fig. 4.5.

Our study extends the findings of [Burke-Spolaor et al. \(2012\)](#) at 1.4 GHz to frequencies below ~ 1 GHz, spanning a wide-frequency range of 300-750 MHz, using a much larger sample size of over 12,000 pulses. Our analysis revealed that the emission process giving rise to the log-normal behaviour of pulse energies remains the same over a wide frequency range.

4.3.4 Flux density spectrum

The calibrated pulsar flux densities were calculated over a wide range of frequencies (170-750 MHz) by imaging the pulsar field (see Fig. 4.2), as listed in Table 4.1. It is possible that the flux density values at lower frequencies can be less reliable due to inherently larger source confusion at these frequencies and comparatively larger fields-of-view. As visible from the images in Fig. 4.2, the pulsar is in the vicinity of multiple sources, which may slightly bias the estimated flux densities at lower frequencies. Yet, even at 185 MHz, the pulsar is at least 6σ away from the closest source. Hence, the source is well separated from the close-by sources, thus providing a reliable flux density estimate.

We used the `pulsar_spectra`² repository ([Swainston et al., 2022b](#)), which is a fully-featured spectral fitting PYTHON software package. It also contains a catalogue of flux density measurements from several publications, which were used to collate all the flux density measurements of this source from this work and the existing literature. The resultant spectral fit of PSR J1820–0427 using all known flux densities is shown in Fig. 4.6. The spectral fitting procedure is based on [Jankowski et al. \(2018\)](#). To account for the uncertainties of the outlier points, a Huber loss function ([Huber, 1964](#)) is used instead of the least-squares quadratic loss function. The function deviates to a linear loss once a certain distance is reached from the model. The data are then fitted using different models like a power law, broken power law, log-parabolic, etc. The best-fit model is

²https://github.com/NickSwainston/pulsar_spectra

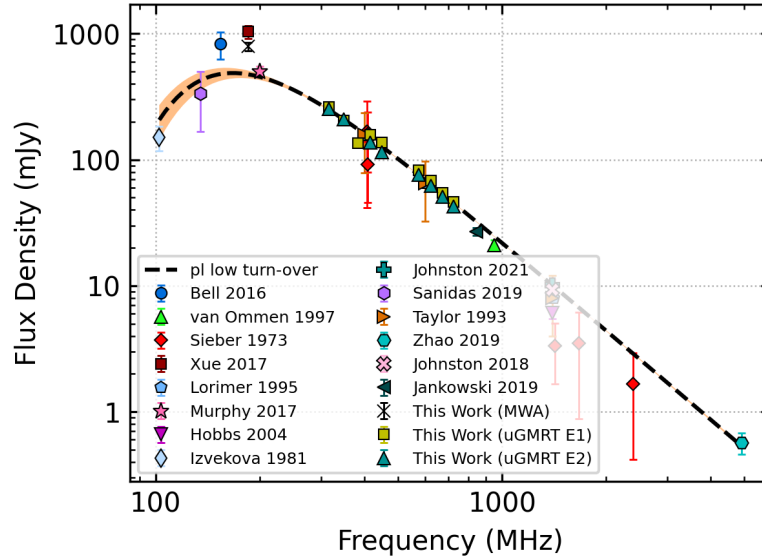


Figure 4.6: Spectral Index fit for PSR J1820–0427 using flux density values from this work along with the flux density values from the published literature. The black dashed line is the best-fitting model to the data, and the orange shaded envelope is the 1σ uncertainty of the best-fitting model. The turn-over frequency was found to be ~ 170 MHz, and the spectral index is -2.34 ± 0.01 . In contrast with the previous studies, the power law with a low-frequency turn-over (dashed line) fits the data best for this pulsar.

then determined using the Akaike information criterion (AIC, [Akaike \(1974\)](#)), which is a measure of information retained by the model without over-fitting.

In the published literature, PSR J1820–0427 is known to exhibit a broken power law ([Lee et al., 2022](#); [Murphy et al., 2017](#)). Fig. 4.6 combines 17 flux density measurements (multiple epochs) from this study with all other published values from the literature. Our analysis suggests a power-law function with a low-frequency turn-over to best describe the spectral behaviour of the pulsar, as shown by the black dashed line in Fig. 4.6. Here the one-sigma uncertainty on the model is given by the orange-shaded envelope. As per this model, the turn-over frequency is 169 ± 5 MHz, and the spectral index is -2.34 ± 0.01 . Given the spectral turnover of the pulsar, it is possible to reconcile that the single pulses at 185 MHz were not bright enough for a detailed single-pulse analysis.

4.3.5 Scatter Broadening

The pulse profiles in our observations show substantial scatter broadening of the pulsar, which may be expected given the moderate DM and proximity to the galactic longitude and latitude ($l \sim 25^\circ$, $b \sim 5^\circ$). For PSR J1820–0427, we are able to characterise the temporal broadening of the pulse caused by multi-path scattering and its frequency dependence, given the significant evolution across the observing band from ~ 170 MHz to ~ 750 MHz. As seen in Fig. 4.3, scattering is readily visible at the lower frequencies of the uGMRT and most pronounced at the low-frequency band of the MWA. As seen from Fig. 4.3, the pulse profile is minimally scattered at the higher frequencies, but the degree of scattering steadily increases at lower frequencies. Though the pulse profile looks relatively simple at the uGMRT bands, it clearly shows an additional feature in the pulsar profile at the MWA band. This is the first reported detection of this additional feature for J1820–0427.

The scattering of pulsar emission depends on fluctuations in the Inter-Stellar Medium (ISM) electron density and results in the broadening of pulse shape at lower frequencies. This pulse broadening is quantified by the timescale, τ_d , which is characteristic of a pulse broadening function (PBF) fitted to a measured pulse shape. The broadening time has a frequency dependence, given by $\tau_d \propto \nu^{-\beta}$, where the scaling index β depends on the details of scattering geometry and the nature of the turbulent medium. The PBF is the impulse response of the ISM to a signal approximated as a delta function. The exact form of the PBF associated with the ISM is generally unknown. It depends on the distribution and the turbulence power spectrum of the scattering material along the line of sight to the pulsar. Its frequency dependence is measured by the frequency scaling index, β , which is related to the underlying physics of turbulence and its power spectrum.

For the estimation of pulse broadening time, τ_d , we use the method developed in [Bhat et al. \(2004\)](#) and [Kirsten et al. \(2019\)](#). Consideration of this method can be justified given the emergence of a secondary hump-like feature at low frequencies, as revealed

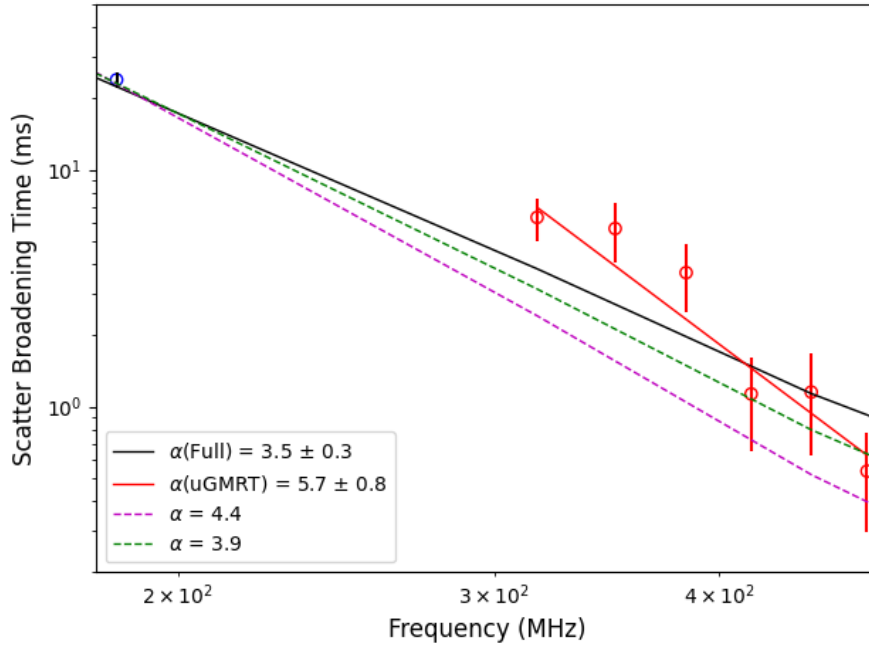


Figure 4.7: Measured scattering delay vs the observing frequency for PSR J1820–0427; using a thick screen model for scattering, as described in the text. The black line in the plot is a power-law fit of the form $\tau_d \propto \nu^{-\beta}$, to the complete observed data. The red line shows a fit to only uGMRT Band 3 data. The green dashed line shows the frequency scaling for Kolmogorov turbulence, and the blue dashed line is for the empirical index favoured by a large body of measurements as shown by [Bhat et al. \(2004\)](#).

in the MWA data. The method makes use of a CLEAN-based algorithm to deconvolve the interstellar pulse broadening from the measured pulse shapes. The CLEAN-based approach offers the benefit that no assumption needs to be made about the intrinsic pulse shape. However, it does involve (as with most other methods) trailing a range of PBFs and uses a set of parameters (i.e. figures of merit) to determine the best fit PBF. As demonstrated in [Bhat et al. \(2004\)](#) and [Kirsten et al. \(2019\)](#), in principle, can also be used to ascertain the shape of PBF that gives a better fit.

For PSR J1820–0427, an exponential PBF with a rounded shape (thick scattering screen) results in better-reconstructed profiles than the simple exponential that corresponds to an ideal thin screen model. [Williamson \(1973\)](#) showed that for a thick scattering screen,

the PBF during the rise time up until shortly after the peak of the emission is given by

$$PBF(t) = \left(\frac{\pi\tau_d}{4t^3}\right)^{1/2} \exp\left[-\frac{\pi^2\tau_d}{16t}\right] \quad (4.4)$$

Fig. 4.7 shows the measured scatter broadening times with observed frequencies with different power law fits. The fitting exercise was performed using the MWA data at 185 MHz and uGMRT Band 3 data from the first epoch of observations. The black line shows a power-law fit using the data at 185-500 MHz, with a frequency scaling index, $\beta \sim 3.5 \pm 0.3$. This is shallower than the theoretically expected value of $\beta = 4.4$ for a Kolmogorov-type turbulence (Rickett, 1990). The overall scaling index is much closer to, albeit lower, than the inferred frequency scaling index from a global fit using a large set of measurements ($\tau_d \propto \nu^{-3.9}$), as shown in Bhat et al. (2004). However, the scaling index, as constrained by uGMRT measurements alone (red line), is much steeper, with an estimated value of $\beta = 5.7 \pm 0.8$ for τ_d measurements across the 300-500 MHz range.

As evident from Fig. 4.7, the measured broadening time at the MWA frequency (185 MHz) is significantly below the expectation based on extrapolation from scaling suggested by uGMRT data. A plausible explanation is perhaps a truncated scattering screen (Cordes & Lazio, 2001), where truncation occurs at $\lesssim 300$ MHz. Such a scenario can give rise to truncated images and, hence, truncated PBFs, as the scattering angle is large enough for the rays from the screen's edges to reach the observer. An observational manifestation of this is a shallower scaling index below the break frequency, i.e. an anomalous frequency scaling as discussed by Cordes & Lazio (2001), however, it is hard to be conclusive given just a single low-frequency measurement, especially considering that our measured profiles are better fit by PBFs of a thick screen rather than that of a thin screen.

The reconstructed profile at the low-frequency band (185 MHz, MWA), as shown in Fig. 4.8 in red, reveals a secondary feature akin to post-cursor emission. The presence of the secondary feature can be easily reconciled given the measured pulse profile at 185 MHz (see Fig. 4.3) and is clearly not an artefact of analysis. However, its absence or

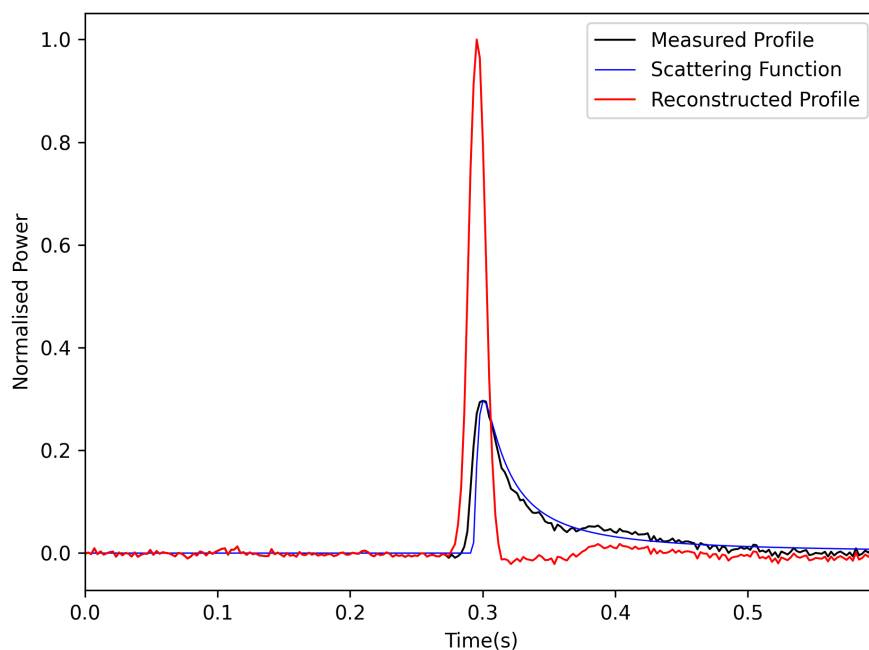


Figure 4.8: The measured pulse at 185 MHz using MWA is shown in black. The curve in blue shows the scattering function, which was chosen to be an exponential pulse broadening function with a rounded shape (thick scattering screen). The red curve is the reconstructed pulse profile and clearly shows a secondary feature emerging at the tail end, near time 0.4.

significantly reduced prominence at the higher frequency bands of uGMRT means either it has a much steeper spectrum than the main feature of the profile or a new feature that is visible at lower frequencies due to the specific beam/emission geometry of the pulsar. The latter may need a broader frequency coverage at low frequencies for detailed investigation (e.g. observations spanning a more extensive frequency range with the MWA).

4.3.6 Faraday Rotation

The polarimetric profiles of pulsars can be used to infer pulsar geometry (Rankin, 1983). The MWA observations were recorded with full polarisation; however, to get the polarimetric profiles of pulsars and estimate the degree of linear polarisation, we first need to correct the effect of Faraday Rotation (e.g., Taylor & Manchester, 1975). We used the

method described in Xue et al. (2019), which involves the application of rotation measure (RM) Synthesis technique to determine the rotation measure (RM, in units of rad m^{-2}) (Brentjens & de Bruyn, 2005; Burn, 1966; Heald et al., 2009). We extracted the Stokes parameters I , Q , U , and V as a function of frequency from the peak of the average total intensity pulse profile, using the pre-processing parts of the `rmfit` (Noutsos et al., 2008) function within the PSRCHIVE package. These Stokes parameters were then used as input to the RM Synthesis code ³. After correcting for the ionosphere contribution, we found the RM value of $69.5 \pm 0.2 \text{ rad m}^{-2}$. Johnston et al. (2007) noted a slightly lower RM of 67.5 rad m^{-2} for this pulsar using multiple frequencies from 0.69 to 3.1 GHz. The difference between the two values can be due to the change in the ionosphere and the local pulsar environment, considering the pulsar’s proximity to the Galactic centre. The difference in RM values can also be expected, given the time difference between observations and the pulsar space velocity.

4.4 Discussion

In this work, we have studied the pulse-to-pulse variability in single pulses using simultaneous wide-band observations made using uGMRT and MWA. The single pulses observed at multi-frequency uGMRT observations have an S/N of close to 100, making this pulsar a perfect source to study the wide-band single pulse behaviour. We employed a novel approach to calibrate the single pulses, using the flux densities estimated from the simultaneously recorded visibilities. In the following subsections, we discuss some of the results and implications of our studies.

4.4.1 Pulse Fluence Distribution

Single-pulse fluence distributions can be used as tools to test models of the pulsar emission mechanism. Most models generally predict these distributions to be Gaussian, log-normal,

³<https://github.com/gheald/RMtoolkit>

or power-law (Luo & Melrose, 1995; Weatherall, 1998). For our case, a log-normal distribution well describes the fluence distribution of PSR J1820–0427 over a wide range of observed frequencies.

Theories for wave growth in inhomogeneous media can be compared with pulsar observations. They can also be used to constrain the emission mechanisms and the potential source of these emissions. The Stochastic Growth Theory (SGT) (Robinson, 1992, 1995, 1997; Robinson et al., 1993) describes self-consistently interacting systems where the interactions occur in an independent homogeneous medium and introduce the relevant distance and time scales. This theory predicts a log-normal distribution of the observed single pulse energies.

Cairns et al. (2004) studied the phase-resolved single-pulse properties of slow-spinning pulsars PSR B0950+08 and PSR B1641–45, along with the Vela pulsar (Cairns et al., 2003a,b,c). Their investigation found that the pulsars showed log-normal fluence distributions over most of the pulse phase. They further reasoned that stochastic growth plays a pivotal role in producing pulsar emission, in which linear instabilities in inhomogeneous plasma generate the radio emission. The SGT also predicts a log-normal pulse fluence distribution seen in a broad population of pulsars, directly indicative of a changing SGT state (Wen et al., 2022). By interpreting the field statistics and the observed variability in a pure SGT, the associated pulsar emission mechanism is suggested to involve only linear processes. This implies that plasma instability in an SGT state either directly generates the radiation or else generates non-escaping waves that are transformed into escaping radiation by linear processes.

Burke-Spolaor et al. (2012) studied the pulse fluence distributions of 315 pulsars at 1.4 GHz, and found that a log-normal distribution adequately describes the fluence distribution for a majority of pulsars. They performed fluence distribution tests to assess the shape of the probability distribution function. In their study, PSR J1820–0427 was fit

by a log-normal distribution. Our analysis makes use of a much larger sample of single pulses, simultaneously observed at <1 GHz, a much wider frequency range and examines the frequency evolution of the distribution. Our results, therefore, extend their analysis with a log-normal pulse fluence distribution at a simultaneously observed wide frequency range from ~ 300 to 750 MHz. A direct consequence of the combined result from our study and [Burke-Spolaor et al. \(2012\)](#) is that the primary pulsar emission mechanism is similar within the observed ~ 1.5 GHz range.

Our analysis reveals a small number of large amplitude pulses. However, they cannot be considered as "giant pulses", which are typically ~ 2 - 3 orders of magnitude brighter than regular pulses ([Cordes et al., 2004](#)). The arrival of these strong pulses had no phase dependence. This may suggest that the emission mechanism for the strong pulses is not any different from those responsible for the emission of the regular (moderately bright) pulses.

4.4.2 Spectral Analysis

4.4.2.1 Mean Flux Density Spectrum

In general, pulsars are known to have a steep flux-density spectrum ([Sieber, 1973](#)) at frequencies above ~ 100 MHz. The study by [Lorimer et al. \(1995\)](#) published spectra of 280 pulsars from measurements at multiple frequencies between 0.4 and 1.6 GHz. The resulting analysis showed that the average spectral index for the pulsar sample was $\alpha = -1.6 \pm 0.3$. Another study ([Maron et al., 2000](#)) which extended the observed frequency range to 5 GHz, derived a mean value of $\alpha = -1.8 \pm 0.2$.

Some of the published literature ([Bell et al., 2016](#); [Zhao et al., 2019](#)) use a single power-law for the spectral behaviour of PSR J1820–0427. However, [Murphy et al. \(2017\)](#) suggested a broken power law to fit the pulsar spectra. The recent study by [Lee et al. \(2022\)](#), which spanned a similar frequency range, also suggested a broken power law with the break frequency at 200 MHz, where below the break frequency $\alpha_{low} = 1.73 \pm 0.03$ and

above 200 MHz $\alpha_{high} = -2.21 \pm 0.02$. However, in this study, we have combined 17 flux density data points obtained from measurements made with MWA (185 MHz) and uGMRT (300-750 MHz) at multiple epochs, with several others from the published literature. With the addition of new data, the flux density spectrum of PSR J1820–0427 now shows a low-frequency power-law turn-over (Fig. 4.6), much in contrast with previous results. The turn-over frequency with this model is 169 ± 5 MHz, and the spectral index is -2.34 ± 0.01 . The spectral index value obtained from our study is close to the value obtained in Lee et al. (2022), though only at high frequencies. Such low-frequency flux density measurements are crucial for constraining the spectral characteristics of pulsar emission at frequency ranges where the Square Kilometre Array (SKA-low) will be operational.

4.4.2.2 Pulse-to-pulse Variability

Single pulses from pulsars exhibit variabilities on multiple different time scales, and by examining these single pulses, we can constrain the pulsar emission mechanism. The intermittent behaviour of pulsars and the possibility of undetected populations raise questions about the presence of intermittent activity or emission variability in all pulsars and its impact on their evolution. For example, if the pulsar emission mechanism produces random intensity pulses, then one can expect a Gaussian distribution of pulse energies. However, any deviation from a Gaussian will point towards a non-random generation of intensities and hint toward a more complicated mechanism. Investigations of the individual pulses from slow pulsars revealed that their emission is quite erratic, especially compared to the stable average pulse profiles. Studying these variabilities is imperative in understanding the pulsar emission behaviour and propagation effects of the intervening plasma. In a recent study, Andaç et al. (2022) performed a 2-dimensional particle-in-cell simulation to investigate the plasmoid formation due to magnetic reconnection in the pulsar magnetosphere as a possible source of pulse-to-pulse variability. According to their study, the origin of strong subpulses is related to plasmoid formation in the magnetosphere. These

plasmoids produce bright, short subpulses, leading to a strong pulse-to-pulse variability. [Andaç et al. \(2022\)](#) also provides some predictions about the flux density distribution of single pulses, which can be applicable to single pulse studies. This kind of model, where bright subpulses are emitted due to the incoherent synchrotron radiation emitted in the pulsar wind current layer, can explain the high variability seen in pulsars like PSR J1820–0427.

Utilising the advantage of the wide observing bandwidth, we inspected the correlation between the pulse intensities at all observed frequencies with the highest observed frequency (725 MHz) using the calibrated single pulse flux densities. Fig. 4.9 shows scatter plots between observed flux at particular frequencies vs the reference flux at 725 MHz. The contours show lines of constant spectral index. Spread in the spectral index values implies that the physical process giving rise to single pulses is chaotic despite showing a global trend. We also found a peculiar behaviour of pulses at high flux densities, different from normal pulses. There appears to be an upward trend in all the subplots of Fig. 4.9, indicating a steeper spectrum for the high-intensity pulses with respect to higher frequencies. Current literature lacks reference to any such observed behaviour in J1820–0427 or any other pulsars.

Thus, an emission process which generates pulses of variable intensity, along with a mechanism which increases coherence with pulse intensity and frequency, may explain the erratic single pulse emission behaviour of PSR J1820–0427. Increased coherence can also imply a suitable change in the local environment. Since we observe the steepening at higher frequencies (see Fig. 4.9), implying lower emission heights (Radius to Frequency Mapping, [Cordes \(1978\)](#)), the coherence in brighter pulses could be due to the closer proximity of the emission region to the pulsar surface, where the magnetospheric conditions are generally different. While this category of pulses may likely make up the tail end of the log-normal pulse fluence distribution that is observed, our observations seem to suggest an additional, intermediate category of pulses (somewhere between “normal”

and “giant” pulses), which conform to large-amplitude single pulses seen in our data for PSR J1820–0427.

4.5 Summary

We have performed the first simultaneous multi-frequency single pulse analysis of PSR J1820–0427. In this work, we have used a high-quality data set from uGMRT at Band 3 (300-500 MHz) and Band 4 (550-750 MHz) and from MWA at 170-200 MHz. We estimated the flux densities using simultaneously recorded visibility data and used them to calibrate the single pulse data. Studies of single pulses can be insightful in understanding the pulsar emission process. The main findings from our analysis can be summarised below -

1. We devised a novel method to calibrate the single pulse beamformed data using simultaneously recorded visibility data. This calibration method was applied to the pulsar data from uGMRT at Band 3 (300-500 MHz) and Band 4 (550-750 MHz) obtained in the phased array mode.
2. We find that the single pulse fluences are best described using a log-normal distribution over a wide range of observed frequencies from 300 to 750 MHz. We further interpret our findings in terms of the Stochastic Growth Theory (SGT). Our results (at ~ 0.1 -1 GHz) are consistent with that from [Burke-Spolaor et al. \(2012\)](#) (at ~ 1 -2 GHz).
3. Using a rounded Pulse Broadening Function (PBF) corresponding to a thick scattering screen, for the measured pulse broadening time, we calculated a frequency scaling index, $\beta \sim 3.5 \pm 0.3$. The reconstructed profile at the low-frequency MWA band revealed a post-cursor type feature in the emission, for which no clear counterparts are seen at higher frequencies (300-750 MHz). Since this feature is absent at the higher frequencies, it may either have a much steeper spectrum than the main

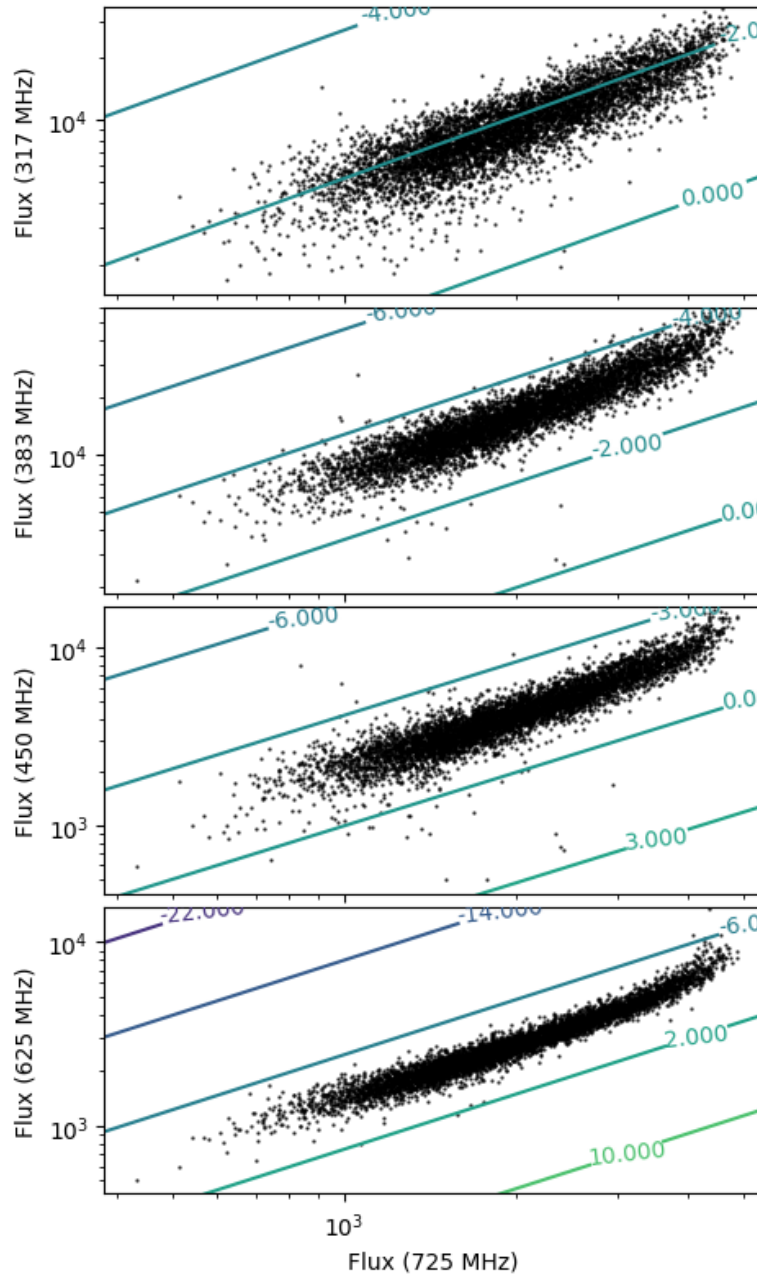


Figure 4.9: Flux vs flux plot between 725 MHz (x-axis) and other frequencies (y-axis). Contours show the lines of constant spectral index. The plot shows a tighter correlation between close frequency pairs. There also appears to be an upward trend for high-intensity pulses, indicating a steeper spectral index and a possibly different emission mechanism.

profile or alternatively, it is a feature that is visible at only lower frequencies (due to the specific beam/emission geometry of the pulsar).

4. Using our multi-frequency observations at a large frequency band (170-750 MHz), in conjunction with published literature, we find that the mean flux density spectrum of PSR J1820–0427 is best described using a power-law function with a low-frequency turnover, in contradiction to the previously thought broken power-law. With this model, the turn-over frequency is 169 ± 5 MHz, and the spectral index is -2.34 ± 0.01 .
5. We studied the pulse-to-pulse spectral index variation for PSR J1820–0427. The large scatter in the single pulse spectral index indicates a physical process less organised at short time scales.
6. Our analysis also indicates a steeper spectrum for high-intensity pulses, as compared to the regular pulses. This anomalous behaviour may point towards an emission mechanism where the coherence increases with intensity and frequency.

Overall, our work signifies the importance of high-sensitivity single pulse analysis over a wide frequency range to understand the intricacies of pulsar emission physics. Pulsars like J1820-0427, with their featureless profile, and no evidence of sub-pulse modulation such as nulling and drifting, are promising targets for detailed investigation of pulse fluence distributions and their frequency dependence. This is one of the less explored aspects of pulse-to-pulse variability, which can now be further investigated, thanks to the advent of uGMRT and its wide-band instrumentation. Other suitable targets include PSRs J0630–2834 and J1752–2806 which may allow extending the analysis down to the low frequencies of the MWA.

Our work also underscores the importance of low-frequency measurements from facilities such as the MWA, e.g., for refining the spectral behaviour of pulsar emission.

The emergence of an intriguing post-cursor type feature at low frequencies illustrates the utility of de-scattering techniques that do not involve the assumption of an intrinsic pulse shape. Analysis of this kind may allow us to explore the frequency evolution of average pulsar emission for pulsars where the profiles are substantially temporally broadened at $\lesssim 300$ MHz.

Chapter 5

Evolutionary subpulse drifting and nulling in PSR J0026–1955

“There’s something that doesn’t make sense. Let’s go and poke it with a stick.”

- The Doctor

This chapter is a faithful reproduction of *PSR J0026-1955: A curious case of evolutionary subpulse drifting and nulling* by [Janagal et al. \(2023\)](#).

Radio pulsars are rotating neutron stars with highly coherent radiation emanating from the vicinity of magnetic poles, which cross our line of sight once every pulsar rotation ([Hewish et al., 1968](#)). They possess a large mass (~ 1 to $\sim 2 M_{\odot}$) confined within a small radius ($\lesssim 10$ km), with strong gravitational ($\sim 10^{11}$ times stronger than the Earth’s surface gravitational field) and magnetic fields ($\sim 10^8$ to $\sim 10^{12}$ G; e.g., [Gold, 1969](#); [Lorimer & Kramer, 2004](#)). Pulsars are the sites of some of the highest energy physical processes, making them powerful astrophysical laboratories, owing to such extreme environments of very strong gravitational and magnetic fields surrounding them. However, even though more than 3000 pulsars are known to date, a definitive exposition of the processes by which pulsars emit beams of radio waves is still non-existent in the literature (e.g., [Melrose et al., 2020](#)).

Radio emission from pulsars exhibits a variety of phenomena, which modulate their pulse-to-pulse emission, observable in the form of subpulse drifting, nulling, mode changing, etc., thereby providing a range of avenues to understand the complex physical processes that cause the emission. In many cases, individual pulses from a pulsar show substructure with one or more distinct components called subpulses. [Drake & Craft \(1968\)](#) observed the systematic ‘marching’ of these subpulses with phase within the on-pulse window, leading to diagonal drifting structures in a pulse stack, called driftbands (pulse number vs rotation phase), as commonly seen in many pulsars (e.g., [Bhattacharyya et al., 2009](#); [Bilous, 2018](#); [Janagal et al., 2022](#); [McSweeney et al., 2017](#)). For such a pulse stack, the drift rate is then defined as the reciprocal of the slope of the driftbands ($^{\circ}/P_1$, where P_1 is the pulsar rotation period).

Theoretical models explaining subpulse drifting were suggested early on after the discovery of subpulse drifting in pulsars (e.g., [Ruderman & Sutherland, 1975](#); [Sturrock, 1971](#)). The most well-developed model at the time was able to explain the subpulse drifting phenomenon exhibited by pulsars studied then, most with stable drift rates, such as B0809+74 and B0943+10 (e.g., [Deshpande & Rankin, 1999](#); [Taylor et al., 1971](#)). The original model proposed by [Ruderman & Sutherland \(1975\)](#) associated drifting subpulses with a rotating ‘carousel’ of a discrete number of sparks (electrical discharges) in regions of charge depletion just above the neutron star surface near the magnetic poles. This carousel of sparks circulates around the magnetic axis due to an $\mathbf{E} \times \mathbf{B}$ drift and the electron-positron pairs produced in the discharges are ultimately responsible for the observed radio emission. The rotation rate of the carousel (P_4) around the magnetic axis is generally different from the pulsar period.

Two characteristic features of subpulse drifting pulsars are their drift rates and P_3 . The drift rate is defined as $D = \Delta\phi$ per pulse period ($^{\circ}/P_1$), where $\Delta\phi$ is the longitude shift in degrees during one pulse period P_1 . A positive value indicates a drift from early to later longitudes, while a negative value corresponds to a drift from later to earlier longitudes.

In a pulse stack, the vertical separation between driftbands at a given longitude is P_3 (typically expressed in units of the pulsar rotation period, P_1), which is a measure of time after which a subpulse will return at a particular phase. The caveat here is that the pulsar rotation only permits observation of the subpulse positions once every pulse. A specific subpulse in one pulse cannot be unambiguously identified in the next due to the difficulty in resolving the presence of aliasing, making it generally difficult to evaluate the true carousel speed. That is to say, if aliasing is present, the observed drift rate is related to the beating frequency between P_1 and P_4 . Another consequence of aliasing is that the drift rate can appear to vary even if P_4 stays constant as long as the beamlet configuration changes. Thus, if multiple drift rates are present in a given pulsar, it does not necessarily mean that the rotation speed of the carousel has changed; it may be that the number of beamlets has changed instead (e.g., [Janagal et al., 2022](#); [McSweeney et al., 2017](#); [Rankin et al., 2013](#)).

Even in the simplest case of a constant P_4 and a fixed number of beamlets, the apparent drift rate (i.e. the slope of the driftbands) is not a steady function of rotation longitude. This is a purely geometric phenomenon related to the projection of the beamlets' motion onto the line of sight trajectory, as explained in [Edwards & Stappers \(2002\)](#). This results in the driftbands themselves appearing curved, referred to as “geometric curvature”. Geometric curvature is always present but, similar to the polarisation position angle (PPA) of the rotating vector model ([Radhakrishnan & Cooke, 1969](#)), will only be visible if the pulse window is sufficiently wide for a given pulsar's particular viewing geometry. Geometric curvature is also similar to the PPA in that it is symmetric about the fiducial point, giving the driftbands a characteristic ‘S’-shape, with an excess (or deficit) of the drift rate appearing in the peripheral part of the pulse window.

The carousel model satisfactorily explains the subpulse drifting nature of some pulsars that show stable drift rates, citing the theoretical stability of electric and magnetic fields at the spark locations ([Ruderman & Sutherland, 1975](#)). Furthermore, multi-frequency

observations of a large fraction of the pulsar population have brought forth a variety of such atypical pulsars (e.g., [Song et al., 2023](#); [Weltevrede et al., 2007](#)). These studies show that a substantial fraction ($\sim 50\%$) of known pulsars exhibit subpulse drifting. However, explaining the drifting behaviour in pulsars that exhibit anything more complicated than a single stable drift rate requires modifications or extensions to the basic carousel model. Such pulsars present ideal test beds to modify the classical carousel model. Several extensions have been proposed over the years to account for the observed complicated behaviour. For example, [Gil & Sendyk \(2000\)](#) suggest that a quasi-central spark can account for the non-drifting core components in profiles. The well-known phenomenon of bi-drifting may be explained in terms of the presence of an inner annular gap ([Qiao et al., 2004](#)) or an inner acceleration gap ([Basu et al., 2019](#)), or non-circular spark motions ([Wright & Weltevrede, 2017](#)). Similarly, the phenomenon of drift rate reversal, shown by some pulsars, can be explained by the modified carousel model, where sparks rotate around the location of the electric potential extremum of the polar cap instead of the magnetic axis ([Szary et al., 2022](#)). These extensions/modifications are generally developed to explain specific drifting behaviours observed in a relatively small subset of subpulse drifting pulsars. However, there is still no comprehensive theory that can describe all the observed drifting behaviours.

Several theories have also been suggested to interpret the drifting subpulses geometrically. [Kazbegi et al. \(1991\)](#) and [Gogoberidze et al. \(2005\)](#) suggested that drifting subpulses result from modulation in the emission region caused by drift waves in some form of magnetospheric oscillations. In their model, the subpulses result from periodic variations in the magnetospheric plasma, which may cause the emission region to move across the observer's line of sight. [Clemens & Rosen \(2008\)](#) suggest that non-radial oscillations in the emission region could be responsible for subpulse drifting without invoking circulations in the magnetosphere. They propose that the drifting subpulses could be due to non-radial oscillations in the magnetosphere. Although these models are able to explain

phenomena such as mode changing, other phenomena, such as bi-drifting, memory across nulls, etc., cannot be convincingly accounted for.

Another phenomenon often seen in conjunction with subpulse drifting is ‘nulling’, where the emission from a pulsar ceases abruptly for a few to hundreds of pulse periods (Backer, 1970a) before it is restored. To date, pulse nulling has been reported in more than 200 pulsars (Wang et al., 2020), which is less than 10% of the known pulsar population. Nulls lasting for one or two pulses are generally attributed to the stochastic processes within the pulsar magnetosphere (e.g., Basu et al., 2018a). However, in subpulse drifting pulsars, short nulls can be attributed to a slight variation of the spark distribution, where nulls are caused by an empty line-of-sight (e.g., Janagal et al., 2022). Long nulls, on the other hand, are thought to be related to changes in the plasma processes within the pulsar magnetosphere (e.g., PSR B1706-16; Naidu et al., 2017), or even the spin-down energy loss in the most extreme cases (e.g., PSR B1931+24; Kramer et al., 2006). If nulls and changes in the drift modes are, in fact, caused by intrinsic changes in the pulsar magnetosphere, their interactions could be crucial in understanding the mechanisms behind changes between different magnetospheric states. Nulling itself may be an extreme form of mode-changing, where a pulsar switches between different magnetospheric states, as suggested by the broadband behaviour of three nulling pulsars reported by Gajjar et al. (2014). Hence, the study of pulsars exhibiting both nulling and drifting phenomena is crucial for comprehending the true origin and nature of the nulling phenomenon.

Pulsars which exhibit complicated drifting behaviour such as mode changing and nulling, and are also bright enough for single pulse analysis, are relatively rare. However, this combination is essential in shaping ideas concerning the pulsar radio emission process. Recently, the Murchison Widefield Array (MWA) independently discovered PSR J0026–1955 (McSweeney et al., 2022) in the shallow pass of their Southern-Sky MWA Rapid Two-metre (SMART) pulsar survey (Bhat et al., 2023a,b). The pulsar was originally detected in 2018 in the Green Bank Northern Celestial Cap (GBNCC) pulsar survey

(Stovall et al., 2014). However, the discovery was not followed up until the recent re-discovery by the MWA. J0026–1955 is a bright pulsar which has a period of 1.306150 s and a dispersion measure (DM) of 20.869 pc cm⁻³. The pulsar exhibits complex subpulse drifting behaviour and mode switching in addition to a large nulling fraction (~77% at 155 MHz). McSweeney et al. (2022) found two distinct subpulse drifting modes A and B, with slow and fast drift rates, respectively, which were further categorised (A1/A2 and B1/B2) depending upon the qualitative properties of modal appearances and context. The pulsar was sometimes seen to abruptly change its drift rate, while at other times, it exhibits a consistent evolution of the drift rate within its drifting modes.

The most distinctive feature of PSR J0026–1955 is its slow drift rate evolution, which has been found in only a handful of other pulsars like B0031-07 (Joshi & Vivekanand, 2000; McSweeney et al., 2017; Vivekanand & Joshi, 1997) and B0818-13 (Lyne & Ashworth, 1983). Furthermore, with its variable drift rates, the pulsar also poses an essential question to the stability of the carousel, as the basic models assume a stable configuration, leading to a non-variable drift rate throughout a drift mode. For J0026–1955, McSweeney et al. (2022) attempt to model the observed drifting behaviour with an exponentially decaying drift rate, similar to what is seen in PSR B0818-13 and PSR B0809+74 (Lyne & Ashworth, 1983). However, they were unable to fully characterise the observed drifting behaviour owing to their limited data sets and, consequently, an insufficient number of drift sequences. They also suggest a possibility of subpulse phase memory across short null sequences, which would benefit from more observations. Using longer multi-frequency observations, the modal taxonomy presented by McSweeney et al. (2022) can be tested for viability and to examine whether there is a need for something more sophisticated than an exponential model of drift rates. The complex drifting and nulling behaviour of this new pulsar thus warrants deeper investigations of its properties and their nature at different frequencies.

The unusual behaviour of J0026–1955 reported in McSweeney et al. (2022) will also benefit from a detailed study at higher frequencies, allowing us to test the frequency

dependence of such characteristics. Furthermore, given the slow period and large nulling fraction of the pulsar, long-duration observations with a higher signal-to-noise ratio (S/N) are necessary to collect a sufficiently large number of complete burst sequences in order to undertake a more robust statistical analysis.

In this study, we present a detailed investigation of subpulse drifting and nulling exhibited by J0026–1955, with new observations obtained using the upgraded Giant Metrewave Radio Telescope (uGMRT) at 300-500 MHz. This paper is organised as follows. In section 5.1, we briefly describe the observation details and data-reduction procedures; the subpulse drifting and nulling analysis are presented in section 5.2; our findings are discussed in section 5.3; and a summary of the paper is given in section 5.4.

5.1 Observations and Data Reduction

The Giant Metrewave Radio Telescope (GMRT) is a radio interferometric array consisting of 30 antennas, each with a 45-meter diameter, and spread over an area of 28 square kilometres in a Y-shape (Swarup et al., 1991). The GMRT recently underwent an upgrade, which included the addition of wide-band receivers and digital instrumentation, allowing for near-seamless coverage in frequency from 120 MHz to 1600 MHz (Gupta et al., 2017; Reddy et al., 2017). For our observations of PSR J0026–1955, we used the upgraded GMRT in the phased array mode, where signals from each antenna are coherently added for maximum sensitivity. J0026–1955 was observed with the uGMRT at Band 3 (300-500 MHz) and Band 4 (550-750 MHz), over two epochs at each frequency band. However, due to the presence of higher levels of radio frequency interference (RFI), Band 4 data quality was not adequate for meaningful single-pulse analysis. Thus for the work presented in this paper, we limit our analysis to Band 3 (300-500 MHz) data. Details of observations, including the number of pulses which had pulsar emission (burst) and lacked any emission (null), are summarised in Table 4.1.

MJD	Scan	Length	Number of Pulses	
		(minutes)	Burst	Null
59529	1	54	1825	669
	2	43	735	1234
	3	54	781	1717
59543	1	54	971	1506
	2	54	642	1841
	3	54	1315	1151
Total			6269	8118

All observations are in the 300-500 MHz band, with $655.56\mu\text{s}$ time resolution, spread over 2048 channels.

Table 5.1: Table of observations for PSR J0026–1955.

The data were recorded at $655.56\mu\text{s}$ time resolution, spread across 2048 channels, thus providing a frequency resolution of 97.65 kHz, and were converted to single-pulse archives using the DSPSR package (van Straten & Bailes, 2011). The single pulse files were then frequency scrunched and combined using the routines from PSRCHIVE (Hotan et al., 2004). Finally, each frequency-scrunched single-pulse sequence file was manually searched for RFI using the interactive RFI zapping subroutine `pazi` of PSRCHIVE. The RFI-excised file was then converted into an ASCII format that contained the pulse time series and was used for all subsequent analyses.

Following the methodology detailed above, the pulsar time series data obtained in the last step were used to generate the pulse stacks (pulse phase vs pulse number) as shown in Fig. 5.1. The bright yellow diagonally arranged pixels between pulse phase -20° and $+20^\circ$ are the subpulse driftbands, which can be clearly seen to march from a positive to a negative phase, with increasing pulse number. Despite multiple rounds of RFI excision using the `pazi` subroutine, it is evident from Fig. 5.1 that there is some residual RFI. For example, several seconds of RFI can be seen right before pulse number 850 in panel (a). However, cases where the subpulses are bright enough to be visually recognised (despite the RFI), were retained. With such a tradeoff, we were able to salvage data that could still

be used for exploration without affecting the subpulse drifting analysis. Further, panels (c) and (d), provide clear examples of short and long nulls, where any emission from the pulsar is absent for a certain duration ranging from a few to a few hundred pulses. Table 5.1 presents a comprehensive summary of nulls and bursts observed in different observations.

5.2 Analysis

In subsequent analysis, we elaborate on different subpulse behaviours and attempt to characterise the drifting nature to learn the underlying mechanism in the context of the carousel model (Ruderman & Sutherland, 1975).

In general, the preliminary analysis of any subpulse drifting pulsar aims at the classification of drift modes. However, considering that J0026–1955 does not always exhibit well-defined discrete modes but rather a drift rate evolution, such an analysis is complicated. In section 5.2.1, we discuss a drift rate evolution-based classification scheme for deciding the mode boundaries, using linear and exponential models for drift rate evolution. Section 5.2.2 discusses the modes identified using this scheme. The observed nulling behaviour of the pulsar at 400 MHz is discussed in section 5.2.3. Further, the evolutionary drift rate behaviour of the pulsar is studied in detail in section 5.2.4. The exponential drift rate model used in section 5.2.1 was employed by Lyne & Ashworth (1983) to demonstrate memory across nulls for the first time. Following their lead, we have also examined J0026–1955 for possible instances of memory across nulls, detailed in section 5.2.5.

5.2.1 Drift Mode Boundaries

PSR J0026–1955 poses a unique challenge for identifying the drift modes. Generally, subpulse-drifting pulsars exhibit stable modes, which can be uniquely characterised by their P_3 values. However, the slowly evolving drift rates and P_3 of J0026–1955 complicate the mode identification. Thus, to identify the drift modes, we employed a different strategy.

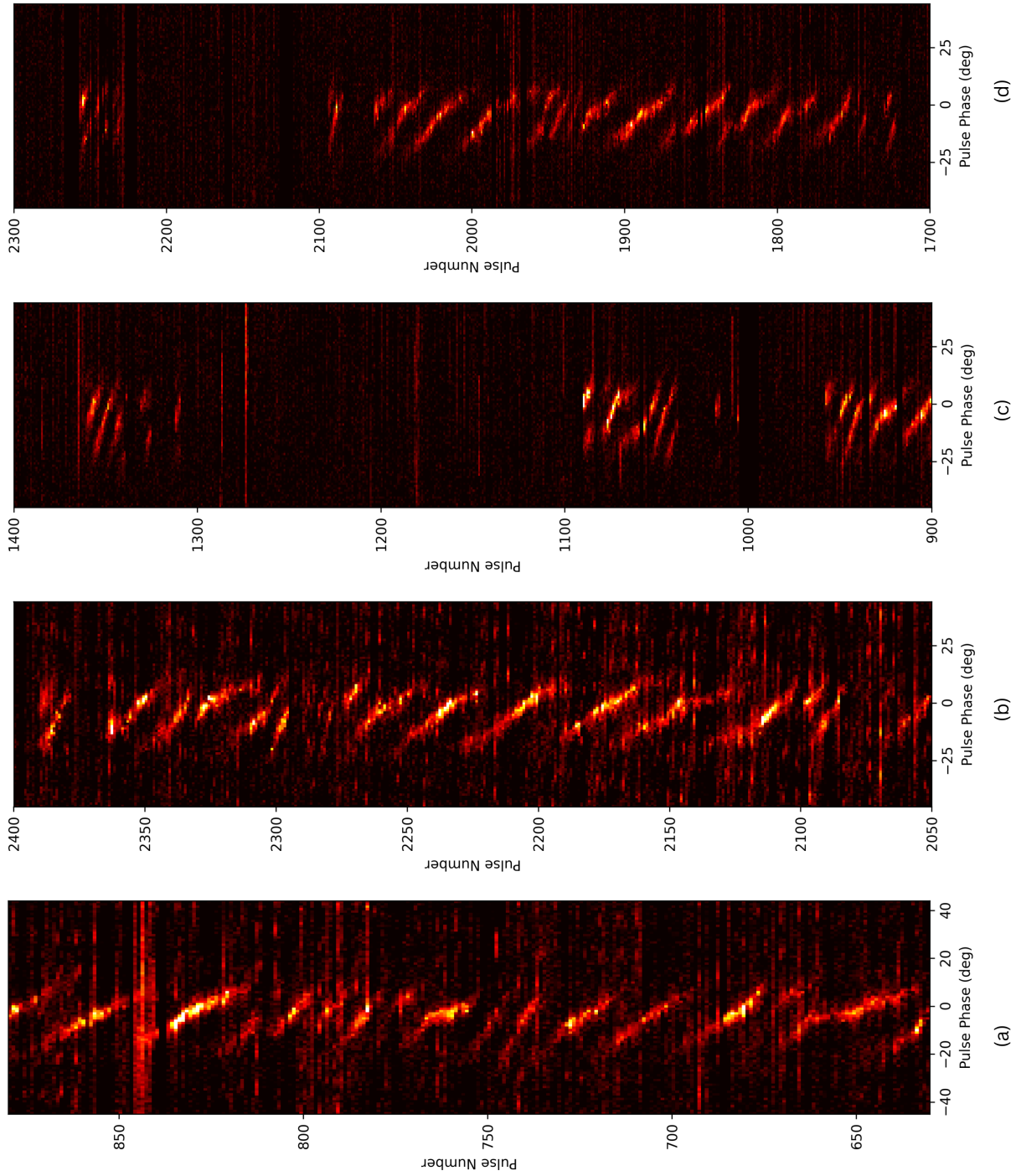


Figure 5.1: Each pulse stack (Pulse phase vs Pulse number) represents the variety of subpulse drifting sequences shown by PSR J0026–1955 at 400 MHz (using uGMRT). Bright yellow diagonally arranged pixels around to phase 0° are the drift bands. The pulsar exhibits both short and long nulls, where no emission can be seen in the on-pulse region.

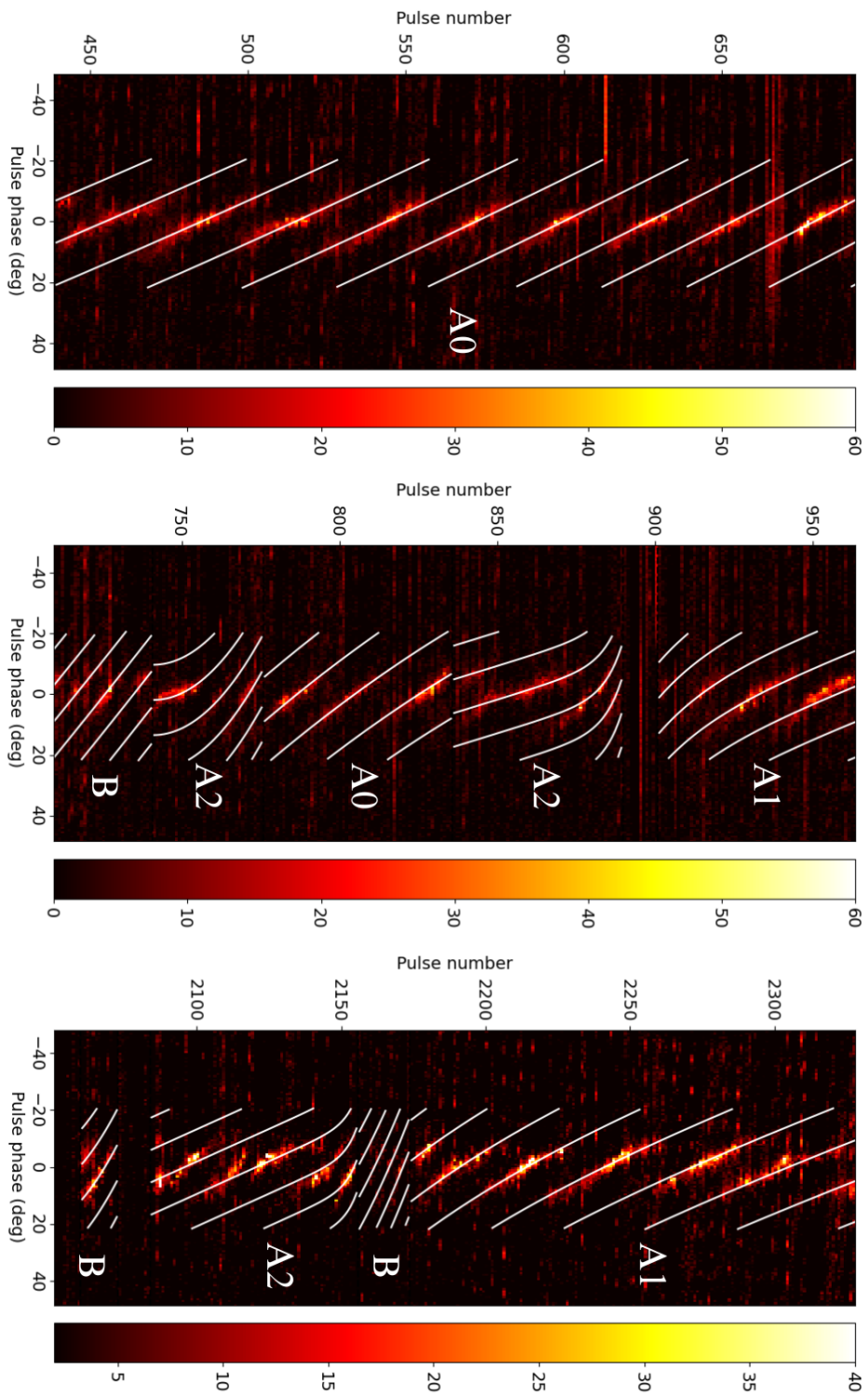


Figure 5.2: Pulse stack with drift bands (yellow bright subpulses) modelled using linear and exponential models (white lines). The evolution of drift rates can be seen in modes A1 and A2. The inter-modal drift band connectivity is also apparent in most cases.

Given that the pulsar exhibits both evolutionary and non-evolutionary drift rates, we modelled the drift rate behaviours to make a drift rate-based modal classification, which also accounts for the evolution. The linear model is the most straightforward generalisation of a constant drift rate, essentially including the next term in the Taylor expansion – and valid in situations where the drift sequences are sufficiently short relative to the rate of evolution. Further, to account for the drift rate evolution across individual driftbands (which can show significant curvature), we follow the lead of [Lyne & Ashworth \(1983\)](#) to use an exponential model. Hence, we used the linear model for non-evolving drift rates and an exponential model for evolutionary drift rates. To account for both kinds of drift rate behaviour, we used the following two models:

1. *Linear model of drift rates* ([McSweeney et al., 2017](#))

This model assumes a linearly evolving drift rate (D) with respect to increasing pulse number. Thus, devising an equation which depends linearly on pulse number (p) since the onset of the drift sequence, we get

$$D = \frac{d\phi}{dp} = a_1 p + a_2 \quad (5.1)$$

where a_1 and a_2 are constants, and ϕ is the pulse phase. We can integrate eqn. 5.1 to get the dependence of pulse phase on pulse number, which would be a quadratic relationship.

$$\phi(p) = a_1 p^2 + a_2 p + C \quad (5.2)$$

Here, $C = P_2 d + \phi_0$ is the integration constant that can be associated with a physical parameter, P_2 , which is the “horizontal” separation between drift bands and is assumed to be a constant for the model fit of each drift sequence. Here, ϕ_0 is an initial reference phase and can be defined as the phase at which the zeroth drift band crosses the zeroth pulse in a given sequence. Thus, the model has four free parameters, a_1 , a_2 , ϕ_0 , and P_2 , to be accounted for.

2. Exponential model of drift rates (McSweeney et al., 2022)

For the cases where individual drift bands can show significant curvature, the exponential model can be a better fit. In this model, the drift bands are modelled with an exponential function which assumes an exponential decay rate for the drift rate, D

$$D = \frac{d\phi}{dp} = D_0 e^{-p/\tau_r} + D_f \quad (5.3)$$

where D_f is the asymptotic drift rate, D_0 is the difference between D_f and the drift rate at the beginning of the drift sequence, p is the number of pulses since the onset of the drift sequence, and τ_r is the drift rate relaxation time (in units of the rotation period). To get the relationship with ϕ and p , we integrate eqn. 5.3

$$\phi = \tau_r D_0 \left(1 - e^{-p/\tau_r}\right) + D_f p + (\phi_0 + P_2 d) \quad (5.4)$$

where ϕ is the phase of a sub-pulse; ϕ_0 is an initial reference phase; d is the (integer) drift band number; and P_2 is the longitudinal spacing between successive drift bands. Thus, the model has five free parameters, D_0 , D_f , τ_r , ϕ_0 , and P_2 , of which the expression $\phi_0 + P_2 d$ defines the pulse phase at $p = 0$. The last term in eqn. 5.4 is the same as the constant in eqn. 5.2.

Using eqn. 5.2 and 5.4 from the linear and exponential drift rate models, we employed either of the two on different mode sequences. The fitting procedure for either of the models was carried out following the method described in McSweeney et al. (2022).

The pulsar exhibits both stable subpulse drifting (no evolution) and evolutionary drifting. Therefore, firstly we determined the mode boundaries (the beginning and end of a drift sequence) by visually inspecting the drift rate evolution in the pulse stack. Then, the evolutionary and non-evolutionary drift sequences were separated, with the caution that not too many mode boundaries are made. Sub-pulses were first smoothed using a

Gaussian kernel of width ~ 3.6 ms (i.e. 1° of pulsar rotation, the approximate width of a subpulse). Then, the subpulses in each drifting sequence were identified by determining the peaks above a certain flux density threshold. This threshold was chosen such that for a minimum pixel value, no sub-pulse is identified in the off-pulse region. Each sub-pulse in the drift sequence is then assigned a driftband number. Finally, depending upon the drift rate model of choice, the driftbands are fitted (using SciPy's `curve_fit` method) with the functional form of the sub-pulse phases as mentioned in eqn. 5.2 and 5.4. Examples of drift rate fitting are shown in Fig. 5.2, where the bright diagonally arranged patterns are the driftbands and the white overlaid lines are the driftband fits. The drift rate evolution across an entire observation (scan 2 of observation made on MJD 59529) using the above methodology is shown in Fig. 5.3. Here the x -axis shows the pulse number, and the y -axis shows the drift rate in $^\circ/P_1$ units. The different curves correspond to either a linear or an exponentially varying drift rate across a drift sequence.

The models described above do not take into account the geometric curvature that must be present (to some degree), as discussed earlier. However, we argue that the geometric curvature must be negligible in J0026–1955's pulse window. As seen in Fig. 5.1 (and Fig. 5.2), the pulsar exhibits a variety of drifting modes with inconsistent drift rates. If the geometric curvature was significant across the pulse window, it should be visible in all the modes despite their evolutionary and non-evolutionary features. The fact that the characteristic 'S'-shape of geometric curvature is not visible throughout leads us to conclude that it must be negligible across the pulse window for this pulsar. We, therefore, do not attempt to include geometric curvature in our models. In the next subsection, we describe the drifting modes and their various sub-classes, among which is a non-evolutionary mode (A0), in which the driftbands appear straight (see the left panel of Fig. 5.2). This mode demonstrates the lack of a significant presence of geometric curvature.

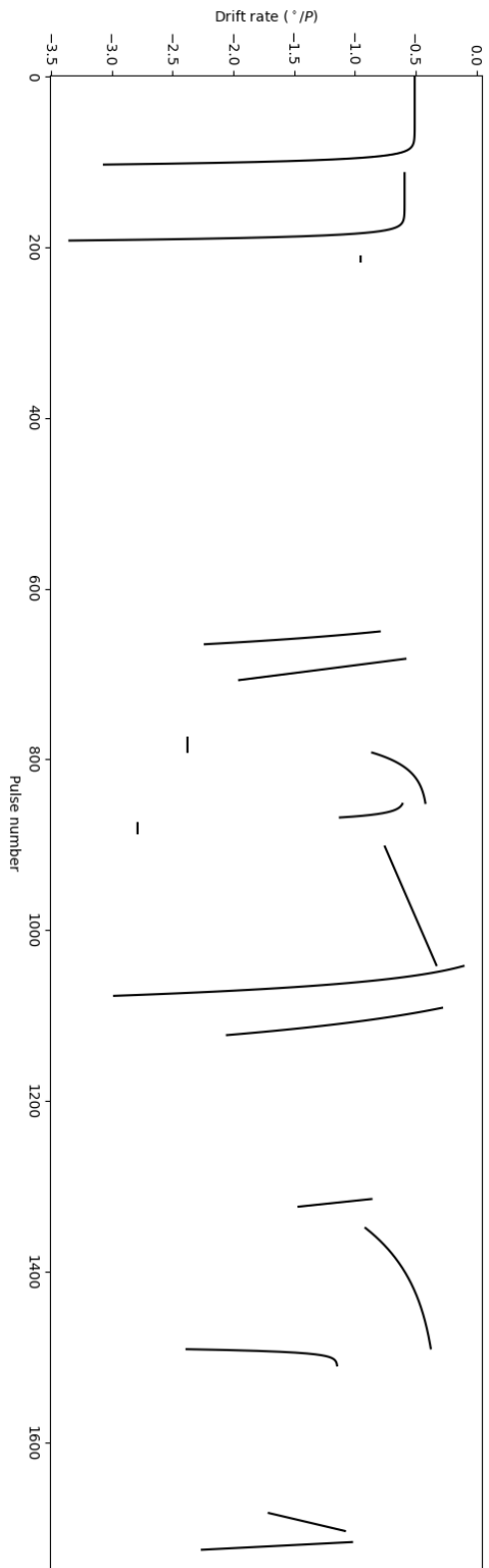


Figure 5.3: For the MJD 59529 scan 2 observation of J0026–1955, the above plot shows the drift rates as obtained using the linear and exponential drift rate models discussed in section 5.2.1. Some of the corresponding drift band fits are shown in Fig. 5.2.

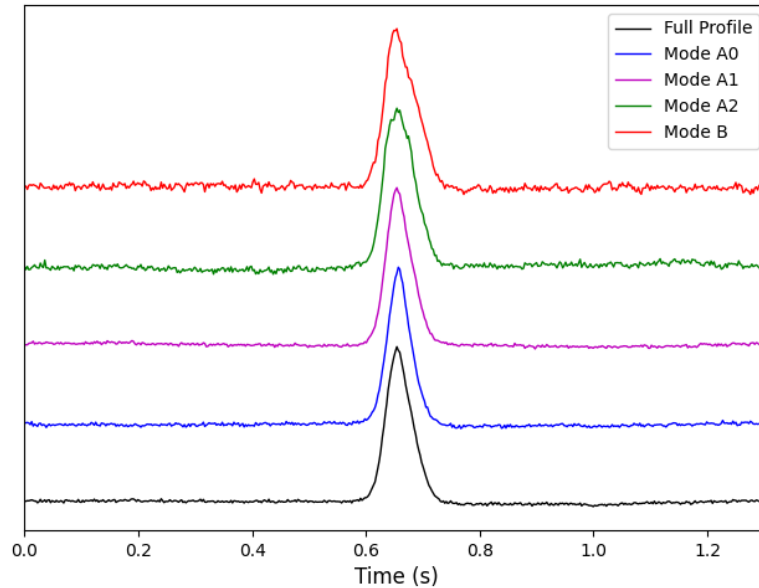


Figure 5.4: Average modal profiles of subpulse drifting modes exhibited by J0026–1955. Note that the average profiles of modes A0 and A1 are very similar. However, for modes A2 and B, the profiles are comparatively wider.

5.2.2 Drift Mode Classification

McSweeney et al. (2022) categorised the drifting behaviour into two different classes: A and B. They further made sub-categories of modes A and B depending on the qualitative properties of drift sequences, their appearance and context. In this work, the broad classification into modes A and B follows McSweeney et al. (2022), but our subcategories of these modes are completely different and are based on the drift rate modulation instead of organisation in drifting patterns. In our analysis, we first modelled the drift rates exhibited by the pulsar and then categorised them. The drift rate modelling provided insight into the drifting behaviour, which was the basis for our mode classification, as described below.

1. **Mode A:** Mode A is classified as an umbrella mode category which encompasses the slower drift rates. The pulsar in mode A exhibits organised as well as unorganised

driftbands. All of the evolutionary subpulse drifting behaviour exhibited by the pulsar can also be sub-categorised under mode A.

- (a) *Mode A0*: This is the non-evolutionary sub-category of mode A. These are mode sequences which possess an almost constant drift rate and do not exhibit any evolutionary behaviour, as shown in Fig. 5.2. Along with a stable drifting rate ($\sim -0.6^\circ/P_1$), mode A0 also has the largest mode length. The sequences, at times, do show frequent interruptions and rapid but temporary deviations in the drift rate. However, the overall drift rate still hovers around a constant number. The occurrence fraction of mode A0 in the complete set of observations was about 12%.
- (b) *Mode A1*: According to our drift rate classification, sequences which demonstrate a slow evolution from fast to slow drift rates, as shown in Fig. 5.2, are labelled as mode A1. In an extreme case of drift rate evolution in mode A1, the sequence begins with a small P_3 value of about $16P_1$ and ends after 110 pulses with a much different P_3 of about $60P_1$. Mode A1 also had the largest occurrence fraction of $\sim 17\%$ among all the subpulse drifting modes.
- (c) *Mode A2*: In addition to the evolution from faster to slower drift rates, the pulsar also exhibits the opposite evolutionary behaviour. Mode A2 sequences begin with a slow drift rate, where the driftbands are far apart and evolve towards a faster drift rate. In our data, mode A2 had a total occurrence fraction of $\sim 7\%$. The sequences in mode A2 are generally short-lived and consist of 3-4 driftbands before the sequence ends with a faster drift rate (see fig. 5.2). We also note that most occurrences of mode A2 are followed by a null. This possible correlation is discussed in detail in section 5.3.2. [McSweeney et al. \(2022\)](#) assumed this mode as a combination of mode A and the faster drifting mode (mode B). However, we believe that this is yet another evolutionary mode of J0026–1955, as the driftbands are fully connected throughout the

drift sequence and exhibit a slow evolution rather than a sudden change in drift rate.

As expected, from Fig. 5.4, it can be seen that the modal profiles of all the sub-categories of mode A show similar features despite the dissimilar drift rate behaviour, lending credibility to our classification scheme.

2. **Mode B:** The pulsar also exhibits a faster drift rate on its own without being a part of any evolutionary behaviour. This was present in only $\sim 4\%$ of the total observation. Mode B sequences are short-lived, are generally isolated occurrences, and do not show a drift rate evolution, as shown in Fig. 5.2. Mode B sequences can be found anywhere in the pulse stack, even in the midst of long, otherwise uninterrupted null sequences. The average drift rate for mode B is $\sim -1.6^\circ/P_1$. The average modal profile of mode B is shown in Fig. 5.4, which shows slightly different features with a skewed average profile, as compared to mode A profiles.

An additional feature was sometimes noted in the drift sequences of J0026–1955, where an extra driftband seems to appear towards the leading edge. An example can be seen at around pulse number 2125 in panel (c) of Fig. 5.2, in mode A2. There is a sudden break in the middle of the driftband, and both pieces look disassociated. It appears that towards the end of the first driftband, the drift rate fastens, and for the second driftband, the drift rate begins at a faster rate and then slows down. Overall, if the sudden drift rate change and the break are ignored, they seem to form a full driftband. During our analysis, we have not accounted for the break and considered the driftband in full wherever such a deviation was noted.

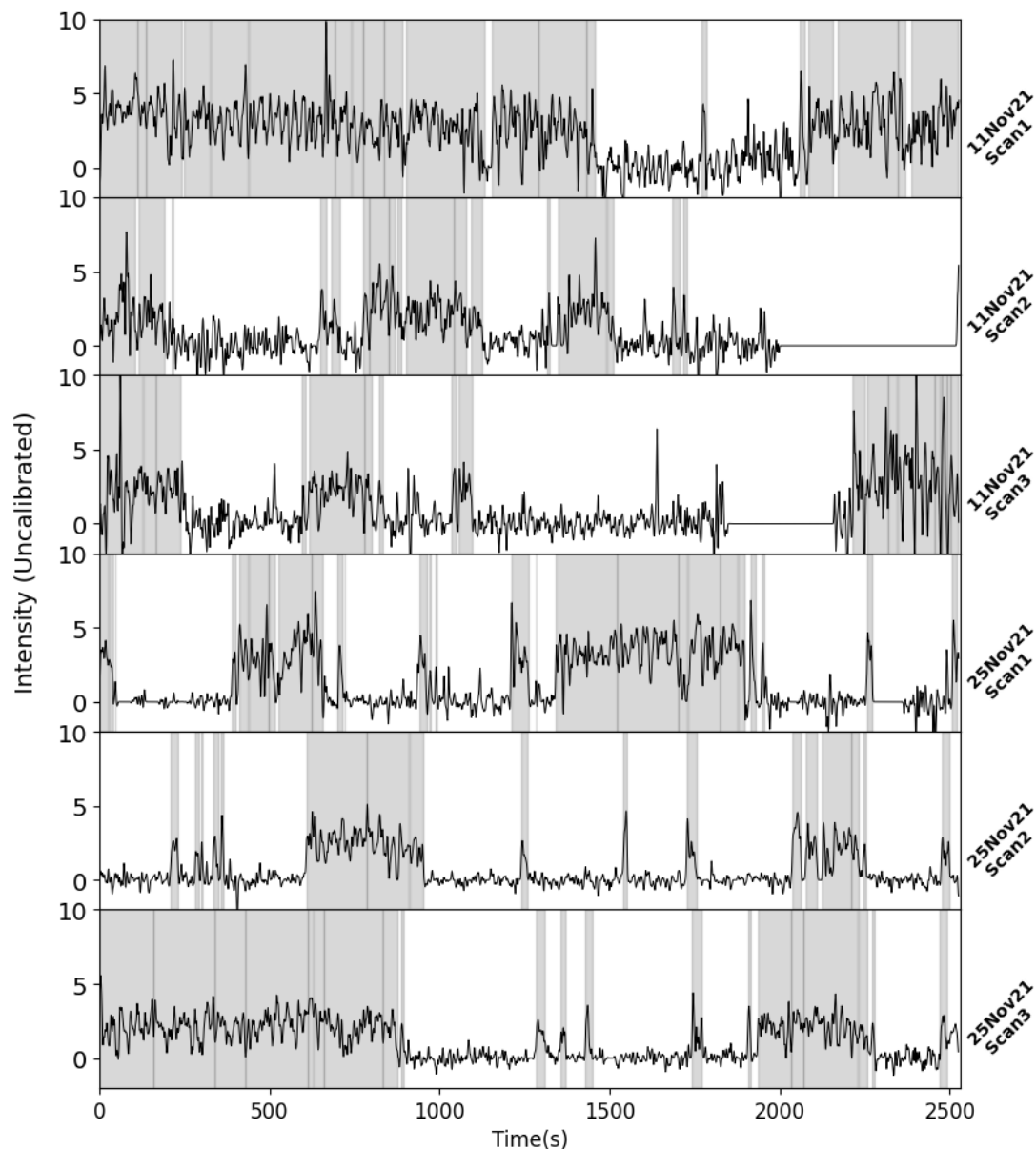


Figure 5.5: Peak flux density within the on-pulse window as a function of time for the six uGMRT observations at 400 MHz. The shaded grey regions show detected subpulses. The unshaded region corresponds to nulls and RFI occurrences. The peak fluxes were measured after smoothing the time series with a Gaussian filter (1σ) to suppress the noise contribution and accentuate the contrast between nulling and burst sequences.

5.2.3 Nulling

Nulling is the temporary disappearance of emission from a pulsar for brief periods of time. After deciding the mode boundaries using the method described in 5.2.2, sequences with no subpulse detection were counted as nulls. In our observations, PSR J0026–1955 showed evidence of both long bursts of pulses and long nulls. The long nulls are sometimes interrupted with short mode B sequences. Fig. 5.5 shows the entire length of null and burst sequences in all our observation scans. The longest null sequence goes on for 1117 pulses (~ 25 minutes). In contrast, the most prolonged burst in our observations lasts for 867 pulses (~ 19 minutes).

Fig. 5.5 shows intensity as a function of time for all the observations. The shaded grey regions show detected subpulses, and the rest are nulls. The degree of nulling in a pulsar can be quantified in terms of the nulling fraction (NF), which is the fraction of pulses with no detectable emission. Overall, J0026–1955 was in a null state for more than half of our observations, with an estimated total nulling fraction of $\sim 58\%$. This differs from the nulling fraction of $\sim 77\%$ obtained at 155 MHz using the MWA (McSweeney et al., 2022). This discrepancy and the nulling behaviour of J0026–1955 are discussed in detail in section 5.3.1.

5.2.4 Drift Rate Evolution

PSR J0026–1955 exhibits multiple drift rates and evolutionary features throughout the drift sequences and individual driftbands. Initially, we used the linear and exponential models to understand the drift rate behaviour within a sequence, as described in section 5.2.1. However, driftbands and sequences in J0026–1955 exhibit more complicated evolutionary features, as seen in the mode A1 and A2 occurrences in Fig. 5.2, where even an exponential model fails to accurately describe the evolutionary drift rates correctly.

We further explored the drift rate behaviour of J0026–1955 by studying the variation

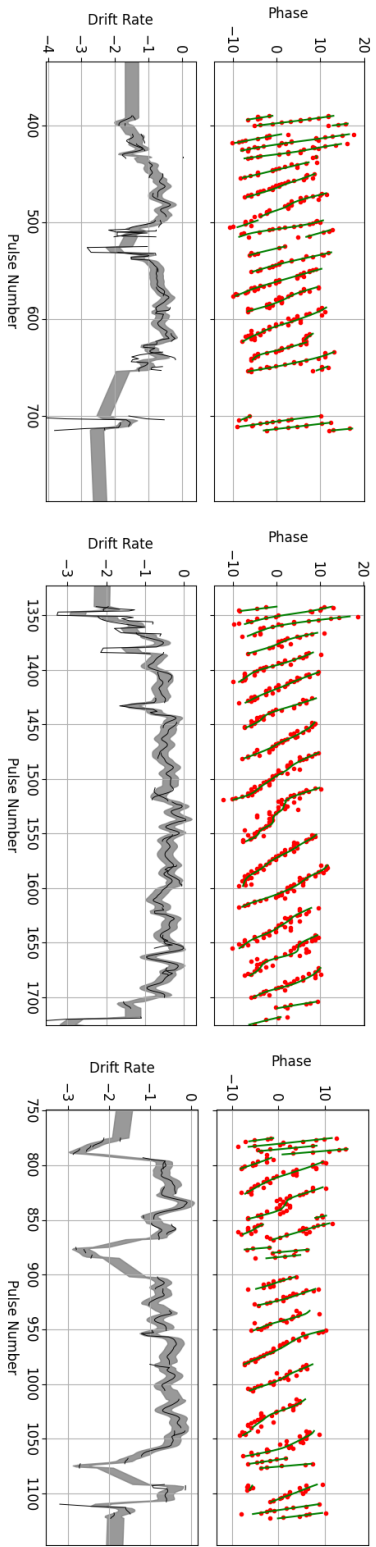


Figure 5.6: In the top panels of all sub-figures, the red dots show the location of subpulses, while the green lines correspond to fits to drift bands using a cubic smoothing spline method. In the lower panels, the black solid lines show the drift rates ($^{\circ}/P_1$) of individual drift bands, while the solid grey line shows the average drift rate. The figures represent only a few drift sequences.

in drift rate with each pulse in a driftband. To calculate the evolution of the drift rate with each pulse, we followed the methodology described in Szary et al. (2022). We first employed a cubic smoothing spline estimate using the *SmoothingSplines*¹ software package on each of the driftbands, irrespective of their mode identity or drift mode boundaries. Then, we obtained the drift rate (phase/pulse number) by calculating the gradient of the fitted spline function at every pulse number for each driftband. As seen in J0026–1955 pulse stacks, there can be two driftbands at a given pulse number. Fig. 5.6 shows examples of some drift sequences, where the top panel shows part of the pulse stack, where the red dots indicate the location of subpulses. Here, the green line is the cubic spline fit, which was obtained with the smoothing parameter $\lambda = 100$. In the bottom panel of Fig. 5.6, the black lines show the gradient calculated at each pulse number for every driftband. As some pulses contain two subpulses, yielding two measurements of the drift rate for that pulse number, we estimate multiple drift rates at some of the pulse numbers. The solid grey envelope shows the mean drift rate at every pulse number where the contribution from multiple driftbands at any given pulse is averaged.

A subset of pulsars that exhibit multiple subpulse drifting modes shows a harmonic relationship between P_3 , as reported in previous studies (McSweeney et al., 2019; Rankin et al., 2013). In the case of J0026–1955, a similar analysis with drift rates leads to interesting implications. A cumulative and modal histogram of individual drift rates obtained by taking a gradient of the smoothing spline fit of driftbands at each pulse number can be seen in Fig. 5.7. The top panel shows a distribution of all drift rates, where each colour corresponds to the different modes classified for J0026–1955. The lower panels of Fig. 5.7 display the distribution of drift rates for all observed subpulse drifting modes of J0026–1955. Apart from two distinct drift rate peaks at approximately $-0.5^\circ/P_1$ and $-1.6^\circ/P_1$, a third peak is visible at around $-2.7^\circ/P_1$. The peak values of the drift rates form an arithmetic sequence with a common difference of approximately $-1.1^\circ/P_1$.

¹<https://github.com/nignatiadis/SmoothingSplines.jl>

Further, considering eqn. 1 and 2 in [McSweeney et al. \(2019\)](#), it can be implied that if an arithmetic spacing exists between drift rates, then the corresponding number of sparks will also have an arithmetic relationship, assuming a constant carousel rotation rate (P_4).

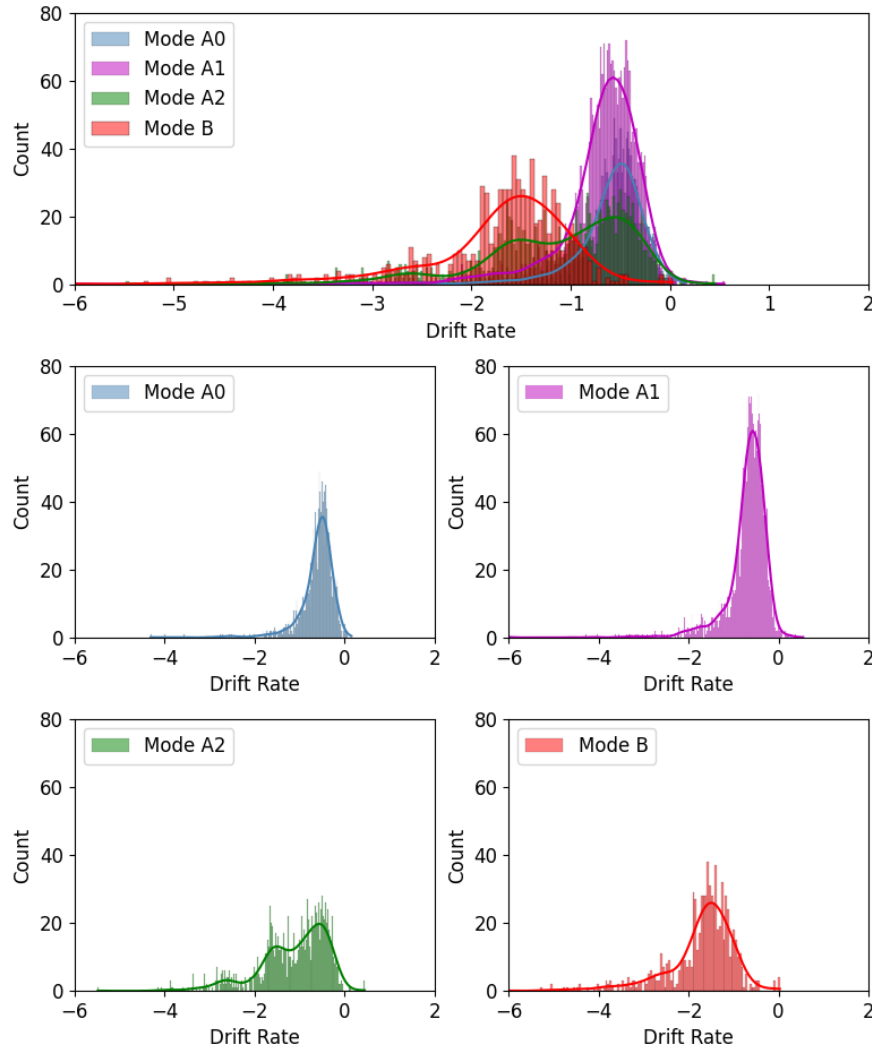


Figure 5.7: The figure shows a distribution of drift rates ($^{\circ}/P_1$) for different modes. The topmost panel shows the combined distribution, and the lower panels show the drift rates for individual modes.

5.2.4.1 A fourth-order polynomial fit of drift rates

On a closer examination of Fig. 5.6, it is evident that the drift rate is irregular. Furthermore, the drift rate does not simply evolve towards a higher or lower rate but shows variability, even within a particular mode. A linear or exponential drift rate could not accurately comprehend the complexity of this drift rate evolution. Hence, we tried to fit the average drift rate with a polynomial. Employing the polynomial regression method using `scikit_learn`, we successfully fit a fourth-order (quartic) polynomial function to the evolving drift rates. A higher-order polynomial could also describe the evolutionary drift rate. However, such a model might be counter-intuitive and would only provide a customised fitting rather than a general model. Fig. 5.8 shows the fourth-order polynomial fit of the drift rates (blue dots) for scan 2 of the observation made on MJD 59529 (November 11, 2022). The black line is the average drift rate at each pulse number, same as the grey envelope in Fig. 5.6. Different colours of the fourth-order polynomial fit correspond to different modes, following the colour scheme of Fig. 5.7. A direct comparison between the drift rate models in Fig. 5.3 and Fig. 5.8 can be made, where the latter shows the evolution of drift rate within a drift mode sequence. The fourth-order polynomial model can be seen to better describe the drift rate modulation as compared to the more simplistic, linear and exponential models, which lacked the detail.

To understand the overall drift rate modulation in various modes, we overlaid the drift rate fits for each mode, as shown in Fig. 5.9, where the x -axis shows mode length and y -axis the drift rate. The black line in each subplot shows the mean of drift rates (from the polynomial fits) with the pulse number. The grey envelope corresponds to the 1σ deviation from the mean drift rate. As expected, mode A0, which does not show any noticeable evolutionary behaviour, had an almost constant average drift rate across all instances, around -0.6. In contrast, the drift rate evolution of modes A1 and A2 is observable in their respective subplots. Drift rates in mode A1 can be seen to evolve towards a slower drift rate as compared to the commencing rate, whereas mode A2 shows

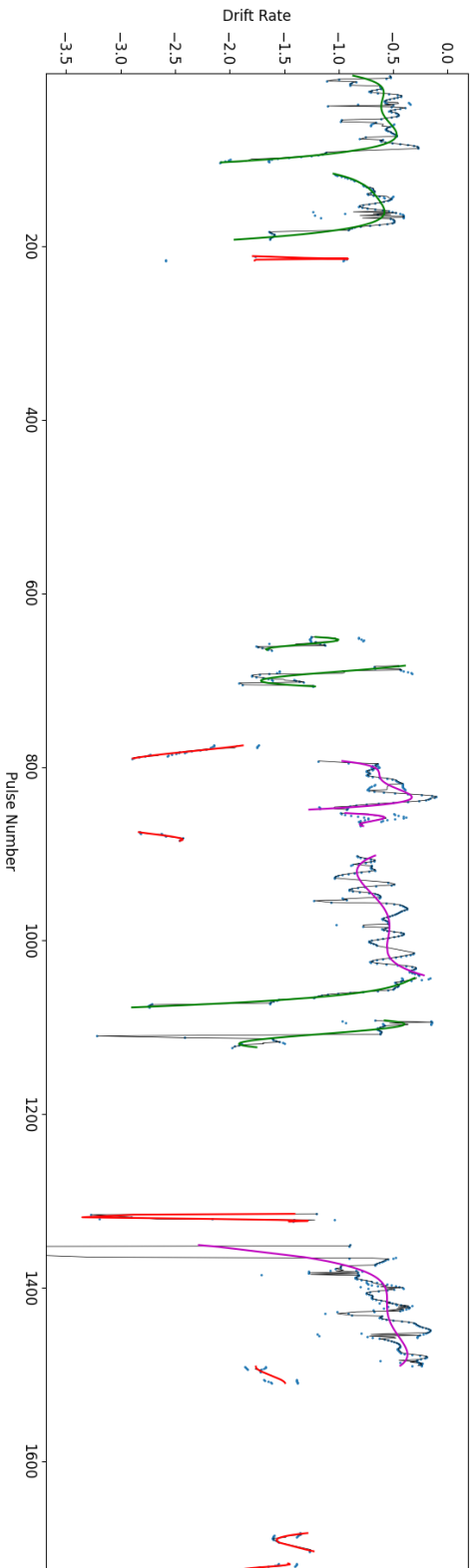


Figure 5.8: For the same observation of J0026–1955 shown in Fig. 5.3, the above plots show the quartic drift rate model fits. Using the cubic smoothing spline method, we calculated the drift rate ($^{\circ}/P_1$) at each pulse number, which is shown using the blue dots. The black line shows the average drift rate per pulse number. Drift rates for each of the modes are fit using a quartic polynomial, which describes a global evolution of drift rates. The colour scheme in the lower panel is similar to Fig. 5.7

an overall evolution towards a faster drift rate as it reaches the end of a drift sequence.

5.2.5 Memory across nulls

We also investigated the presence of memory across nulls, as reported by [McSweeney et al. \(2022\)](#). Our analysis shows that the short-lived nulls of PSR J0026–1955 indicate evidence of subpulse memory across nulls. This could be a subpulse phase memory or a drift rate memory. In the first scenario, the phase of the last subpulse before the null and the first subpulse after the null are similar. On the other hand, a drift rate memory could be a case where the drift rate across the null stays the same, and the driftbands could be extrapolated.

We followed the model fitting technique described in [5.2.1](#) to explore the latter. To check if there is indeed a drift rate connection between the sequence before the null and the sequence after the null, we fit the previous drift sequence (before null) using the model of choice (following the method in [5.2.1](#)). We then extrapolate the model to a subpulse right after the null sequence ends, allocating the subpulse a reasonable driftband number. We can consider a drift rate memory if the projected phase of the subpulse after the null matches the real subpulse within an error range. The error on phase prediction is calculated from the covariance matrix of the model fit (using standard uncertainty propagation). If the phase of the real pulse falls outside the subpulse phase range projected by the model, then we consider that there is no memory across the null. On the other hand, if the projected phase and the phase of the real pulse are within the error bars and smaller than P_2 (phase distance between two subpulses within a pulse), then we classify that null as being consistent with being phase-connected subpulse across the null. An example of drift rate memory across nulls is shown in the top panel of [Fig. 5.10](#), where the white lines depict the drift rate fits. The top panel in [Fig. 5.10](#) shows two drift sequences on either end and a null. By fitting the sequence before the null and projecting the drift rate behaviour to the latter sequence, one can note that the drift sequences before and after the

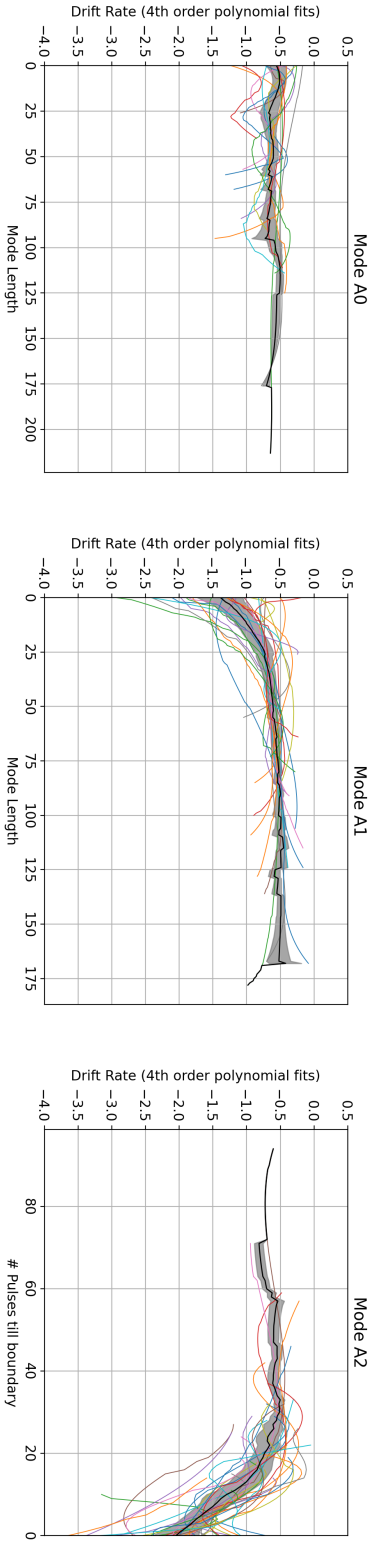


Figure 5.9: The figure combines all the drift rate fits using the quartic polynomial. The black line shows the average of all drift rates, and the grey envelope shows the 1σ deviation around the mean. *Left:* Drift rate for mode A0 stays constant on average despite sudden changes, as shown by the black line. *Middle:* Mode A1 is an evolutionary mode where the drift rate evolves from faster to slower drift rates. This is also shown by the black line, which evolves from an average drift rate of $\sim -1.3^\circ/P_1$ to $\sim -0.5^\circ/P_1$ with pulse number. *Right:* The evolutionary behaviour of mode A2 is the opposite of mode A1, where it evolves from a slower to a faster drift rate towards the end. In this plot, we have plotted the drift rates such that all drift sequences end together. This exercise shows the claimed drift rate behaviour. Following the trend of the black line (average drift rate), one can note that the drift rate evolves from $\sim -0.5^\circ/P_1$ to $\sim -2.0^\circ/P_1$.

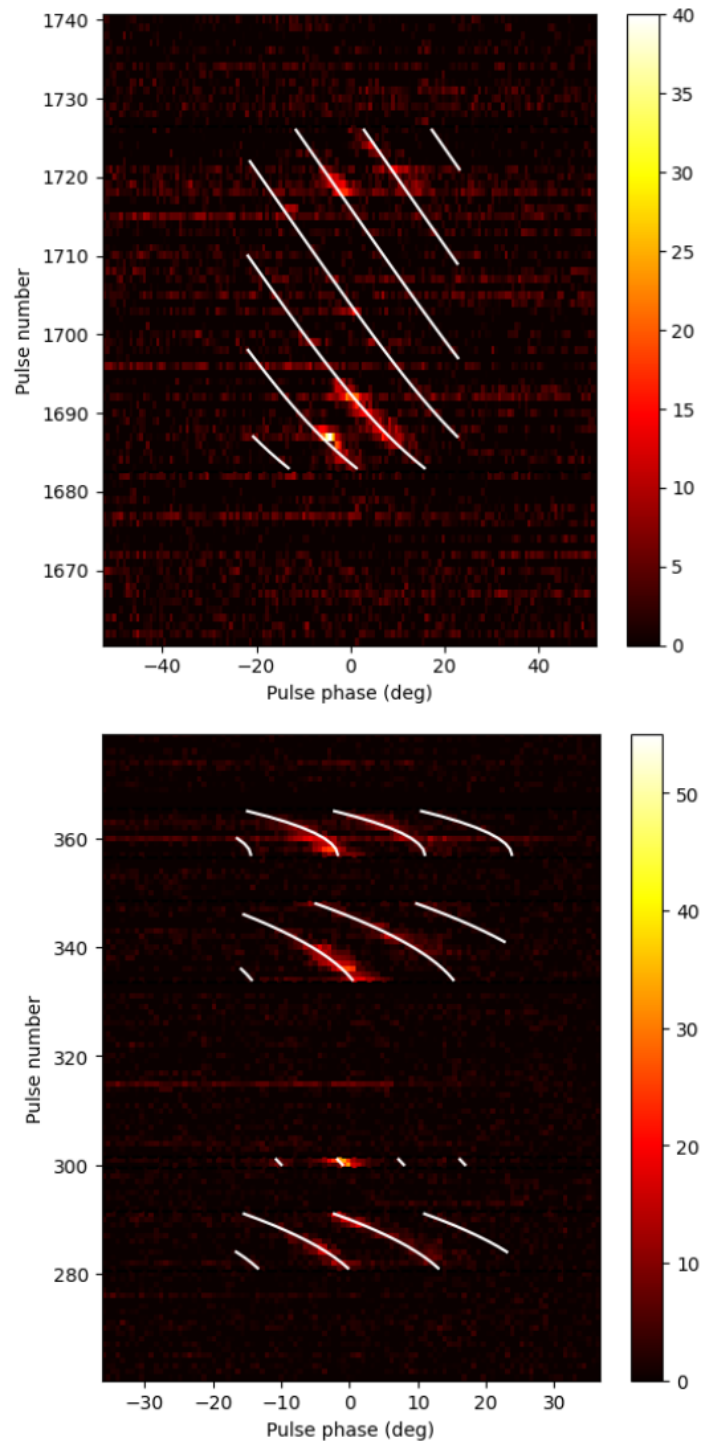


Figure 5.10: Examples showing speculative drifting during nulls for J0026–1955. *Top:* Between the two drifting sequences, there is a single burst at 1703. Extrapolating the drift rates of the first sequence (pulse 1683 to 1694) aligns well with the drifting behaviour at later pulse numbers. The drift band fits are shown to illustrate the approximate locations of the missing driftbands. *Bottom:* Between the four drifting sequences, though the drift rates may not align, the phase memory of the last burst before nulls is almost retained.

null are consistent.

We, however, do not find many instances of subpulse phase memory across nulls in our data. A handful of instances were initially recognised by visual inspection, as they did not show a drift rate memory across nulls. They were further investigated by calculating the phase of the subpulse before and after null. One such example is shown in the bottom panel of Fig. 5.10, where the subpulse phase before and after the null are almost the same. In contrast, since the sequences have different drift rates, a drift rate memory might not be present. A more careful analysis of longer observations is required to verify this fully.

5.3 Discussion

PSR J0026–1955 exhibits a multitude of pulse-to-pulse modulation phenomena, viz. subpulse drifting, mode switching, and nulling, as shown in Fig. 5.1. For each of the driftbands, subpulses arrive at earlier phases with pulsar rotation, thus conforming to the ‘positive drifting’ class of subpulse drifters (Basu et al., 2018b). However, the vertical separation between driftbands (i.e., P_3) can be seen to vary between different sequences, as well as within a drift sequence. There are instances where J0026–1955 can be seen to abruptly switch from one subpulse drifting mode to another, a behaviour exhibited by many other pulsars (e.g., Janagal et al., 2022; McSweeney et al., 2019). However, in addition to the abrupt mode change, the drift rate can also sometimes be seen to evolve gradually, which is a relatively rare phenomenon, observed in only a small subset of subpulse drifting pulsars, e.g., PSR B0943+10 (Bilous, 2018), PSR B0809+74 and PSR B0818–13 (Lyne & Ashworth, 1983). For PSR J0026–1955, a quick glance at mode A1 and A2 sequences (evolutionary drift modes) in Fig. 5.2 shows this variable drift rate. The pulsar also exhibits long and short-duration nulls, where an association between drifting and nulling can be drawn. Below, we discuss the variety of phenomena exhibited by J0026–1955 in light of the analysis presented in section 5.2.

5.3.1 Nulling Behaviour of J0026–1955

The analysis presented in section 5.2.3 highlights the unique nulling behaviour of J0026–1955, which exhibits complex emission properties. The nulling fraction at 400 MHz is approximately 58%, an estimate reached from 330 minutes of observation, whereas, at 155 MHz, it was estimated to be 77% from 192 minutes of MWA observation (McSweeney et al., 2022). This discrepancy suggests a possibility that the nulling behaviour of J0026–1955 may not be broadband and that there may be frequency-dependent mechanisms at play. Frequency-dependent nulling has been observed in some pulsars, where the nulling behaviour varies depending on the observed frequency (e.g., Bhat et al., 2007). However, given the modest separation in the frequency bands (with band edges separated by ~ 130 MHz and the centre frequencies differing by a factor of ~ 2.5), it is unclear if the observed discrepancy is entirely attributable to frequency-dependent nulling. Alternatively, the observed inconsistency could simply be an unintended observational bias, where the MWA observations were incidentally made around the long nulls. The perceived discrepancy could also be because of the presence of an emission component with a shallow spectral index leading to a null at 155 MHz. Assuming that J0026–1955 exhibits broadband nulling, a combination of the number of nulls out of the total number of pulses observed at 155 MHz and 400 MHz will imply a nulling fraction of $\sim 65\%$.

It is also possible that the nulling behaviour of J0026–1955 is complex and multifaceted, involving both broadband and frequency-dependent mechanisms. Different models attribute pulsar nulling to intrinsic changes in the magnetosphere, such as temperature fluctuations altering coherence conditions (Cheng, 1981; Deich et al., 1986), switching between gap discharge mechanisms (e.g., Daugherty & Harding, 1986; Zhang et al., 1997), variations in magnetospheric currents (Timokhin, 2010), change in pulsar beam geometry (Herfindal & Rankin, 2007, 2009; Rankin & Wright, 2008), disruption of the entire particle flow in the magnetosphere (Kramer et al., 2006), etc. Though such models may be able to describe the long-period nulls seen for J0026–1955, the presence of subpulse

(phase or drift rate) memory across nulls challenges these theories for at least the case of short nulls where such memory exists. Further investigation is needed to fully understand the nature of the observed disparity and the complex emission properties of J0026–1955.

5.3.2 Drift Rate - Nulling Correlation

There have been only a limited number of investigations that explored a correlation between nulling and subpulse drifting. For example, PSR B0818–41 presents a case where a decrease in the pulsar drift rate is accompanied by a gradual decrease in intensity before the onset of a null (Bhattacharyya et al., 2010). PSR B0809+74 also shows an association between nulls and subpulse drifting, where the drift rate deviates from normal after the nulls (van Leeuwen et al., 2003). Using the partially screened gap model, the authors suggest that some kind of “reset” of the pulsar’s radio emission engine occurs during the nulls, which is responsible for the conditions of the magnetosphere. For PSR B0809+74, van Leeuwen et al. (2003) suggest that nulling and subpulse drifting may be related, with changes in emission beam geometry potentially causing both the nulling and changes in the drift behaviour. Wang et al. (2007) suggested that emission can cease or commence suddenly when the charge or magnetic configuration in the magnetosphere reaches the so-called “tipping point”; however, the triggering mechanism for such stimulus is unknown. In the case of PSR J1822–2256, Janagal et al. (2022) also showcase a relationship between nulling and mode changing, where a null preceded most occurrences of their mode D. Such correlations suggest that emission mechanisms and magnetosphere dynamics between nulls and subpulse drifting may be strongly related.

PSR J0026–1955 also provides some compelling evidence of a possible correlation between subpulse drifting and nulling. Our observations suggest a complex and dynamic mechanism underlying the pulsar radio emission, with important implications for understanding astrophysical processes in extreme environments. In particular, we have found that the pulsar J0026–1955 likely switches to a null state after mode A2. Mode A2 is an

evolutionary mode, where the drifting begins at a slower drift rate and evolves towards a faster drift rate before the mode eventually ends. In 27 out of 31 instances, mode A2 is followed by a null, either short or long. In such cases, the ramping up towards the faster drift rate begins remarkably consistently about 20 pulsar rotations prior to the null (see Fig. 5.10), which suggests that the null itself might be causally related to the preceding drifting behaviour. In the rest of the four sequences, mode A2 was once at the end of our observation and was followed by either mode A0 or A1 in three instances. These occurrences can also be seen as a drift reset, where the pulsar temporarily evolves to a faster drift rate and then returns to a slower one. This reset could also be due to a change in the magnetospheric conditions before a “tipping point” was reached. It was also noted that not every null sequence followed mode A2, but a null followed most occurrences of mode A2. We did not find any strong correlation between the intensity of subpulses towards the onset or end of a null. The variation in pulse intensity of transitions from burst to null was sometimes abrupt and smooth at other times and lacked any compelling evidence of intensity dependence. It is worth noting that this kind of phenomenon, where nulls affect the drifting behaviour leading up to them, is relatively rare in contrast with the more commonly studied effect of nulls on burst sequences that come after them (e.g., [Janagal et al., 2022](#); [Lyne & Ashworth, 1983](#); [van Leeuwen et al., 2003](#)). A deeper understanding of these rare cases can provide useful insights into the complex dynamics relating nulls and subpulse drifting.

5.3.3 Memory Across Nulls

Only a limited number of pulsars retain the information about previous subpulses during nulls, as demonstrated by, e.g., [Unwin et al. \(1978\)](#) and [Gajjar et al. \(2017\)](#). This memory retention can provide valuable insights into the true nature of the nulling phenomenon and any correlation with subpulse drifting it may have. If intrinsic changes in the pulsar magnetosphere lead to both nulls and drift-rate modulations, studying the interactions

between these phenomena could offer valuable insights into the mechanisms that trigger and facilitate transitions between the different states. Subpulse memory across nulling in drifting pulsars has been generally attributed to either of the two reasons: (1) the polar cap continues to discharge, but the emission is not observed (Filippenko & Radhakrishnan, 1982), or (2) the subpulse ceases drifting for the duration of the null (Unwin et al., 1978). In the first case, the absence of radio emission is attributed to the lack of coherent structure, and the drift rate remains the same before and after the null. Thus, a part of the drift sequence would be missing, though one could still map the driftbands with similar drift rates pre- and post-null, showing ‘drift rate’ memory across nulls. Whereas in the second scenario, the subpulse drifting is thought to resume at the phase where it left off, demonstrating a subpulse ‘phase memory’ across nulls. As described in section 5.2.5, we have encountered possibilities of both ‘drift rate’ memory and ‘subpulse phase’ memory across nulls in the case of J0026–1955.

5.3.3.1 Drift rate memory

J0026–1955 exhibits a clear case of subpulse drift memory (top panel in Fig. 5.10), where the pulsar seems to remember the drift rate even after a short (~ 20 pulses) null. The study described in Filippenko & Radhakrishnan (1982) suggests that nulling in pulsars results from an uninterrupted and stable discharge in the polar gap rather than a complete cessation of sparks. This observation is similar to the case of J1840–0840, where the drift rate stays the same across the null, and an entire driftband is missing from the sequence (Gajjar et al., 2017). PSR J1840–0840 also shows ‘subpulse phase’ memory in conjunction with the ‘drift rate’ memory.

The cause of undetectable radiation during nulling can be attributed to the absence of the dominant coherence mechanism present during regular pulsar operation rather than the lack of particle flux from the polar cap (Filippenko & Radhakrishnan, 1982). Therefore, during the null states, the subpulses on the polar cap may continue to drift during the null

state, either at similar or different rotation speeds. In this case, the phase of the subpulse after the null sequence can be anticipated based on the duration of nulls. In the case of J0026–1955, when the pulsar switches its emission back on after a null, the phase of the subpulse can be extrapolated from the drift rate model before the null. The predicted phase was well within the error range for drift sequences around short nulls. This finding supports the idea that drifting and sparking may still be operational during nulls, providing further evidence for the two scenarios previously observed in drifting pulsars.

5.3.3.2 Subpulse phase memory

As shown in the lower panel of Fig. 5.10, J0026–1955 also presents evidence of a ‘phase’ memory across nulls, where the drift rate does not necessarily stay the same across the nulls. Still, the phase of the last subpulse before the null is almost identical to that of the first subpulse after the null. Similar behaviour is observed in a few other pulsars like B0809+74 and B0818–13, where the drift rate changes after null sequences (Janssen & van Leeuwen, 2004; Lyne & Ashworth, 1983; van Leeuwen et al., 2003). During some of these interactions, the pulsars also seem to indicate some kind of phase memory, such that information regarding the phase of the last subpulse was retained during the null state. Cheng & Ruderman (1980) propose that during the null, the drifting stops and the position of the sparks are remembered by the presence of a hotspot on the pulsar surface. This would imply that once the drifting resumes, the sparks will reform at their previous position. PSR B0031–07 was shown to retain the memory of its pre-null burst phase across short nulls (Joshi & Vivekanand, 2000; Vivekanand & Joshi, 1997). In their study by Gajjar et al. (2017), PSR J1840–0840 presents a unique example of both ‘subpulse phase’ and ‘drift rate’ memory across null. In our data, we only had a few occurrences of memory across nulls of both kinds. A more detailed analysis of drift rate and subpulse phase memory around nulls needs to be conducted for J0026–1955 using longer observations, thus increasing the sample size of such events.

5.3.4 Subpulse Drifting Model for J0026–1955

J0026–1955 presents an exciting and rare phenomenon of drift rate evolution (modes A1 and A2), in addition to regular subpulse drifting with a constant drift rate (modes A0 and B). The pulsar exhibits changes in drift rate over sequences, with mode A1 showing a trend towards a slower drift rate and mode A2 showing a trend towards a faster drift rate with increasing pulse number. Furthermore, irrespective of the modal transitions, we have also observed an inter-modal driftband connectivity in most mode-switching cases. We utilised the techniques described in section 5.2.4 to analyse the evolution of drift rates across the driftbands and sequences. Measuring the slopes of individual driftbands was essential to scrutinise any changes in the drifting pattern.

Furthermore, we modelled the drift rate behaviour across the drift sequences using a quartic polynomial. The quartic model fits were then used to understand the global drift rate variation for the different modes, as shown in Fig. 5.9. The figure shows that the modes A1 and A2 for J0026–1955 display a gradual evolution from their initial drift rates. It is noteworthy that the change of drift rate for mode A2 ($\sim -0.5^\circ/P_1$ to $\sim -2.0^\circ/P_1$) is almost twice as much as the change of drift rate in mode A1 ($\sim -1.3^\circ/P_1$ to $\sim -0.5^\circ/P_1$). Hereafter, we discuss the possible modifications/additions to the existing carousel model that can explain the observed unique behaviour of J0026–1955.

5.3.4.1 Variable Spark Configuration in Carousel Model

As discussed in Rankin et al. (2013), McSweeney et al. (2017), and Janagal et al. (2022), different modes and drift rates of a pulsar can be attributed to a carousel with varying numbers of sparks for each subpulse drifting mode. In such cases, the drift rate is observed to change abruptly. This sudden change cannot be ascribed to the carousel rotation rate, as it would imply significant magnetosphere reconfiguration over a short time scale. However, the drift rate change within a single pulsar rotation can be due to the reconfiguration of spark distribution. In the case of the evolutionary drifting modes of J0026–1955, the idea

of a carousel with a constantly changing number of sparks to describe the changing drift rate may be counter-intuitive. Nevertheless, the non-evolutionary modes (A0 and B) may still have a fixed spark configuration.

An alternative hypothesis, which could involve a changing carousel rotation rate, would need a slow change in the spark carousel itself, where the gradual evolution is a signature of the spark configuration relaxing into a new arrangement after a spark suddenly appears or disappears from the carousel (McSweeney, 2019). Such ‘relaxation’ of the drift rate is reminiscent of the behaviour observed in PSR B0809+74 (Lyne & Ashworth, 1983), where, after a null, the pulsar would temporarily attain a faster drift rate before relaxing into a steady drift rate. They further suggest that a perturbation might alter the drift rate (and emission, thus causing a null), after which the drift rate recovers exponentially to its normal value.

If the number of sparks in the carousel is changing, then the carousel will take some finite amount of time for the sparks to rearrange themselves, for example, into the new configuration in which the sparks are equidistant from each other. During this relaxation time, the angular speed of individual sparks may differ from the angular speed of the whole carousel. In that case, the observed drift rate at any one moment will only depend on the spark that is ‘under’ the line of sight during any given rotation period. In this view, the observed drift rate can appear to change slowly without requiring the average carousel rotation speed to change, as long as the time scale for the spark reconfiguration is relatively long.

If, as the above suggests, the sparks reconfigure themselves only slowly after one of the sparks either appears or disappears, one observational consequence of this is that the driftbands should always look connected, which appears to be the case for J0026–1955. This still remains true in the presence of aliasing, although the observed drift rate changes may be magnified. In comparison, van Leeuwen et al. (2003) point out that connectivity

of driftbands is impossible if the carousel rotation rate transitions from non-aliased to aliased regimes.

5.3.4.2 Carousel Model in Partially Screened Gap

Alternatively, a steady change in the carousel rotation rate (P_4) with a constant spark configuration is also a plausible explanation for the evolutionary drift modes of J0026–1955. In such a case, some conditions might change at the pulsar surface, making the spark carousel change its rotation speed. As a result, the carousel rotation rate varies smoothly, resulting in a gradual drift rate evolution. Below, we provide a hypothesis, using the partially screened gap model (PSG; [Gil et al., 2003](#)), for such a phenomenon that can gradually alter the carousel rotation rate.

According to the PSG, a reverse flow of electrons towards the polar cap leads to an ion discharge in the gap region, which ultimately acts as a screen. Due to this screen, the electric field in the polar cap reduces, which reduces the spark velocity (see eqn 28 of [Ruderman & Sutherland, 1975](#)). [van Leeuwen & Timokhin \(2012\)](#) also suggests that the dependence of the drift rate on the electric and magnetic fields boils down to a dependence on the variation of the accelerating potential across the polar cap. Hence, a variation in the polar gap results in an increase/decrease in the spark velocity, which in turn may also increase/decrease the carousel rotation rate (regardless of whether the drifting is aliased). Consequently, the carousel rotation rate will also affect P_3 . In the case of no aliasing, the drift rate will be more negative for a faster carousel rotation rate, and the P_3 value will be smaller. Further, as discussed in [Janagal et al. \(2022\)](#), a change in drift rate is reflected in the emission heights, where faster drift rate (lower P_3 value) emission is thought to originate from higher emission heights; and at lower emission heights, emission from a slower drift rate (higher P_3 value) is observed. For curvature radiation, the only way to observe a change in the emission height at one observation frequency is if there is a change in the magnetic field lines. For a changing emission height, the foot points of

the magnetic field lines will be closer to or further from the (dipolar) magnetic pole, implying a changing size of the observed spark carousel. For the evolutionary drift modes of J0026–1955, where the drift rate is seen to vary drastically within a drift sequence, a change in emission height (at a fixed observational frequency) would automatically suggest a variable carousel rotation rate for a fixed carousel configuration.

Extrapolating the PSG model, if the screening increases due to the ion discharge in the polar cap region, the electric field in the polar gap region will decrease, lowering the spark velocity and, consequently, lowering the carousel rotation rate. Given the proposed relation between P_4 and emission heights, the emission from a carousel with lower P_4 will come from a lower altitude in the pulsar magnetosphere. We observe a slow drift rate evolution in mode A1, which could be where the screening steadily increases, causing an evolution towards a slower carousel rotation rate. Similarly, mode A2 can be the case where the screening lowers, causing the drift rate to increase and the emission to come from higher altitudes. Since the typical mode length of observed mode A2 occurrences is not as long as mode A0 or A1, we can only conjecture that the screening cannot lower beyond a certain extent.

For modes A1 and A2, a gradual change in the carousel rotation rate might be an acceptable model. This is also consistent with the general understanding that the rotation rate of the carousel cannot change its magnitude or direction abruptly during a single pulsar rotation (as it implies a rapid change in the pulsar magnetosphere), although it may exhibit a slow evolution.

5.3.4.3 Revisiting Mode A2 - Null Correlation

Our findings suggest a strong correlation between mode A2 and nulling across multiple observation epochs, as discussed in section 5.3.2. Such an association indicates the intrinsic nature of these changes and their close relationship with the nulling process.

The gradual transition from slow to fast drift rate, via addition/reduction of sparks as discussed in section 5.3.4.1, might trigger a “reset” of the pulsar’s radio emission engine, causing the emission to cease for several pulses. J0026–1955 provides compelling evidence for a scenario in which the electromagnetic conditions in the magnetosphere region responsible for radio emission attain a null state after the considerable drift rate evolution seen in mode A2. Additionally, the stability of sparks for fast drift rates could be a reason for short sequences. This implies that for mode A2, the spark configuration becomes unstable once the drift rate is sufficiently fast due to an increase in the number of sparks, causing a null. The instability argument can also explain why mode B sequences only last for a short time compared to all the other modes.

Alternatively, following the subpulse drifting model suggested in section 5.3.4.2, mode A2 might indicate the scenario where screening decreases, causing the electric field in the polar gap region to increase. This impacts the spark velocity and, thus, the carousel rotation rate. As the carousel rotation rate increases (due to a decrease in screening), P_3 decreases and the driftbands appear closer in the pulse stack. Using the direct dependence between P_4 and emission heights (derived from the inverse relation between P_3 and emission heights), we can deduce that the emission comes from increasingly higher emission heights for mode A2. Alternatively, it is possible that due to our line of sight, we cannot observe the pulsar past a certain emission height. The drift sequence ends very soon after mode A2 achieves a significantly low drift rate. Similarly, due to the line-of-sight constraint, we might explain why modes with lower drift rates, like mode B, have comparatively shorter mode lengths.

5.4 Summary

We have conducted a thorough analysis of subpulse drifting behaviour in PSR J0026–1955 at 300-500 MHz from uGMRT observations. Our results and conclusions from this study are summarised below.

1. From our observations, we have found that the pulsar exhibits short- and long-duration nulls, with an estimated nulling fraction of $\sim 58\%$ from our uGMRT observations. The nulling fraction is in stark difference from $\sim 77\%$ that was observed at 155 MHz in MWA observations. This disparity could be due to differences in the lengths of observations, or a shallow spectral index component, or a frequency dependence of nulling.
2. The pulsar exhibits unusual drifting behaviour, with both evolutionary and non-evolutionary drift rates. Further, we categorise the unusual subpulse drifting behaviour of this pulsar into two drifting modes: A and B, where mode B is a non-evolutionary mode with a faster drift rate. Mode A was further sub-categorised depending on its evolutionary behaviour. Mode A0 is a non-evolutionary mode with a drift rate 3-4 times slower than mode B. The lack of any curvature in A0 suggests that the viewing geometry must be such that the driftband curvature arising from purely geometric considerations (the “geometric curvature”) is negligible across the pulse window. Mode A1 is an evolutionary mode which shows a smooth evolution of drift rate from fast to slow. On the other hand, the drift rate in mode A2 evolves from a slower to a faster drift rate.
3. The individual driftbands for J0026–1955 are not linear and have variable drift rates. We used a cubic smoothing spline estimate on individual driftbands and calculated the gradient (drift rate) at each pulse. To understand the overall drift rate modulation, we fit the drift rates using a quartic polynomial. The model helped in recognising the inter-band and inter-mode variability in drift rates. Though a simplistic higher-order polynomial can describe the global evolution empirically, understanding the local drift rate variability requires more complex modelling.
4. The pulsar J0026–1955 shows an evolution in drift rate for modes A1 and A2. We advocate the following two models to explain their behaviour:

- (a) *Variable spark configuration* - The gradual evolution of drift rate in modes A1 and A2 could be caused by a slow change in the spark configuration as the carousel reconfigures into an optimal arrangement after a spark appears or disappears. During this reconfiguration, the angular speed of individual sparks may differ from the average carousel rotation. In this case, the observed evolution in drift rate will be due to the motion of sparks “under” the line-of-sight as the entire carousel slowly recomposes.
- (b) *Variable carousel rotation rate* - In this model, we propose that the evolution in drift modes can be explained by a smoothly varying carousel rotation rate with a direct correlation with emission height rather than changes in the number of sparks. The evolution in carousel rotation rate is thought to originate from an increase or decrease in screening in the polar gap region. Therefore, as the screening decreases/increases, the carousel rotates faster/slower (mode A2/A1), with the emission coming from higher/lower altitudes in the pulsar magnetosphere.

A combination of the two suggested models might also be plausible, a possibility that should be explored in future.

5. J0026–1955 shows robust evidence of subpulse memory across nulls. In multiple instances, we have found the possibility of ‘drift rate’ and ‘subpulse phase’ memory across nulls. We believe that there could be an uninterrupted stable discharge in the polar gap during the null, which is not observed due to the absence of a dominant coherence mechanism or a partially screened gap making the generation of detectable radio emission difficult.
6. J0026–1955 exhibits an almost consistent behaviour, where a null often follows mode A2. We propose two hypotheses for this behaviour:
 - (a) The transition from slow to fast drift rates due to the appearance/disappearance

of a spark often triggers a “reset” of the pulsar’s radio emission engine, which often culminates in a null. This reset is most likely to take place after the occurrence of mode A2, where the pulsar transitions from a slow to a fast drift rate. Not every occurrence of a null sequence is preceded by mode A2. However, most occurrences of mode A2 are followed by a null state. A null, followed by mode A2, must relate to a defined pathway in the pulsar emission as it is consistently observed across all independent data sets (from two epochs of observations).

- (b) Using the proposed carousel model, we advocate the idea that a decrease in screening increases the electric field in the polar gap region and impacts the spark velocity and carousel rotation rate. This results in a decrease in P_3 and closer driftbands in the pulse stack, suggesting that emission comes from higher emission heights for mode A2. The sequence ends soon after mode A2 achieves a low drift rate, possibly due to our line of sight not being able to observe the pulsar beyond a certain emission height.

Chapter 6

Summary and Future Prospects

“Everything’s got to end sometime. Otherwise, nothing would ever get started.”

- The Doctor

The underlying theme of this thesis has been to investigate the emission mechanism in pulsars through the observed variability in single pulse emission properties. The work presented in this thesis demonstrates the importance of wide-band single-pulse studies of pulsars and their potential to understand the intricacies of the pulsar emission process. Importantly, single-pulse studies of pulsars provide a unique window for probing the dynamics of pulsar magnetospheres. Therefore, studies of single-pulse phenomena can provide valuable insights into the underlying physical processes. In this context, we studied the processes responsible for pulsar radio emission from an observational perspective, using high-quality data collected at sub-GHz frequencies. In particular, much of the analysis attempts to shed some light on different kinds of single-pulse emission phenomena and constrain some of the current emission theories and models for understanding pulsar emission. Specifically, we have studied the pulse-to-pulse variability, the subpulse drifting and nulling phenomena, and related phenomenology, including mode switching and evolving subpulse drift rates.

Large variabilities in pulse amplitude were noted even in the early days of pulsar

studies. The pulsar emission processes can manifest, at times, in the form of *organised* modulations in pulse amplitude and phase, and are revealed in observations in the form of repeating patterns in pulse sequences (e.g., subpulse drifting). Alternatively, the underlying processes may give rise to variations in single pulse amplitude and phase, which can be quite erratic with no specific order, i.e., *unorganised* modulations. Despite extensive studies over the past five decades, we do not have a concrete theory that can explain the observed emission properties satisfactorily.

The complexity of the emission mechanism and the observed diversity in pulsar emission phenomena continue to challenge our attempts to formulate comprehensive theories. As a result, even after decades of research and the observations of thousands of pulsars, the details of how relativistic plasma behaves in ultra-strong magnetic and gravitational fields remain not well understood.

Nearly half of the known pulsar population exhibit organised modulation in the form of subpulse drifting. This intriguing phenomenon, therefore, holds the potential to unlock the secrets of pulsar emission physics. The traditional carousel model is able to explain the classic drifting behaviour seen in several pulsars. However, a good fraction of pulsars exhibit much more complicated behaviours, such as bi-drifting, mode changing, etc., that continue to challenge the carousel model. Over the years, several extensions or modifications have been proposed to the basic carousel model in an effort to account for these observed anomalies. Yet, a comprehensive theory that can explain the diverse range of observed subpulse drifting behaviours remains elusive.

We investigated the subpulse drifting phenomenon in the pulsar PSR J1822–2256 using observations made with the upgraded Giant Metrewave Radio Telescope (uGMRT). Our findings from the study of PSR J1822–2256 are summarised below:

1. Based on the measured drift periodicities and their characteristics, we classified the drifting behaviour of this pulsar into four distinct drift modes – A, B, C, and D.

2. We examined the possible spark configurations for each mode within the framework of the carousel model.
3. Our analysis also revealed the presence of short-duration ‘pseudo nulls’ alongside genuine nulls in the pulsar’s emission across the entire observed frequency range ($\sim 300 - 750$ MHz). We conjecture that the pseudo nulls occur when the observer’s line of sight passes through a minimum of sparks (mostly apply to modes B and C).
4. We have also explored the frequency-dependent subpulse behaviour and estimated corresponding emission heights for the different drift modes. Our study revealed an intriguing correlation between the observed drift rates and the inferred emission heights.

If confirmed in more pulsars, especially the ones that show both mode switching and subpulse drifting phenomena, such a correlation between emission heights and drift rates can potentially provide useful hints toward understanding the pulsar emission mechanism. There have been recent studies investigating the prevalence of subpulse drifting in pulsars (e.g., [Song et al., 2023](#); [Weltevrede et al., 2007](#)). Further studies involving a detailed exploration with the objective of constraining the possible dependence of emission heights on the observed drift rate (or P_3) can, therefore, prove very instructive. Our work also highlighted a possible connection between nulling and subpulse drifting, which can be explored further using longer, more sensitive observations. Establishing clear links between the emission phenomena, such as sub-pulse drifting and nulling, can provide valuable clues to develop an improved understanding of the fundamental physical processes that drive the pulsar radio emission mechanism.

In this thesis, we also investigated the evolutionary subpulse drifting phenomenon in PSR J0026–1955, a pulsar recently discovered with the Murchison Widefield Array, Australia’s SKA precursor telescope. The focus of this work was a uGMRT follow-up of this pulsar at 300–500 MHz. J0026–1955 is known to exhibit an evolutionary drift rate

behaviour in its subpulse drifting modes (McSweeney et al., 2022). Only a handful of pulsars have been found to show even a small evolution in their drift rates; for example, the temporary drift rate changes after a null, as seen in PSR B0809+74.

1. From our observations, we revealed at least two distinct subpulse drifting modes, both of which exhibited evolutionary drift rates.
2. Our analysis and results further prompted us to propose two possible modifications to the carousel model in an attempt to describe the observed complexity in subpulse drifting. However, both of these modifications need to be tested thoroughly alongside exploring alternative theoretical models.
3. Our analysis also provides clear evidence of a correlation between one of the evolutionary drift modes and nulling, which can also provide another vital clue for developing an improved understanding of the drifting and nulling phenomena in pulsars.

The distinctive subpulse drifting behaviour seen in this pulsar, therefore, presents a perfect opportunity to scrutinise the classical carousel model in an attempt to develop its useful extensions further or even consider suitable alternatives. Furthermore, it is important to note that the analysis so far is focused on observations at frequencies below ~ 500 MHz, and hence detailed studies at complementary (higher) frequency bands ($\gtrsim 500$ MHz) may also help further solidify models of drift rate evolution.

Our study of J0026–1955 is one of the first detailed explorations of the evolutionary drifting behaviour, and it paves the way for further examination in this direction. Yet another area of extension is polarisation analysis, which may help to estimate emission heights and link to the evolutionary drifting behaviour. PSR J0026–1955 also serves as an excellent example for showcasing the potential of MWA-like next-generation telescopes. In particular, with ongoing all-sky pulsar surveys such as the Southern-Sky MWA Rapid

Two-Metre (SMART) pulsar survey, we can expect to find more pulsars like J0026–1955. In the context of J0026–1955, we have proposed two possible modifications to the carousel model to describe our observations. These modifications can be tested alongside exploring other theoretical models as more such objects are discovered.

This thesis also investigated the pulse-to-pulse variability in PSR J1820–0427. This work involved understanding the dynamic pulsar emission behaviour using high-quality observations with the uGMRT and MWA.

1. In this work, we investigated the frequency dependence of single pulse properties. We found that the pulse fluence distribution followed a log-normal distribution across the observed frequency range (300-750 MHz).
2. Our analysis revealed, for the first time, a steepening of the spectral index for high-intensity pulses.
3. We have also demonstrated the application of a new method for calibrating single-pulse flux densities using simultaneous imaging and phased array data.
4. At low frequencies, the reconstructed average profile at 185 MHz (MWA) revealed a post-cursor-type feature in the pulsar emission, for which no clear counterparts are seen at higher frequencies(300–750 MHz).
5. Our analysis also indicated a steeper spectrum for high-intensity pulses, as compared to regular pulses, thus pointing towards an anomalous emission mechanism.

In conjunction with the observed log-normal distributions of single-pulse fluences, our results could potentially aid the current understanding of coherent emission mechanisms for pulsar radio emission and their spectral dependencies. Further investigations of this kind hold the promise of extending our understanding of the fundamental physical processes that drive pulsar radio emission. Overall, our study highlights the benefits of

high-sensitivity single-pulse analysis over a wide frequency range in the context of understanding pulsar emission physics. The distinctive perspective offered by single pulse studies of pulsars will continue to be promising for uncovering the fundamental mechanisms that drive pulsar radio emission. The single-pulse calibration technique developed as part of this work can also be exploited when observations are made with the concurrent interferometric and phased array mode capabilities, which can become routine for pulsar observations with uGMRT.

Finally, this thesis is based on observational studies of pulsars using low-frequency instruments – the uGMRT and the MWA, which are also among the recognised pathfinders/precursors for the Square Kilometre Array. Clearly, the capabilities of low-frequency telescopes can be leveraged to gain valuable insights into the spectral characteristics of pulsars in the frequency range below ~ 1 GHz. With the enhanced sensitivity of new-generation telescopes such as MeerKAT and FAST, there will be additional opportunities for in-depth investigations of single-pulse phenomena across a large number of pulsars. In summary, by utilising high-quality data from upcoming telescopes like the SKA pathfinders and eventually the SKA itself, studies of the kind presented in this thesis can be extended to a larger sample of pulsars, which may help contribute to developing an improved understanding of pulsar emission physics. In essence, this thesis has set the stage for a detailed exploration of both organised and unorganised single pulse emission phenomena, alongside shedding some light on the complex emission processes that underpin the coherent emission mechanisms.

“We are all stories in the end. Just make it a good one. Eh?”

- The Doctor

References

- Akaike, H. 1974, A new look at the statistical model identification, *IEEE Transactions on Automatic Control*, 19, 716
- Andaç, I. C., Cerutti, B., Dubus, G., & Ekşi, K. Y. 2022, Intra-pulse variability induced by plasmoid formation in pulsar magnetospheres, *A&A*, 661, A130
- Baade, W., & Zwicky, F. 1934, Remarks on Super-Novae and Cosmic Rays, *Phys. Rev.*, 46, 76
- Backer, D. C. 1970a, Peculiar Pulse Burst in PSR 1237 + 25, *Nature*, 228, 1297
- Backer, D. C. 1970b, Pulsar Nulling Phenomena, *Nature*, 228, 42
- Backer, D. C. 1973, Pulsar Fluctuation Spectra and the Generalized Drifting-Subpulse Phenomenon, *ApJ*, 182, 245
- Backer, D. C., Rankin, J. M., & Campbell, D. B. 1976, Orthogonal mode emission in geometric models of pulsar polarisation., *Nature*, 263, 202
- Bartel, N., Morris, D., Sieber, W., & Hankins, T. H. 1982, The mode-switching phenomenon in pulsars., *ApJ*, 258, 776
- Basu, R., & Mitra, D. 2018, Subpulse drifting, nulling, and mode changing in PSR J1822-2256, *MNRAS*, 476, 1345
- Basu, R., Mitra, D., & Melikidze, G. I. 2018a, Erratum: “Meterwavelength Single-pulse

- Polarimetric Emission Survey. III. The Phenomenon of Nulling in Pulsars” (2017, ApJ, 846, 109), *The Astrophysical Journal*, 857, 77
- Basu, R., Mitra, D., Melikidze, G. I., & Skrzypczak, A. 2018b, Classification of subpulse drifting in pulsars, *Monthly Notices of the Royal Astronomical Society*, 482, 3757
- Basu, R., Mitra, D., Melikidze, G. I., & Skrzypczak, A. 2019, Classification of subpulse drifting in pulsars, *MNRAS*, 482, 3757
- Bell, M. E., Murphy, T., Johnston, S., et al. 2016, Time-domain and spectral properties of pulsars at 154 MHz, *MNRAS*, 461, 908
- Bhat, N. D. R., Cordes, J. M., Camilo, F., Nice, D. J., & Lorimer, D. R. 2004, Multifrequency Observations of Radio Pulse Broadening and Constraints on Interstellar Electron Density Microstructure, *ApJ*, 605, 759
- Bhat, N. D. R., Gupta, Y., Kramer, M., et al. 2007, Simultaneous single-pulse observations of radio pulsars. V. On the broadband nature of the pulse nulling phenomenon in PSR B1133+16, *A&A*, 462, 257
- Bhat, N. D. R., Swainston, N. A., McSweeney, S. J., et al. 2023a, The Southern-sky MWA Rapid Two-metre (SMART) pulsar survey - I. Survey design and processing pipeline, *Publications of the Astronomical Society of Australia*, 1–22
- Bhat, N. D. R., Swainston, N. A., McSweeney, S. J., et al. 2023b, The Southern-sky MWA Rapid Two-metre (SMART) pulsar survey - II. Survey status, pulsar census, and first pulsar discoveries, *Publications of the Astronomical Society of Australia*, 1–22
- Bhat, N. D. R., Swainston, N. A., McSweeney, S. J., et al. 2023a, The Southern-sky MWA Rapid Two-metre (SMART) pulsar survey – I. Survey design and processing pipeline, *arXiv e-prints*, arXiv:2302.11911

- Bhat, N. D. R., Swainston, N. A., McSweeney, S. J., et al. 2023b, The Southern-sky MWA Rapid Two-metre (SMART) pulsar survey – II. Survey status, pulsar census, and first pulsar discoveries, arXiv e-prints, arXiv:2302.11920
- Bhattacharyya, B., Gupta, Y., & Gil, J. 2009, Exploring the remarkable subpulse drift and polarization properties of PSR B0818–41, *Monthly Notices of the Royal Astronomical Society*, 398, 1435
- Bhattacharyya, B., Gupta, Y., & Gil, J. 2010, Investigation of the unique nulling properties of PSR B0818-41, *MNRAS*, 408, 407
- Biggs, J. D. 1992, An Analysis of Radio Pulsar Nulling Statistics, *ApJ*, 394, 574
- Bilous, A. V. 2018, PSR B0943+10: low-frequency study of subpulse periodicity in the Bright mode with LOFAR, *A&A*, 616, A119
- Brentjens, M. A., & de Bruyn, A. G. 2005, Faraday rotation measure synthesis, *A&A*, 441, 1217
- Burke-Spolaor, S., Johnston, S., Bailes, M., et al. 2012, The High Time Resolution Universe Pulsar Survey - V. Single-pulse energetics and modulation properties of 315 pulsars, *MNRAS*, 423, 1351
- Burn, B. J. 1966, On the depolarization of discrete radio sources by Faraday dispersion, *MNRAS*, 133, 67
- Cairns, I. H., Das, P., Robinson, P. A., & Johnston, S. 2003a, Intrinsic variability and field statistics for the Vela pulsar - III. Two-component fits and detailed assessment of stochastic growth theory, *MNRAS*, 343, 523
- Cairns, I. H., Johnston, S., & Das, P. 2003b, Intrinsic variability and field statistics for the Vela pulsar - II. Systematics and single-component fits, *MNRAS*, 343, 512

- Cairns, I. H., Johnston, S., & Das, P. 2004, Intrinsic variability and field statistics for pulsars B1641-45 and B0950+08, *MNRAS*, 353, 270
- Cairns, I. H., Johnston, S., Das, P., & Robinson, P. A. 2003c, in *Astronomical Society of the Pacific Conference Series*, Vol. 302, *Radio Pulsars*, ed. M. Bailes, D. J. Nice, & S. E. Thorsett, 191
- Caleb, M., Heywood, I., Rajwade, K., et al. 2022, Discovery of a radio-emitting neutron star with an ultra-long spin period of 76 s, *Nature Astronomy*, 6, 828
- Chadwick, J. 1932, The existence of a neutron, *Proceedings of the Royal Society of London. Series A, Containing Papers of a Mathematical and Physical Character*, 136, 692
- Champion, D. J., Lorimer, D. R., McLaughlin, M. A., et al. 2005, Arecibo timing and single-pulse observations of 17 pulsars, *MNRAS*, 363, 929
- Chandrasekhar, S. 1931, The Maximum Mass of Ideal White Dwarfs, *ApJ*, 74, 81
- Cheng, A. F. 1981, in *Pulsars: 13 Years of Research on Neutron Stars*, ed. W. Sieber & R. Wielebinski, Vol. 95, 99–101
- Cheng, A. F., & Ruderman, M. A. 1980, Particle acceleration and radio emission above pulsar polar caps., *ApJ*, 235, 576
- Clark, M. A., LaPlante, P. C., & Greenhill, L. J. 2013, Accelerating radio astronomy cross-correlation with graphics processing units, *International Journal of High Performance Computing Applications*, 27, 178
- Clemens, J. C., & Rosen, R. 2008, A Pulsational Model for the Orthogonal Polarization Modes in Radio Pulsars, *ApJ*, 680, 664
- Cocke, W. J., Disney, M. J., & Taylor, D. J. 1969, Discovery of Optical Signals from Pulsar NP 0532, *Nature*, 221, 525

- Cordes, J., Kramer, M., Lazio, T., et al. 2004, Pulsars as tools for fundamental physics & astrophysics, *New Astronomy Reviews*, 48, 1413, science with the Square Kilometre Array
- Cordes, J. M. 1978, Observational limits on the location of pulsar emission regions., *ApJ*, 222, 1006
- Cordes, J. M. 1979, Coherent Radio Emission from Pulsars, *Space Sci. Rev.*, 24, 567
- Cordes, J. M. 2013, Pulsar State Switching from Markov Transitions and Stochastic Resonance, *ApJ*, 775, 47
- Cordes, J. M., Bhat, N. D. R., Hankins, T. H., McLaughlin, M. A., & Kern, J. 2004, The Brightest Pulses in the Universe: Multifrequency Observations of the Crab Pulsar's Giant Pulses, *ApJ*, 612, 375
- Cordes, J. M., & Lazio, T. J. W. 2001, Anomalous Radio-Wave Scattering from Interstellar Plasma Structures, *ApJ*, 549, 997
- Cordes, J. M., & Lazio, T. J. W. 2002, NE2001.I. A New Model for the Galactic Distribution of Free Electrons and its Fluctuations, arXiv e-prints, astro
- Cordes, J. M., Weisberg, J. M., & Boriakoff, V. 1985, Small-scale electron density turbulence in the interstellar medium., *ApJ*, 288, 221
- Craft, H. D., Comella, J. M., & Drake, F. D. 1968, Submillisecond Radio Intensity Variations in Pulsars, *Nature*, 218, 1122
- Daugherty, J. K., & Harding, A. K. 1986, Compton Scattering in Strong Magnetic Fields, *ApJ*, 309, 362
- Deich, W. T. S., Cordes, J. M., Hankins, T. H., & Rankin, J. M. 1986, Null Transition Times, Quantized Drift Modes, and No Memory across Nulls for PSR 1944+17, *ApJ*, 300, 540

- Deshpande, A. A., & Rankin, J. M. 1999, Pulsar Magnetospheric Emission Mapping: Images and Implications of Polar CAP Weather, *ApJ*, 524, 1008
- Drake, F. D., & Craft, H. D. 1968, Second Periodic Pulsation in Pulsars, *Nature*, 220, 231
- Edwards, R. T., & Stappers, B. W. 2002, Drifting sub-pulse analysis using the two-dimensional Fourier transform, *A&A*, 393, 733
- Edwards, R. T., & Stappers, B. W. 2003, The frequency-dependence of drifting subpulse patterns, *A&A*, 410, 961
- Filippenko, A. V., & Radhakrishnan, V. 1982, Pulsar nulling and drifting subpulse memory., *ApJ*, 263, 828
- Gajjar, V., Joshi, B. C., & Kramer, M. 2012, A survey of nulling pulsars using the Giant Meterwave Radio Telescope, *Monthly Notices of the Royal Astronomical Society*, 424, 1197
- Gajjar, V., Joshi, B. C., & Wright, G. 2014, On the long nulls of PSRs J1738–2330 and J1752+2359, *Monthly Notices of the Royal Astronomical Society*, 439, 221
- Gajjar, V., Yuan, J. P., Yuen, R., et al. 2017, On Nulling, Drifting, and Their Interactions in PSRs J1741-0840 and J1840-0840, *ApJ*, 850, 173
- Gangadhara, R. T. 1997, Orthogonal polarization mode phenomenon in pulsars., *A&A*, 327, 155
- Gangadhara, R. T. 2004, Pulsar Radio Emission Altitude from Curvature Radiation, *Astrophysical Journal*, 609, 335
- Gil, J., Melikidze, G. I., & Geppert, U. 2003, Drifting subpulses and inner acceleration regions in radio pulsars, *A&A*, 407, 315

- Gil, J. A., & Sendyk, M. 2000, Spark Model for Pulsar Radiation Modulation Patterns, *ApJ*, 541, 351
- Gogoberidze, G., Machabeli, G. Z., Melrose, D. B., & Luo, Q. 2005, On the origin of the drifting subpulses in radio pulsars, *MNRAS*, 360, 669
- Gold, T. 1968, Rotating Neutron Stars as the Origin of the Pulsating Radio Sources, *Nature*, 218, 731
- Gold, T. 1969, Rotating Neutron Stars and the Nature of Pulsars, *Nature*, 221, 25
- Goldreich, P., & Julian, W. H. 1969, Pulsar Electrodynamics, *ApJ*, 157, 869
- Greisen, E. W. 1998, in *Astronomical Society of the Pacific Conference Series*, Vol. 145, *Astronomical Data Analysis Software and Systems VII*, ed. R. Albrecht, R. N. Hook, & H. A. Bushouse, 204
- Gupta, Y., Gothoskar, P., Joshi, B. C., et al. 2000, in *Astronomical Society of the Pacific Conference Series*, Vol. 202, *IAU Colloq. 177: Pulsar Astronomy - 2000 and Beyond*, ed. M. Kramer, N. Wex, & R. Wielebinski, 277
- Gupta, Y., Ajithkumar, B., Kale, H. S., et al. 2017, The upgraded GMRT: opening new windows on the radio Universe, *Current Science*, 113, 707
- Hankins, T. H., Kern, J. S., Weatherall, J. C., & Eilek, J. A. 2003, Nanosecond radio bursts from strong plasma turbulence in the Crab pulsar, *Nature*, 422, 141
- Hankins, T. H., & Rickett, B. J. 1986, Frequency Dependence of Pulsar Profiles, *ApJ*, 311, 684
- Harding, A. K., & Preece, R. 1987, Quantized Synchrotron Radiation in Strong Magnetic Fields, *ApJ*, 319, 939

- Heald, G., Braun, R., & Edmonds, R. 2009, The Westerbork SINGS survey. II Polarization, Faraday rotation, and magnetic fields, *A&A*, 503, 409
- Heiles, C., & Campbell, D. B. 1970, Pulsar NP 0532: Properties and Systematic Polarization of Individual Strong Pulses at 430 MHz, *Nature*, 226, 529
- Herfindal, J. L., & Rankin, J. M. 2007, Periodic nulls in the pulsar B1133+16, *MNRAS*, 380, 430
- Herfindal, J. L., & Rankin, J. M. 2009, Deep analyses of nulling in Arecibo pulsars reveal further periodic behaviour, *MNRAS*, 393, 1391
- Hessels, J. W. T., Ransom, S. M., Stairs, I. H., et al. 2006, A Radio Pulsar Spinning at 716 Hz, *Science*, 311, 1901
- Hewish, A., Bell, S. J., Pilkington, J. D. H., Scott, P. F., & Collins, R. A. 1968, Observation of a Rapidly Pulsating Radio Source, *Nature*, 217, 709
- Hotan, A. W., van Straten, W., & Manchester, R. N. 2004, PSRCHIVE and PSRFITS: An Open Approach to Radio Pulsar Data Storage and Analysis, *Publ. Astron. Soc. Australia*, 21, 302
- Huber, P. J. 1964, Robust Estimation of a Location Parameter, *The Annals of Mathematical Statistics*, 35, 73
- Huguenin, G. R., Taylor, J. H., & Troland, T. H. 1970, The Radio Emission from Pulsar MP 0031-07, *ApJ*, 162, 727
- Intema, H. T. 2014a, in *Astronomical Society of India Conference Series*, Vol. 13, *Astronomical Society of India Conference Series*, 469
- Intema, H. T. 2014b, SPAM: Source Peeling and Atmospheric Modeling, *Astrophysics Source Code Library*, record ascl:1408.006, ascl:1408.006

- Intema, H. T., van der Tol, S., Cotton, W. D., et al. 2009, Ionospheric calibration of low frequency radio interferometric observations using the peeling scheme. I. Method description and first results, *A&A*, 501, 1185
- Janagal, P., Chakraborty, M., Bhat, N. D. R., Bhattacharyya, B., & McSweeney, S. J. 2022, Revisiting the subpulse drifting phenomenon in PSR J1822-2256: drift modes, sparks, and emission heights, *MNRAS*, 509, 4573
- Janagal, P., Chakraborty, M., Bhat, N. D. R., McSweeney, S. J., & Sett, S. 2023, Single-pulse analysis and average emission characteristics of PSR J1820-0427 from observations made with the MWA and uGMRT, *MNRAS*, 523, 5934
- Janagal, P., McSweeney, S. J., Chakraborty, M., & Bhat, N. D. R. 2023, PSR J0026–1955: A curious case of evolutionary subpulse drifting and nulling, *Monthly Notices of the Royal Astronomical Society*, 524, 2684
- Jankowski, F., van Straten, W., Keane, E. F., et al. 2018, Spectral properties of 441 radio pulsars, *MNRAS*, 473, 4436
- Janssen, G. H., & van Leeuwen, J. 2004, Intermittent nulls in PSR B0818-13, and the subpulse-drift alias mode, *A&A*, 425, 255
- Johnston, S., & Kerr, M. 2017, Polarimetry of 600 pulsars from observations at 1.4 GHz with the Parkes radio telescope, *Monthly Notices of the Royal Astronomical Society*, 474, 4629
- Johnston, S., Kramer, M., Karastergiou, A., et al. 2007, Evidence for alignment of the rotation and velocity vectors in pulsars – II. Further data and emission heights, *Monthly Notices of the Royal Astronomical Society*, 381, 1625
- Johnston, S., van Straten, W., Kramer, M., & Bailes, M. 2001, High Time Resolution Observations of the Vela Pulsar, *ApJ*, 549, L101

- Jones, P. B. 2013, An incomplete model of RRATs and of nulls mode changes and subpulses, *MNRAS*, 431, 2756
- Joshi, B. C., Naidu, A., Gajjar, V., & Wright, G. A. E. 2018, in *Pulsar Astrophysics the Next Fifty Years*, ed. P. Weltevrede, B. B. P. Perera, L. L. Preston, & S. Sanidas, Vol. 337, 348–349
- Joshi, B. C., & Vivekanand, M. 2000, A study of subpulse phase correlation across nulls in PSR B0031-07, *MNRAS*, 316, 716
- Kaspi, V. M. 2010, Grand unification of neutron stars, *Proceedings of the National Academy of Sciences*, 107, 7147
- Kazbegi, A. Z., Machabeli, G. Z., & Melikidze, G. I. 1991, The Nature of Pulsar Subpulse Drift, *Australian Journal of Physics*, 44, 573
- Kettenis, M., van Langevelde, H. J., Reynolds, C., & Cotton, B. 2006, in *Astronomical data analysis software and systems XV*, Vol. 351, 497
- Kijak, J., Kramer, M., Wielebinski, R., & Jessner, A. 1998, Pulse shapes of radio pulsars at 4.85 GHz, *A&AS*, 127, 153
- Kirsten, F., Bhat, N. D. R., Meyers, B. W., et al. 2019, Probing Pulsar Scattering between 120 and 280 MHz with the MWA, *ApJ*, 874, 179
- Kiziltan, B. 2011, Reassessing The Fundamentals: New Constraints on the Evolution, Ages and Masses of Neutron Stars, *AIP Conf. Proc.*, 1379, 41
- Kramer, M., Karastergiou, A., Gupta, Y., et al. 2003, Simultaneous single-pulse observations of radio pulsars. IV. Flux density spectra of individual pulses, *A&A*, 407, 655
- Kramer, M., Lyne, A. G., O’Brien, J. T., Jordan, C. A., & Lorimer, D. R. 2006, A Periodically Active Pulsar Giving Insight into Magnetospheric Physics, *Science*, 312, 549

- Lang, K. R. 1969, Interstellar Scintillations of Pulsar Radiation, *Science*, 166, 1401
- Lang, K. R. 1971, Interstellar Scintillation of Pulsar Radiation, *ApJ*, 164, 249
- Lee, C. P., Bhat, N. D. R., Sokolowski, M., et al. 2022, Spectral analysis of 22 radio pulsars using SKA-Low precursor stations, *Publ. Astron. Soc. Australia*, 39, e042
- Lorimer, D. R. 2008, Binary and Millisecond Pulsars, *Living Reviews in Relativity*, 11, 8
- Lorimer, D. R. 2009, Radio Pulsar Statistics, ed. W. Becker (Berlin, Heidelberg: Springer Berlin Heidelberg), 1–17
- Lorimer, D. R., & Kramer, M. 2004, *Handbook of Pulsar Astronomy*, Vol. 4
- Lorimer, D. R., Yates, J. A., Lyne, A. G., & Gould, D. M. 1995, Multifrequency flux density measurements of 280 pulsars, *MNRAS*, 273, 411
- Luo, Q., & Melrose, D. B. 1995, Curvature maser emission due to field line torsion in pulsar magnetospheres, *MNRAS*, 276, 372
- Lyne, A. G., & Ashworth, M. 1983, The effect of nulls upon subpulse drift in PSRs 0809 + 74 and 0818 – 13, *Monthly Notices of the Royal Astronomical Society*, 204, 519
- Lyne, A. G., Smith, F. G., & Graham, D. A. 1971, Characteristics of the Radio Pulses from the Pulsars, *Monthly Notices of the Royal Astronomical Society*, 153, 337
- Lyubarskii, Y. E. 1996, Generation of pulsar radio emission., *A&A*, 308, 809
- Maan, Y. 2019, Expected Imprints of the Carousel in Multi-frequency Pulsar Observations and New Evidence for Multi-altitude Emission, *ApJ*, 870, 110
- Manchester, R. N., Hobbs, G. B., Teoh, A., & Hobbs, M. 2005, *VizieR Online Data Catalog: ATNF Pulsar Catalog (Manchester+, 2005)*, *VizieR Online Data Catalog*, VII/245

- Manchester, R. N., & Taylor, J. H. 1977, Pulsars
- Maron, O., Kijak, J., Kramer, M., & Wielebinski, R. 2000, Pulsar spectra of radio emission, *A&AS*, 147, 195
- McMullin, J. P., Waters, B., Schiebel, D., Young, W., & Golap, K. 2007, in *Astronomical Society of the Pacific Conference Series*, Vol. 376, *Astronomical Data Analysis Software and Systems XVI*, ed. R. A. Shaw, F. Hill, & D. J. Bell, 127
- McSweeney, S. 2019, PhD thesis, Curtin University, Australia
- McSweeney, S. J., Bhat, N. D. R., Tremblay, S. E., Deshpande, A. A., & Ord, S. M. 2017, Low-frequency Observations of the Subpulse Drifter PSR J0034-0721 with the Murchison Widefield Array, *ApJ*, 836, 224
- McSweeney, S. J., Bhat, N. D. R., Wright, G., Tremblay, S. E., & Kudale, S. 2019, The Frequency-dependent Behavior of Subpulse Drifting. I. Carousel Geometry and Emission Heights of PSR B0031-07, *ApJ*, 883, 28
- McSweeney, S. J., Bhat, N. D. R., Swainston, N. A., et al. 2022, Independent Discovery of a Nulling Pulsar with Unusual Subpulse Drifting Properties with the Murchison Widefield Array, *ApJ*, 933, 210
- Melrose, D. B. 2017, Coherent emission mechanisms in astrophysical plasmas, *Reviews of Modern Plasma Physics*, 1, 5
- Melrose, D. B., Rafat, M. Z., & Mastrano, A. 2020, Pulsar radio emission mechanisms: a critique, *Monthly Notices of the Royal Astronomical Society*, 500, 4530
- Melrose, D. B., Rafat, M. Z., & Mastrano, A. 2021, Pulsar radio emission mechanisms: a critique, *MNRAS*, 500, 4530
- Mitra, D., Basu, R., Maciesiak, K., et al. 2016, METERWAVELENGTH SINGLE-PULSE POLARIMETRIC EMISSION SURVEY, *The Astrophysical Journal*, 833, 28

- Murphy, T., Kaplan, D. L., Bell, M. E., et al. 2017, Low-Frequency Spectral Energy Distributions of Radio Pulsars Detected with the Murchison Widefield Array, *Publ. Astron. Soc. Australia*, 34, e020
- Naidu, A., Joshi, B. C., Manoharan, P. K., & Krishnakumar, M. A. 2017, Detection of long nulls in PSR B1706–16, a pulsar with large timing irregularities, *Monthly Notices of the Royal Astronomical Society*, 475, 2375
- Naidu, A., Joshi, B. C., Manoharan, P. K., & KrishnaKumar, M. A. 2017, Simultaneous multi-frequency single pulse observations of pulsars, *A&A*, 604, A45
- Narayan, R. 1992, The Physics of Pulsar Scintillation, *Philosophical Transactions of the Royal Society of London Series A*, 341, 151
- Noutsos, A., Johnston, S., Kramer, M., & Karastergiou, A. 2008, New pulsar rotation measures and the Galactic magnetic field, *MNRAS*, 386, 1881
- Noutsos, A., Sobey, C., Kondratiev, V. I., et al. 2015, Pulsar polarisation below 200 MHz: Average profiles and propagation effects, *A&A*, 576, A62
- Offringa, A. R., van de Gronde, J. J., & Roerdink, J. B. T. M. 2012, A morphological algorithm for improving radio-frequency interference detection, *A&A*, 539, A95
- Offringa, A. R., McKinley, B., Hurley-Walker, N., et al. 2014, WSCLEAN: an implementation of a fast, generic wide-field imager for radio astronomy, *MNRAS*, 444, 606
- Offringa, A. R., Wayth, R. B., Hurley-Walker, N., et al. 2015, The Low-Frequency Environment of the Murchison Widefield Array: Radio-Frequency Interference Analysis and Mitigation, *Publ. Astron. Soc. Australia*, 32, e008
- Ord, S. M., Tremblay, S. E., McSweeney, S. J., et al. 2019, MWA tied-array processing I: Calibration and beamformation, *Publ. Astron. Soc. Australia*, 36, e030

- Ord, S. M., Crosse, B., Emrich, D., et al. 2015, The Murchison Widefield Array Correlator, Publ. Astron. Soc. Australia, 32, e006
- Ostriker, J. P., & Gunn, J. E. 1969, On the Nature of Pulsars. I. Theory, ApJ, 157, 1395
- Qiao, G. J., Lee, K. J., Zhang, B., Xu, R. X., & Wang, H. G. 2004, A Model for the Challenging “Bi-drifting” Phenomenon in PSR J0815+09, ApJ, 616, L127
- Qiao, G. J., Lee, K. J., Zhang, B., Xu, R. X., & Wang, H. G. 2004, A Model for the Challenging “Bi-drifting” Phenomenon in PSR J0815+09, The Astrophysical Journal, 616, L127
- Radhakrishnan, V., & Cooke, D. J. 1969, Magnetic Poles and the Polarization Structure of Pulsar Radiation, Astrophys. Lett., 3, 225
- Rankin, J. M. 1983, Toward an empirical theory of pulsar emission. I. Morphological taxonomy., ApJ, 274, 333
- Rankin, J. M. 1986, Toward an Empirical Theory of Pulsar Emission. III. Mode Changing, Drifting Subpulses, and Pulse Nulling, ApJ, 301, 901
- Rankin, J. M., Comella, J. M., Craft, H. D., J., et al. 1970, Radio Pulse Shapes, Flux Densities, and Dispersion of Pulsar NP 0532, ApJ, 162, 707
- Rankin, J. M., & Wright, G. A. E. 2008, The ‘periodic nulls’ of radio pulsar J1819+1305, MNRAS, 385, 1923
- Rankin, J. M., Wright, G. A. E., & Brown, A. M. 2013, Drifting, moding and nulling: another look at pulsar B1918+19, MNRAS, 433, 445
- Ransom, S. M. 2001, PhD thesis, Harvard University, Massachusetts
- Reddy, S. H., Kudale, S., Gokhale, U., et al. 2017, A Wideband Digital Back-End for the Upgraded GMRT, Journal of Astronomical Instrumentation, 6, 1641011

- Redman, S. L., Wright, G. A. E., & Rankin, J. M. 2005, Pulsar PSR B2303+30: a single system of drifting subpulses, moding and nulling, *MNRAS*, 357, 859
- Rickett, B. J. 1990, Radio propagation through the turbulent interstellar plasma., *ARA&A*, 28, 561
- Robinson, P. 1992, Clumpy Langmuir waves in type III radio sources, *Solar Physics*, 139, 147
- Robinson, P. A. 1995, Stochastic wave growth, *Physics of Plasmas*, 2, 1466
- Robinson, P. A. 1997, Nonlinear wave collapse and strong turbulence, *Rev. Mod. Phys.*, 69, 507
- Robinson, P. A., Cairns, I. H., & Gurnett, D. A. 1993, Clumpy Langmuir Waves in Type III Radio Sources: Comparison of Stochastic-Growth Theory with Observations, *ApJ*, 407, 790
- Ruderman, M. 1972, Pulsars: Structure and Dynamics, *Annual Review of Astronomy and Astrophysics*, 10, 427
- Ruderman, M. A., & Sutherland, P. G. 1975, Theory of pulsars: polar gaps, sparks, and coherent microwave radiation., *ApJ*, 196, 51
- Salpeter, E. E. 1969, Pulsar Amplitude Variations, *Nature*, 221, 31
- Scheuer, P. A. G. 1968, Amplitude Variations in Pulsed Radio Sources, *Nature*, 218, 920
- Serylak, M., Stappers, B. W., & Weltevrede, P. 2009, S2DFS: analysis of temporal changes of drifting subpulses, *A&A*, 506, 865
- Sett, S., Bhat, N. D. R., Sokolowski, M., & Lenc, E. 2022, Image-based searches for pulsar candidates using MWA VCS data, *arXiv e-prints*, arXiv:2212.06982

- Sieber, W. 1973, Pulsar Spectra, *A&A*, 28, 237
- Singha, J., Surnis, M. P., Joshi, B. C., et al. 2021, Evidence for profile changes in PSR J1713+0747 using the uGMRT, *MNRAS*, 507, L57
- Smits, J. M., Mitra, D., & Kuijpers, J. 2005, Frequency dependence of the drifting subpulses of PSR B0031-07, *A&A*, 440, 683
- Sokolowski, M., Colegate, T., Sutinjo, A. T., et al. 2017, Calibration and Stokes Imaging with Full Embedded Element Primary Beam Model for the Murchison Widefield Array, *Publ. Astron. Soc. Australia*, 34, e062
- Sokolowski, M., Jordan, C. H., Slep, G., et al. 2020, Calibration database for the Murchison Widefield Array All-Sky Virtual Observatory, *Publ. Astron. Soc. Australia*, 37, e021
- Song, X., Weltevrede, P., Szary, A., et al. 2023, The Thousand-Pulsar-Array programme on MeerKAT - VIII. The subpulse modulation of 1198 pulsars, *MNRAS*, 520, 4562
- Staelin, D. H., & Reifenstein, E. C. 1968, Pulsating Radio Sources near the Crab Nebula, *Science*, 162, 1481
- Stovall, K., Lynch, R. S., Ransom, S. M., et al. 2014, The Green Bank Northern Celestial Cap Pulsar Survey. I. Survey Description, Data Analysis, and Initial Results, *ApJ*, 791, 67
- Sturrock, P. A. 1971, A Model of Pulsars, *ApJ*, 164, 529
- Sutton, J. M. 1971, Scattering of pulsar radiation in the interstellar medium, *MNRAS*, 155, 51
- Swainston, N. A., Bhat, N. D. R., Morrison, I. S., et al. 2022a, MWA tied-array processing IV: A multi-pixel beamformer for pulsar surveys and ionospheric corrected localisation, *Publ. Astron. Soc. Australia*, 39, e020

- Swainston, N. A., Lee, C. P., McSweeney, S. J., & Bhat, N. D. R. 2022b, pulsar_spectra: A pulsar flux density catalogue and spectrum fitting repository, arXiv e-prints, arXiv:2209.13324
- Swarup, G., Ananthakrishnan, S., Kapahi, V. K., et al. 1991, The Giant Metre-Wave Radio Telescope, *Current Science*, 60, 95
- Szary, A., van Leeuwen, J., Wright, G., et al. 2022, MeerKAT Observations of the Reversing Drifting Subpulses in PSR J1750-3503, *ApJ*, 934, 23
- Taylor, J. H., & Huguenin, G. R. 1971, Observations of Rapid Fluctuations of Intensity and Phase in Pulsar Emissions, *ApJ*, 167, 273
- Taylor, J. H., Huguenin, G. R., Hirsch, R. M., & Manchester, R. N. 1971, Polarization of the Drifting Subpulses of Pulsar 0809 + 74, *Astrophys. Lett.*, 9, 205
- Taylor, J. H., & Manchester, R. N. 1975, Observed properties of 147 pulsars., *AJ*, 80, 794
- Timokhin, A. N. 2010, A model for nulling and mode changing in pulsars, *MNRAS*, 408, L41
- Tingay, S. J., Goetze, R., Bowman, J. D., et al. 2013, The Murchison Widefield Array: The Square Kilometre Array Precursor at Low Radio Frequencies, *Publ. Astron. Soc. Australia*, 30, e007
- Tremblay, S. E., Ord, S. M., Bhat, N. D. R., et al. 2015, The High Time and Frequency Resolution Capabilities of the Murchison Widefield Array, *Publ. Astron. Soc. Australia*, 32, e005
- Unwin, S. C., Readhead, A. C. S., Wilkinson, P. N., & Ewing, W. S. 1978, Phase stability in the drifting subpulse pattern of PSR 0809+74., *MNRAS*, 182, 711

- van Leeuwen, A. G. J., Stappers, B. W., Ramachandran, R., & Rankin, J. M. 2003, Probing drifting and nulling mechanisms through their interaction in PSR B0809+74, *A&A*, 399, 223
- van Leeuwen, J., & Timokhin, A. N. 2012, On Plasma Rotation and Drifting Subpulses in Pulsars: Using Aligned Pulsar B0826-34 as a Voltmeter, *ApJ*, 752, 155
- van Straten, W., & Bailes, M. 2011, DSPSR: Digital Signal Processing Software for Pulsar Astronomy, *Publ. Astron. Soc. Australia*, 28, 1
- van Straten, W., Demorest, P., & Osłowski, S. 2012, Pulsar Data Analysis with PSRCHIVE, *Astronomical Research and Technology*, 9, 237
- Vivekanand, M., & Joshi, B. C. 1997, The Drifting Behavior of PSR B0031-07, *ApJ*, 477, 431
- Wang, N., Manchester, R. N., & Johnston, S. 2007, Pulsar nulling and mode changing, *MNRAS*, 377, 1383
- Wang, N., Manchester, R. N., & Johnston, S. 2007, Pulsar nulling and mode changing, *Monthly Notices of the Royal Astronomical Society*, 377, 1383
- Wang, P. F., Han, J. L., Han, L., et al. 2020, Jiamusi pulsar observations. III. Nulling of 20 pulsars, *A&A*, 644, A73
- Wayth, R., Tingay, S., Trott, C., et al. 2018, The Phase II Murchison Widefield Array: Design overview, *Publications of the Astronomical Society of Australia (PASA)*, 35, doi:10.1017/pasa.2018.37
- Weatherall, J. C. 1998, Pulsar Radio Emission by Conversion of Plasma Wave Turbulence: Nanosecond Time Structure, *ApJ*, 506, 341
- Weltevrede, P. 2018, in *Pulsar Astrophysics the Next Fifty Years*, ed. P. Weltevrede, B. B. P. Perera, L. L. Preston, & S. Sanidas, Vol. 337, 424–425

- Weltevrede, P., Edwards, R. T., & Stappers, B. W. 2006, The subpulse modulation properties of pulsars at 21 cm, *A&A*, 445, 243
- Weltevrede, P., Stappers, B. W., & Edwards, R. T. 2007, The subpulse modulation properties of pulsars at 92 cm and the frequency dependence of subpulse modulation, *A&A*, 469, 607
- Wen, Z. G., Yuan, J. P., Wang, N., et al. 2022, A Single-pulse Study of the Subpulse Drifter PSR J1631+1252 Discovered at FAST, *ApJ*, 929, 71
- Williamson, I. P. 1973, Pulse broadening due to multiple scattering in the interstellar medium-II, *MNRAS*, 163, 345
- Wright, G., & Weltevrede, P. 2017, Pulsar bi-drifting: implications for polar cap geometry, *MNRAS*, 464, 2597
- Xue, M., Ord, S. M., Tremblay, S. E., et al. 2019, MWA tied-array processing II: Polarimetric verification and analysis of two bright southern pulsars, *Publ. Astron. Soc. Australia*, 36, e025
- Yao, J. M., Manchester, R. N., & Wang, N. 2017, A New Electron-density Model for Estimation of Pulsar and FRB Distances, *ApJ*, 835, 29
- Zhang, B., Qiao, G. J., & Han, J. L. 1997, Inverse Compton Scattering: Gap Parameters, Energy Loss of the Particles, and Possible Implications for Pulsar Radio Emission, *ApJ*, 491, 891
- Zhao, F.-Y., Strom, R. G., & Jiang, S.-Y. 2006, The Guest Star of AD185 must have been a Supernova, *Chinese Journal of Astronomy and Astrophysics*, 6, 635
- Zhao, R.-S., Yan, Z., Wu, X.-J., et al. 2019, 5.0 GHz TMRT Observations of 71 Pulsars, *ApJ*, 874, 64